UNIFIED NONLINEAR OPTIMIZATION-BASED SENSORLESS CONTROL FOR SWITCHED RELUCTANCE MACHINE DRIVES

UNIFIED NONLINEAR OPTIMIZATION-BASED SENSORLESS CONTROL FOR SWITCHED RELUCTANCE MACHINE DRIVES

BY

SILVIO ROTILLI FILHO, B.Sc.

A THESIS

SUBMITTED TO THE DEPARTMENT OF ELECTRICAL & COMPUTER ENGINEERING

AND THE SCHOOL OF GRADUATE STUDIES

OF MCMASTER UNIVERSITY

IN PARTIAL FULFILMENT OF THE REQUIREMENTS

FOR THE DEGREE OF

DOCTOR OF PHILOSOPHY

Doctor of Philosophy (2022) McMaster University

(Electrical & Computer Engineering) Hamilton, Ontario, Canada

TITLE:	UNIFIED NONLINEAR OPTIMIZATION-BASED SENSORLESS CONTROL FOR SWITCHED RELUCTANCE MACHINE DRIVES
AUTHOR:	Silvio Rotilli Filho B.Sc., (Electrical Engineering) Federal University of Santa Catarina, UFSC, Florianópolis, Brazil
SUPERVISOR:	Dr. Ali Emadi Ph.D. (Texas A&M University) IEEE Fellow Professor and Canada Excellence Research Chair Laureate.
NUMBER OF PAGES:	xx, 139

To My Family

Abstract

Rotor position estimation of switched reluctance machines (SRMs) is the main focus of this work. Rotor position sensors are a crucial component of optimal motor controls. Fail-safe operation and system cost reduction have been extensively researched and implemented in industry and academia. Position sensorless control on switched reluctance machines introduces a new challenge due to high nonlinearity under different operating conditions.

A comprehensive review of SRM analytical modeling is presented, detailing each technique's main advantages and drawbacks. A least square-based analytical model (LSA) is proposed, which provides a simpler implementation and improved performance when compared to the methods commonly used in the literature. A literature review of rotor position sensor technology, position sensor fail modes, and position sensorless control is presented, providing a good roadmap of potential development and current limitations of the current technology. A wide speed range sensorless control is usually required when considering fail-safe techniques, fail detection methods and low-cost applications. A unified nonlinear optimization-based sensorless control is proposed in this thesis, where a single method is used for startup, low and high speeds, with reduced memory allocation where a look-up table is not required, optimal

transient response due to the elimination of a phase-locked-loop (PLL), and robustness against parameter variation. The method is validated at a wide speed range and torque conditions, thus showing the performance against conventional methods.

Acknowledgements

First, I would like to thank my supervisor and mentor, Dr. Ali Emadi, for all the guidance, inspiration, and allowing me to be part of his team, working alongside these amazing engineers and researchers in the best transportation electrification program in the world. Thank you for all the support and for being such a great inspiration.

I want to thank Dr. Berker Bilgin for his help through different projects and my Ph.D. studies. I was fortunate to attend Dr. Bilgin's course on switched reluctance machines, which helped me consolidate my knowledge in electric machines and controls.

My sincere gratitude to my supervisory committee members Dr.Mehdi Narimani and Dr. Babak Nahidmobarakeh. Your valuable contribution and insightful comments and discussions always showed me the path to improve my work.

I am grateful to my colleagues Carlos Vidal, Lucas Bruck, Fabricio Machado, Le Sun, Romina Rodriguez, Niloufar Keshmiri, John Ramoul, Jack Gillies, and Rasul Tarvirdilu-Asl for their support and friendship. Special thanks to David Ofori-Amoah, Diego Valencia, Sumedh Dhale, Peter Azer, Gaoliang Fang, and Dianxun Xiao, who were always available to help and contribute to my success, and to my colleagues and friends Iman Aghabali and Mehdi Eshaghian, who tragically left us, but will always be part of my life.

A very special thanks to my friend Alan Callegaro, who was always present during happy and tough times and inspired me to pursue my Ph.D. This would be a tough journey without your support.

I can't express in words my gratitude and love to my mother Losnei and my grandparents Lourdes and Leniro. Thank you for being such an inspiration for me, for all the unconditional love and support, and for teaching me all the values and principles that made me what I am today. Thanks to my aunt Loeri, uncles Leandro and Leocir, and father-in-law Rufino for all the support and help throughout my journey. A special thanks to my mother-in-law Rosa, who is no longer with us, but has always supported, loved, and encouraged me to pursue my dreams - I will always miss you.

My truthful gratitude to my wife Daniella and my daughters Olivia and Isabel. Thank you for all the love, unconditional support, and patience. Thank you for always being on my side during the hard times and for all the happiness and love you bring to my life. This would be impossible without you.

Notation and abbreviations

Abbreviation

SRM	Switched Reluctance Machine
SNR	Signal to Noise Ratio
EV	Electric Vehicle
HEV	Hybrid Electric Vehicle
IM	Induction Machine
PMSM	Permanent Magnet Synchronous Machine
FEA	Finite Element Analysis
PI	Proportional Integral
PWM	Pulse Width Modulation
LUT	Lookup Table
Back-EMF	Back Electromagnetic Force
LSA	Least Square-Based Analytical Approximation
ECU	Electronic Control Unit
VR	Variable Reluctance
PLL	Phase Locked Loop

DSP	Digital Signal Processor
AMR	Anisotropic Magnetoresistive-Effect
GMR	Giant Magnetoresistive-Effect
TMR	Tunneling Magnetoresistive-Effect
CMR	Colossal Magnetoresistive-Effect
SMO	Sliding Mode Observer
DAC	Digital Analog Converter
ADC	Analog Digital Converter
MAF	Moving Average Filter
UNLO	Unified Nonlinear Optimization

List of Symbols

θ	Rotor position
$\hat{\theta}$	Estimated Rotor position
V	Phase Voltage
i	Phase Current
λ	Flux-Linkage
L	Phase Inductance
R	Phase Resistance
e	Back-EMF
ω	Speed
W_f	Magnetic Stored Energy
W_c	Co-Energy

T	Torque
rpm	Revolutions per minute
V_{DC}	DC-Link VOltage

Contents

List of Tables

List of Figures

Chapter 1

Introduction

1.1 Motivation

The rapid growth in transportation electrification and the constant search for efficient use of electrical energy are pushing the industry to design reliable motors with high performance, high efficiency, high energy density, and low cost. In industry, 62.5% of all the energy consumption is related to motor drive application, and induction machines (IMs) have been the preferred choice given their low cost, and self-starting capability [1]. For transportation, electric machines are used in various applications, such as electric pumps, electronic power steering, electric seats, electric mirrors, and especially in the powertrain of electric vehicles (EVs) and hybrid vehicles (HEVs). For EVs and HEVs, permanent magnet synchronous motors (PMSMs) are often chosen due to their high power and torque density [2]; however, rare-earth permanent magnets are used in the rotor construction, which reduces the motor reliability when operating under harsh environment with extreme temperatures. Moreover, the price

instability and supply chain problems associated with rare-earth magnets can significantly increase the manufacturing costs of the machines [3].

Switched reluctance machines (SRMs) present a simple and reliable construction and lower manufacturing costs when compared to IMs and PMSMs [2]. SRMs do not contain conductors or permanent magnets in the rotor, having a simple construction of laminated steel with salient poles, which enables a reliable operation at high speeds and high temperatures, making a good candidate for traction and industrial application. However, the salient structure of the machine brings challenges associated with high torque ripple and acoustic noise. To overcome these challenges, advanced motor control algorithms have been extensively researched and implemented in the literature [4–10].

To properly control the SRM and to implement advanced motor control techniques, precise rotor position feedback is required. Position sensors can reduce the system's robustness and reliability, increase the motor size, and increase costs. The advantages of robust operation can be drastically reduced when using position sensors. Thus, replacing the position sensor with sensorless algorithms can eliminate sensor-related issues.

Several approaches have been proposed in the literature to estimate the rotor position information. They can be divided into two categories: magnetic-parameter-free and magnetic-parameter-based methods, subdivided into two sub-categories - low and high-speed sensorless controls.

When considering a low-speed operation, magnetic-parameter-free methods do not require any predefined information of the machine under test, relying on the estimated magnetic characteristics. However, it relies on the unsaturated magnetic

assumption, which can present high errors or unstable operation at high load conditions. Magnetic-parameter-based estimators present a higher position accuracy under wide load conditions, which is required for high dynamic systems with precise torque control. Parameter-based control presents the disadvantage of extra effort on machine characterization and high pre-stored magnetic characteristics of the motor.

Similar to the low-speed cases, the magnetic-parameter-free methods are independent of offline measurements and pre-stored data, but present challenges on sensitivity to current noises and ripples, discontinuous position estimation, or high implementation complexity. Magnetic-parameter-based sensorless control can reduce the system complexity by searching pre-stored magnetizing lookup tables, but these methods can present high sensitivity to noises, parameter variations, and high storage requirements. To mitigate the problems above, position sensorless control based on observers can improve system robustness, present low noise sensitivity, and reduce stored data sizes at the cost of increased system complexity and computational burden.

The position-sensorless control methods are feasible for a specific operating region, either low or high speeds, but not both. For a wide-speed range operation, different methods need to be combined. The main challenge is the transition region from one method to another and the increase in complexity, memory allocation, and computational time during the transition region. Stability problems and low reliability can also occur during this period.

This thesis proposes a magnetic-parameter-based unified sensorless control algorithm for a wide-speed operation, with reduced memory allocation, high transient response, and simple implementation while providing a low rotor position error.

1.2 Contributions

The author has contributed to several original developments in rotor position estimation and modeling of switched reluctance motor drives in this thesis, which are listed as follows:

1. A nonlinear analytical model of the phase inductance based on a least-square analytical approximation is proposed to improve model accuracy and potential reduction in system complexity compared to the methods shown in the literature.

2. A comprehensive analysis of rotor position sensor technologies, position sensor fail modes, and fail detection techniques is presented.

3. A cost function based on the machine voltage equations and nonlinear inductance profile is proposed to analyze and implement the position estimation method.

4. A unified nonlinear optimization-based position estimation method for starting operation and running state is proposed and validated.

5. A comparative benchmark assessment between the proposed and conventional sensorless control techniques is performed to comprehensively evaluate the proposed estimation methods.

1.3 Thesis Outline

The main objective of this work is to investigate the rotor position sensorless control of SRM drives, thus improving the overall performance and reliability of the system.

Chapter 2 introduces the general background and fundamental concepts of switched reluctance machines starting from its electromagnetic principles, operation and control, including a brief review of the power electronic converters used to drive the

SRMs.

Chapter 3 presents the literature review of SRMs magnetic characteristics modeling. It includes the experimental characterization of switched reluctance machines, the experimental setup used in this thesis, a comprehensive analysis of the different modeling techniques proposed in the literature, and a proposed least square-based analytical approximation, reducing the implementation complexity and improving model accuracy. A quantitative comparison between the different methods for the machine under test is also discussed.

In Chapter 4, a comprehensive review of the position sensor technology is presented. The position sensor failure modes and failure detection methods are discussed, showing the challenges in the early identification of near-to-failure states on fail-safe applications. This chapter also presents the existing sensorless control methods proposed in the literature, including startup techniques, low-speed parameter-based and parameter-free pulse injection methods, and high-speed techniques based on the prestored magnetic information of the machine or magnetic parameter-free approaches.

Chapter 5 presents the proposed unified nonlinear optimization-based method for a wide-speed operation, where the general approach of the estimator is presented, including the cost function based on the nonlinear inductance profile. The observable region on the positive and negative torque region is identified, showing a reasonable convergence rate to the local minimum of the proposed cost function. In order to force the minimization direction to a local minimum, the Levenberg-Marquart method, which is a combination of Newton's method for optimization and the steepest descent is proposed. The methods for standstill/start, low-speed and high-speed operation are presented, and the effectiveness of the position estimation method is demonstrated

by experimental results during steady-state and speed transient response.

In Chapter 6, a benchmark between the proposed method and a conventional method initially presented in Chapter 4 is presented. Different techniques for low and high speed are shown, and a transition from different speed ranges is implemented. The comparisons include both the dynamic and steady-state performance during speed transients at a wide speed range. Besides the comparison, some other attractive features of the proposed method are also presented.

Chapter 7 provides the conclusion of the thesis and suggestions for future work. It also presents a summary of publications and contributions.

Chapter 2

Switched Reluctance Machine (SRM) Drives and Control.

2.1 Fundamentals and Operating Principles of SRMs

2.1.1 Electromagnetic Principles

Switched reluctance machines construction presents a salient structure, where the rotor and stator have salient poles. Due to this characteristic, the air-gap changes depending on the rotor position, producing a highly nonlinear inductance, generating a flux-linkage that is a function of rotor angle (θ) and phase current (i). The flux-linkage ($\lambda(\theta, i)$) is generated only during the phase coils excitation. The equivalent circuit of a single-phase can be simplified neglecting the mutual coupling effect as presented in Figure 2.1, where V is the phase voltage, R is the phase resistance, $L(\theta, i)$ is the nonlinear phase inductance, and $e(\theta, i)$ is the back electromagnetic force (back-EMF). The mathematical model of the SRM can then be derived by the voltage

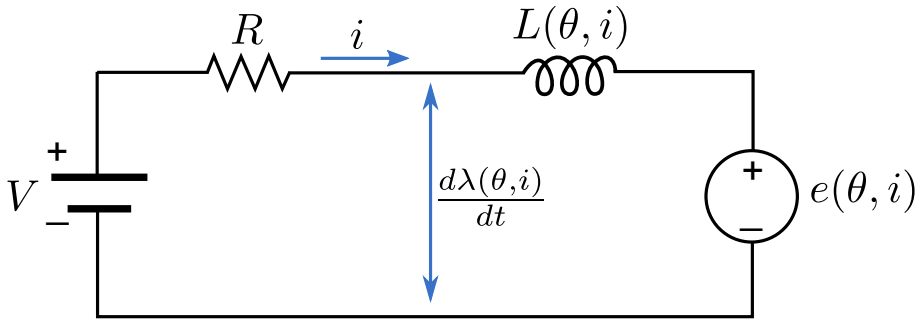

Figure 2.1: SRM equivalent circuit

equation as 2.1

$$\begin{aligned} V &= Ri + \frac{d\lambda(\theta,i)}{dt} \\ V &= Ri + \frac{\partial\lambda(\theta,i)}{\partial i}\frac{di}{dt} + \frac{\partial\lambda(\theta,i)}{\partial\theta}\frac{d\theta}{dt} \\ V &= Ri + \frac{\partial\lambda(\theta,i)}{\partial i}\frac{di}{dt} + \frac{\partial\lambda(\theta,i)}{\partial\theta}\omega \end{aligned} \tag{2.1}$$

where ω is the rotor speed. The flux can be expressed by the self-inductance $L(\theta, i)$ as 2.2.

$$\lambda(\theta, i) = iL\,(\theta, i) \tag{2.2}$$

And substituting 2.2 into 2.1, the model can be represented as 2.3

$$\begin{aligned} V &= Ri + L_{inc}(\theta,i)\frac{di}{dt} + e \\ e &= i\omega\frac{\partial L(\theta,i)}{\partial\theta} \\ L_{inc}(\theta,i) &= \underbrace{L(\theta,i)}_{\text{self-inductance}} + \underbrace{i\frac{\partial L(\theta,i)}{\partial i}}_{\text{magnetic saturation}} \end{aligned} \tag{2.3}$$

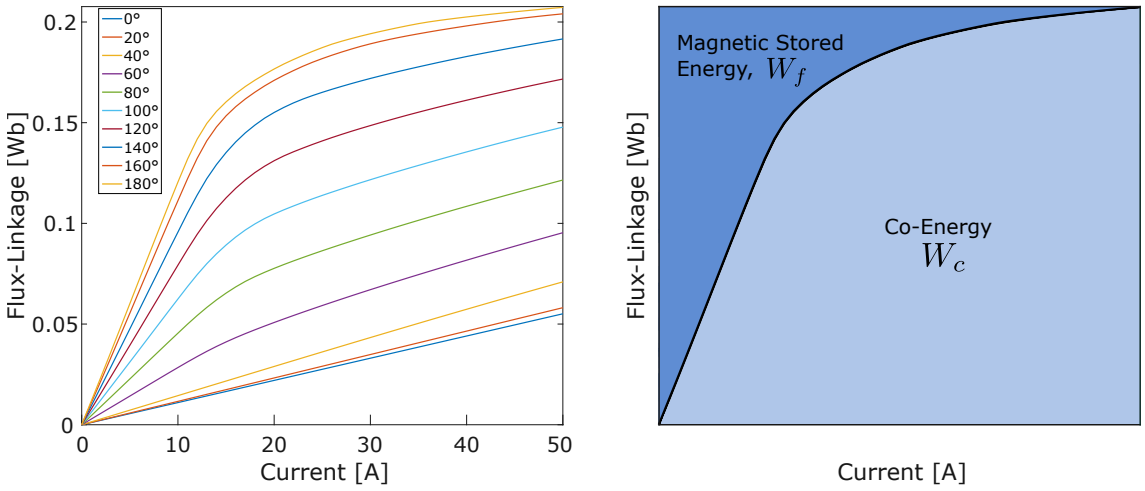

Figure 2.2: 8/6 SRM flux-linkage curves. a) magnetization curve for different rotor positions, b) co-energy representation at aligned position.

where $L_{inc}(\theta, i)$ is the incremental inductance, and e is the back-EMF, which represents the air gap power that will be converted into mechanical power, and is directly related to the excitation current and rotor speed. However, high currents can saturate the magnetic material, limiting the rate of change of flux-linkage. Figure 2.2a shows the flux-linkage profile of a 8/6 SRM under different rotor positions.

Considering a constant current and an infinitesimal change in flux-linkage, the magnetic stored energy (W_f) can be defined as 2.4.

$$W_f = \int i d\lambda(\theta, i) \tag{2.4}$$

The energy can also be calculated considering a constant flux-linkage and an infinitesimal change in current, which is called co-energy (W_c), and is defined in 2.5, been represented as the lower part of the graph in Figure 2.2b. Co-energy is not a physical quantity but is heavily used in energy storing systems due to the more

straightforward mathematical representation.

$$W_c = \int \lambda(\theta, i) di \tag{2.5}$$

When considering the linear region, the magnetic co-energy can be simplified as 2.6.

$$W_c = \frac{1}{2} L(\theta) i^2 \tag{2.6}$$

The amount of stored energy is dependent on the air gap volume, as shown in Figure 2.2a. The energy stored as co-energy is converted to mechanical power, and under electromagnetic saturation, the magnetic stored energy decreases while the co-energy increases, thus, increasing the torque capability of the machine. Under constant current excitation, the torque production is a function of the rate of change of co-energy.

$$T = \frac{dW_c}{d\theta} \tag{2.7}$$

Substituting 2.6 into 2.7, the torque can be derived as 2.8. By definition, the torque production is independent of the direction of current.

$$T = \frac{1}{2} \frac{dL(\theta)}{d\theta} i^2 \tag{2.8}$$

The SRM power can then be derived from 2.3 as 2.9.

$$\underbrace{iV}_{\text{electrical power}} = \underbrace{i^2 R}_{\text{copper losses}} + \underbrace{\frac{d}{dt}\left(\frac{1}{2} L(\theta)\, i^2\right)}_{\text{magnetic power}} + \underbrace{\frac{1}{2} i^2 \frac{dL(\theta)}{d\theta} \omega}_{\text{airgap power}} \tag{2.9}$$

The input electrical power is converted into electrical, magnetic, and mechanical power, respectively. The electrical power is dissipated as heat by the copper losses, the magnetic power is stored as a magnetic field in the magnetic circuit, and the air gap power is converted into torque production.

2.1.2 Operational Principles

Due to the double salient construction and material properties of the SRM, the torque production and flux linkage profile are functions of rotor position and phase current. Finite Element Analysis (FEA) provides a good understanding of the machine operation and helps evaluate the machine characteristics and dynamics. Since the flux generation happens only when the phase is energized, the majority of the generated flux links to the same phase coil; therefore, the mutual flux is negligible in conventional SRMs [1], and the single-phase characterization can be extrapolated to other phases.

The static flux-linkage profile and torque of an 8/6 SRM under a range of excitation currents is presented in Figure 2.3 and Figure 2.4, respectively. At unaligned position (0° electrical angle), the air gap is the largest, and the flux linkage and torque are minimum. The torque profile can be separated by the motoring region and generation region. When the flux-linkage increases, the torque is positive, and the electrical power is converted into mechanical power and losses. The opposite happens when the flux-linkage decreases, where the torque is negative and mechanical energy is converted into electric energy.

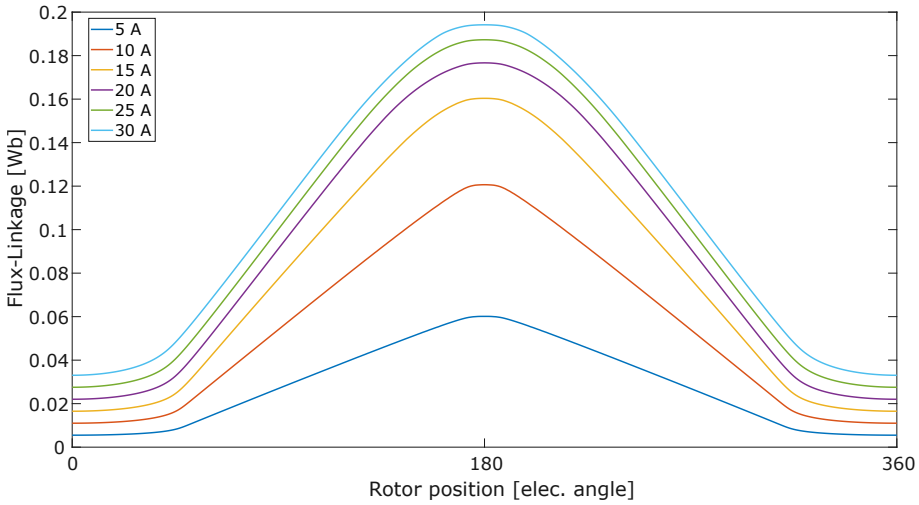

Figure 2.3: 8/6 SRM flux-linkage profile

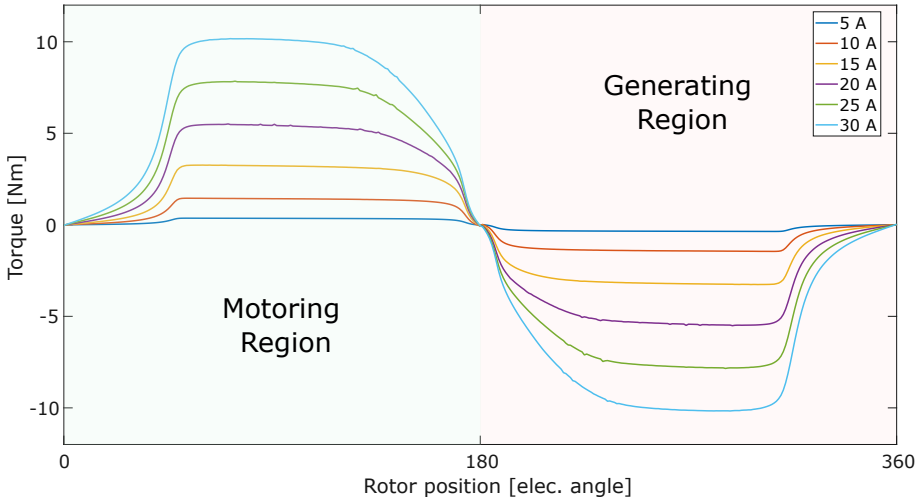

Figure 2.4: 8/6 SRM torque profile

For SRMs, during power generation, an excitation current needs to be applied, and the torque sign is independent of the current direction, relying only on the rotor position region. This can be better understood when considering the poles' tendency to align to the lowest reluctance path. When the rotor is at 0°, and the phase is

energized with a constant current, the mechanical torque is positive, and the rotor will self-align at 180° electrical degrees; thus, the machine will be operating in motoring mode. An external force needs to be applied to move away from the aligned position, so a negative torque is generated to pull back the rotor to alignment; thus, the machine will operate in generating mode.

2.1.3 Control of Switched Reluctance Machines

The stator winding needs to be sequentially excited when considering the continuous motion of the machine. In order to produce positive torque, the phase excitation happens on the positive slope of the flux-linkage, from unaligned to aligned rotor position.

A simplified commutation of a four-phase 8/6 SRM is presented in Figure 2.5. For phase A, the excitation starts at time t_1, and is represented as the turn-on angle θ_{ON}. At the time t_2, the phase is turned off at the turn-off angle θ_{OFF}, where the demagnetization starts and the residual currents are dissipated. During the demagnetization, the incoming phase starts to conduct, and during this short period, multiple phases are excited, thus varying the torque production during commutation, producing torque ripple.

The turn-on and turn-off angles need to be optimized for different speeds and torque requirements. Since the induced EMF on SRMs is dependent on the rotor speed and excitation current, as presented by 2.3, the induced voltage becomes relevant to the dynamics of the phase current at high-speed operation, where the rate o change of current ($\partial i/\partial t$) is dependent on the DC link voltage (V), the back EMF

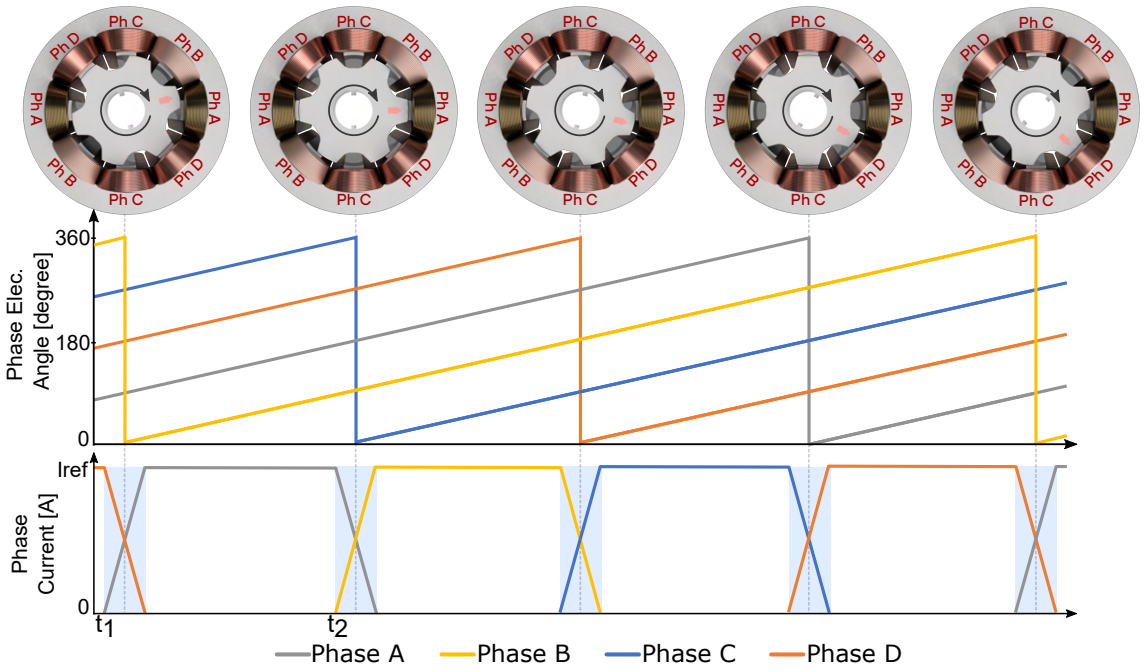

Figure 2.5: Simplified phase commutation scheme for a four-phase 8/6 SRM

(ε) and the inductance ($L(\theta, i)$), as presented by 2.10.

$$\frac{V - \varepsilon}{L(\theta, i)} = \frac{\partial i}{\partial t} \tag{2.10}$$

An overview of the closed-loop control scheme for SRMs is presented in Figure 2.6. Outer speed control can be implemented, giving the torque reference to the current control loop. The current loop is implemented to set the optimal conduction angles through a look-up table or other optimal control technique, sending the switching signal to the switches gates, thus, controlling the current based on the reference signal(i_{ref}).

A hysteresis current control can be used for current reference tracking by switching the DC-link voltage fed into the phase. To maintain the phase current within a limited

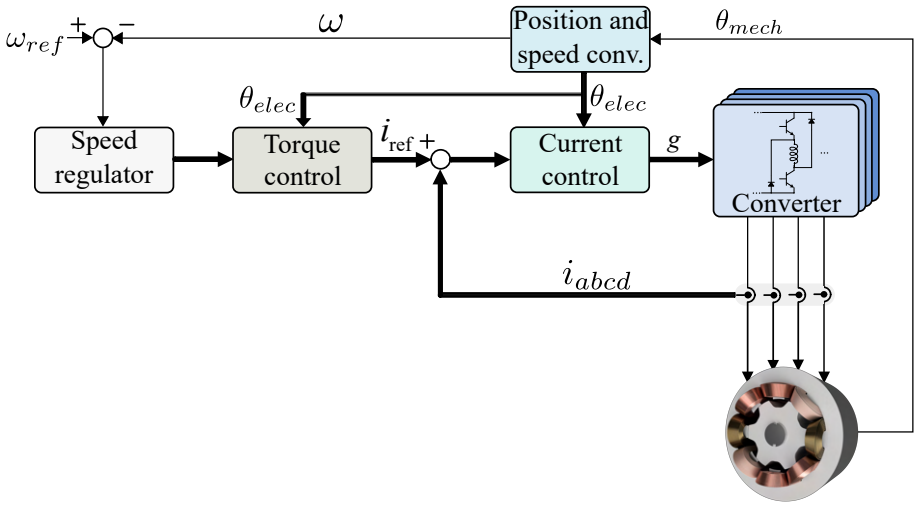

Figure 2.6: Control diagram of SRM drives

deviation from the current reference, a hysteresis band is defined by 2.11

$$\begin{aligned} i_{upper} &= i_{ref} \times (1 + \beta) \\ i_{lower} &= i_{ref} \times (1 - \beta) \end{aligned} \tag{2.11}$$

were i_{upper} and i_{lower} is the upper and lower band, respectively, and β is the band tolerance expressed as a percentage of the current reference. Figure 2.7 shows the switching profile for low and high speeds. It can be observed that the hysteresis current control has a variable switching frequency, where higher switching frequencies will be noticed near to the unaligned position (low inductance), and lower switching frequency will be noticed close to the aligned position (higher inductance). The switching is also highly dependent on the rotating speed, where at lower speeds, the back-EMF is low, and the rate of change of current is high. At high speeds, the

machine operates under a single pulse mode, where the phase is turned on at θ_{ON} and off at θ_{OFF} position.

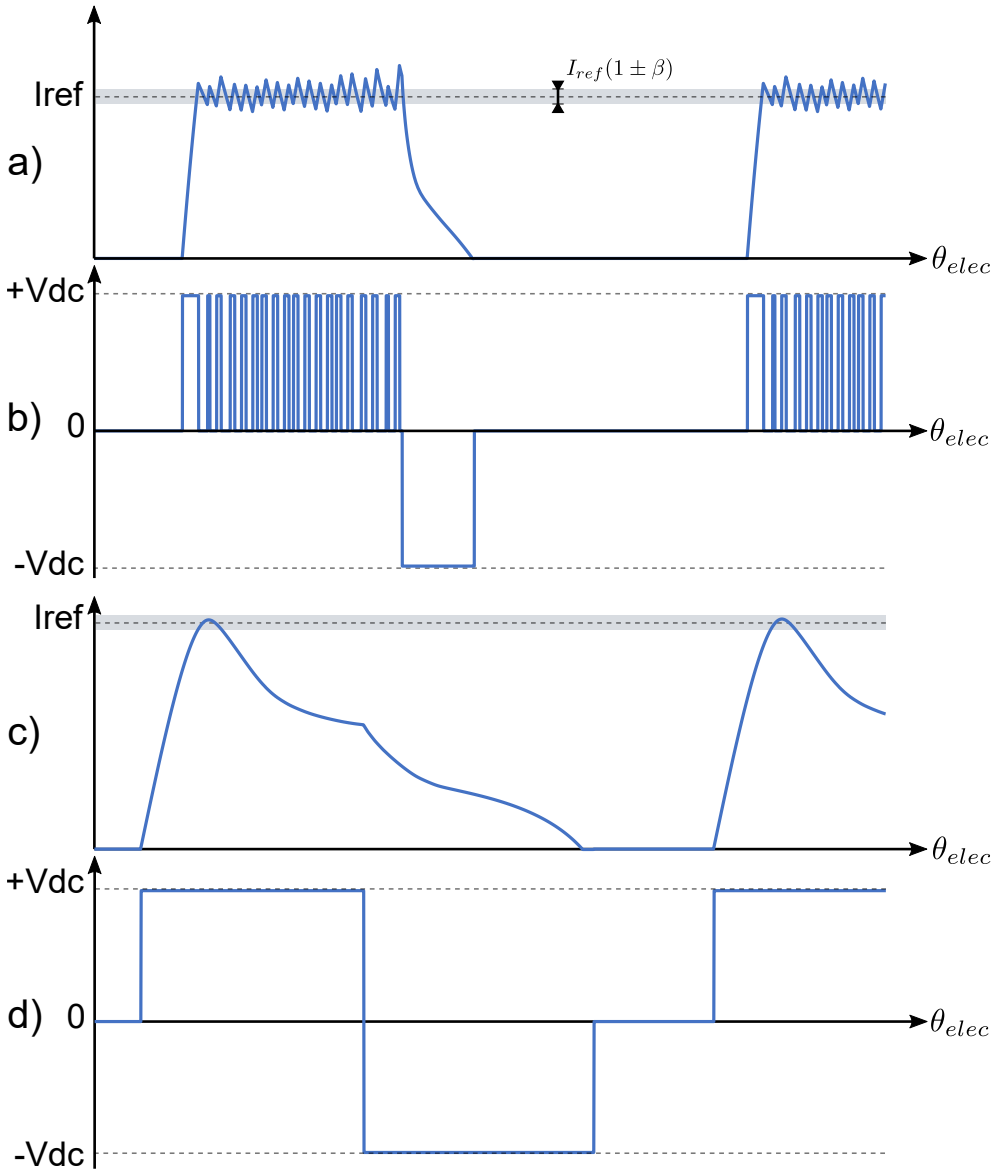

Figure 2.7: SRM soft-switching phase excitation and operational waveform: a) current waveform at low-speed, b) switching pattern for low-speed operation, c) current waveform at high-speed, d) switching pattern for high-speed

Several power converter topologies can be used for switched reluctance machines, like the (N+1)-switch converter, C-Dump, N-Switch, and others [11–13]. The most common implementation is the asymmetric bridge converter, shown in Figure 2.8, which allows independent current control for the phases at the cost of additional switches and diodes. There are two possible switching patterns: the hard-switching and soft-switching modes. In hard-switching, when the switches S_1 and S_2 are conducting (Figure 2.9a), the phase voltage is equal to the DC-link voltage (V_{DC}). The phase current then increases until it hits the upper limit of the hysteresis control. At this stage, the switches are turned OFF, and the current previously stored on the magnetic circuit is conducted back to the DC-link and DC-link capacitors through the diodes (Figure 2.9b). During this condition, the terminal phase voltage is equal to negative V_{DC}, causing the current to decrease to the lower limit of the hysteresis band rapidly. This process continues until the end of the excitation cycle, where the switches are turned OFF, and the phase current decays to zero. Hard-switching mode can result in faster response, at the cost of increased switching losses due to higher switching frequency and higher current harmonics and current ripple in the DC-link capacitors.

Soft-switching can improve the drawbacks of hard-switching at the cost of a slower current tracking response. For the soft-switching operation, both switches are ON during the phase excitation (Figure 2.9a). The DC-link voltage is applied to the phase terminals, and the current increases until it reaches the upper limit. At this point, the upper (S_1) or the bottom (S_2) switch is turned off, and the phase current freewheels through one diode and one switch. The phase voltage is equal to the sum of the voltage drop of the diode and switch, and the current slowly decay until it

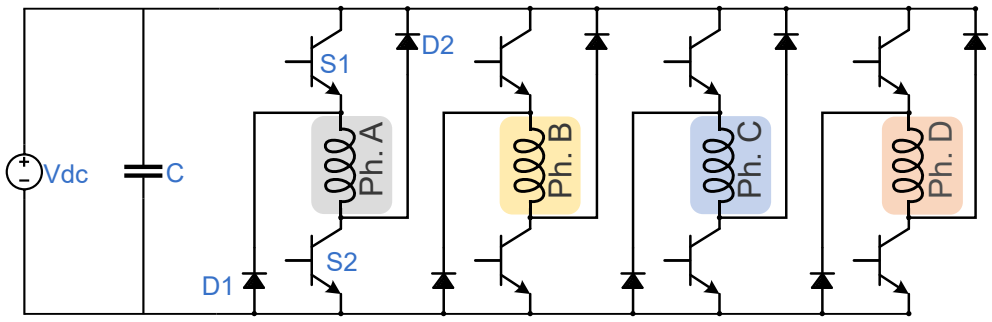

Figure 2.8: Four-phase asymmetric bridge converter

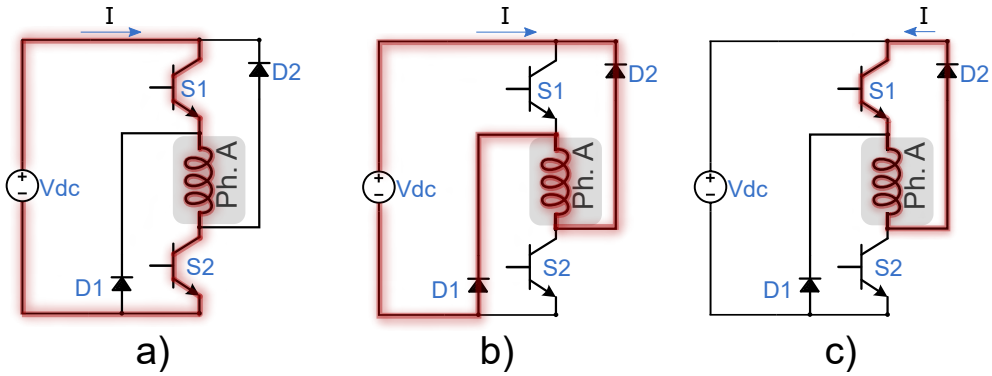

Figure 2.9: Asymmetric bridge converter operation: a) energized phase, b) hard-switching, c)soft-switching

reaches the hysteresis lower limit, where the switches start conducting. The switching pattern continues until the end of excitation, where all the switches are turned OFF to provide a fast reduction on phase current.

2.2 Summary

This chapter defines the operating principles of switched reluctance machine drives. The model is presented in terms of the machine voltage equations. The analysis of the stored energy explains the flux-linkage static characteristics and torque production in the air gap. A brief description of the most popular power converter is also presented,

and the hysteresis and single pulse control are introduced, presenting the current waveform during low and high-speed operation.

Chapter 3

Modeling of Switched Reluctance Machines

Switched reluctance machines are commonly designed to operate under magnetically saturated regions, increasing the co-energy, maximizing the torque production capability, and reducing the workload on power semiconductors. The magnetic nonlinearity of the machine needs to be considered for proper system modeling and controls. Accurate machine model presents several challenges, mainly because of the high nonlinear characteristics of the SRM flux-linkage and phase inductance, as presented in [14–19], where the nonlinear variation of the machine characteristics with respect to current and rotor position changes, are caused by the magnetic saturation and double saliency construction of the machine.

The inductance and flux-linkage profiles are highly dependent on the instantaneous phase current and rotor position; however, the machine characteristics can be obtained through finite element analysis (FEA) or experimental validation. Lookup-table-based models are simple to be implemented, and depending on the table size, can

present good accuracy, but this method suffers from high memory allocation, which is prohibitive or not desired in some applications. Analytical-based models are an alternative option for the magnetic parameter representation of the machine, providing this way a wide range of model fidelity, computational resources, and data allocation. The SRM characteristics can be analytically represented by the flux-linkage or phase inductance profiles and are categorized by linearized and non-linearized models.

Linearized models have a simple implementation, low data allocation, and low computational resources but reduced model fidelity. They can be represented in different categories: Single slope approximation, dual step approximation, and triple slope technique, which presents lower to a higher order of complexity, respectively. High-order polynomial approximations can be implemented to overcome the problems of analytical model fidelity and high modeling variations. A least square-based analytical approximation is proposed, where a benchmark performance with a conventional truncated Fourier expansion approximation and linear models is presented.

3.1 Numerical Analysis

The highly non-linear behavior of switched reluctance motors makes it extremely challenging to derive an analytical expression based solely on the machine geometry, since the flux-linkage is directly proportional to rotor position and current changes. FEA can be used for static electromagnetic simulations to properly model the machine. An accurate model of the flux-linkage and torque at different current excitation levels and rotor positions can be obtained. Figure 3.1 shows the static flux-linkage profile of a four-phase 8/6 SRM for different excitation current, and Figure 3.2 presents the inductance profile of the machine. Figure 3.3 shows the torque characteristics of the

machine under test.

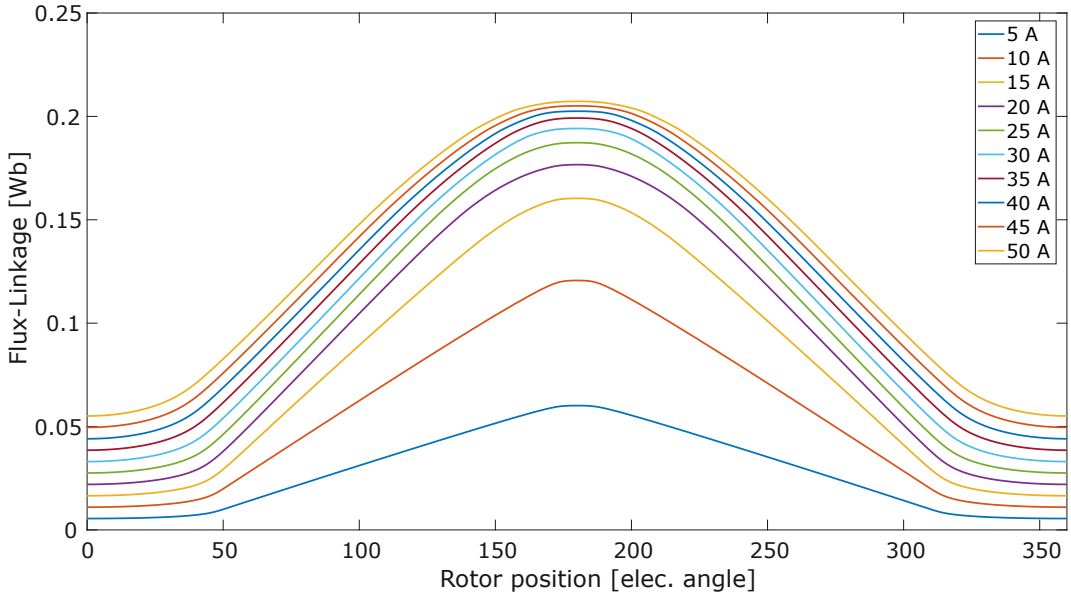

Figure 3.1: 8/6 SRM Flux-linkage profile

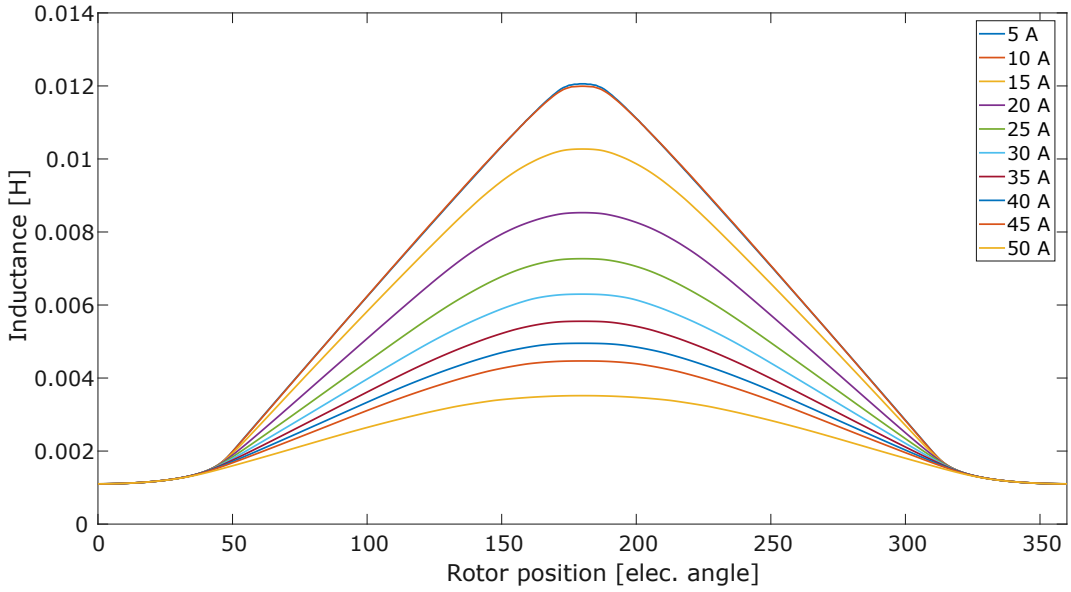

Figure 3.2: 8/6 SRM Inductance profile

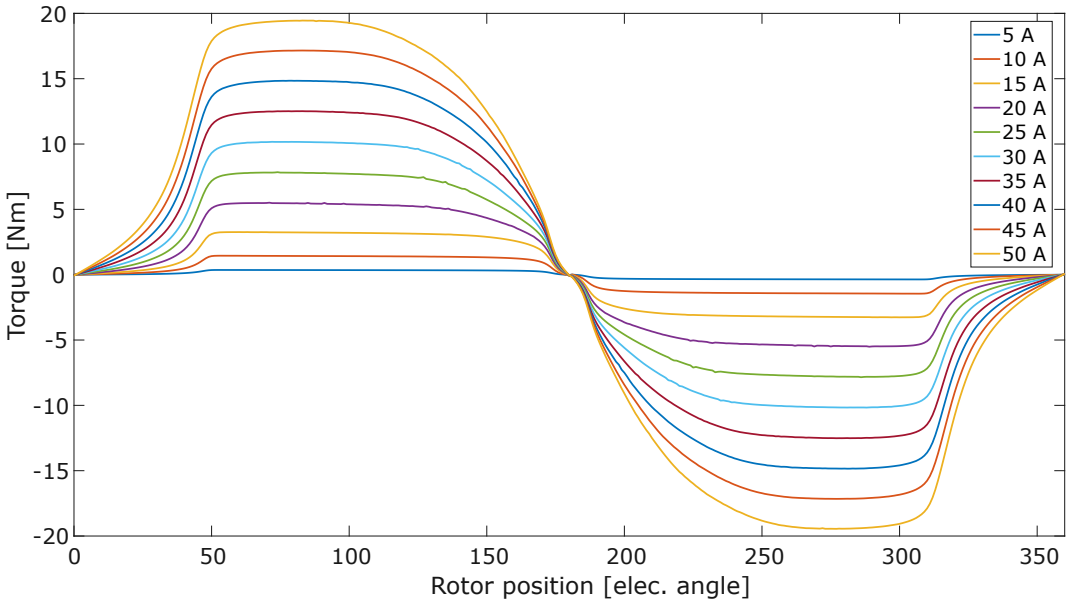

Figure 3.3: 8/6 SRM Torque profile

3.2 Experimental Characterization

3.2.1 Experimental Setup

The 2D electromagnetic FEA data presents several assumptions that are not always true compared to the designed machine characteristics, which can include deviations from the material properties that can occur during the manufacturing process, mechanical eccentricities and tolerances during assembly and manufacturing, and 3D leakage effects that are neglected from the finite element model.

The experimental test bench used in this work is based on a 5.1 kW, 300 V, 8/6 four-phase switched reluctance machine, with a rated speed of 6000 rpm, 8 Nm peak torque and 14.35 A of rated RMS phase current. A four-phase IGBT-based asymmetric converter is used for the tests, controlled by a TI TMS320F28335 digital

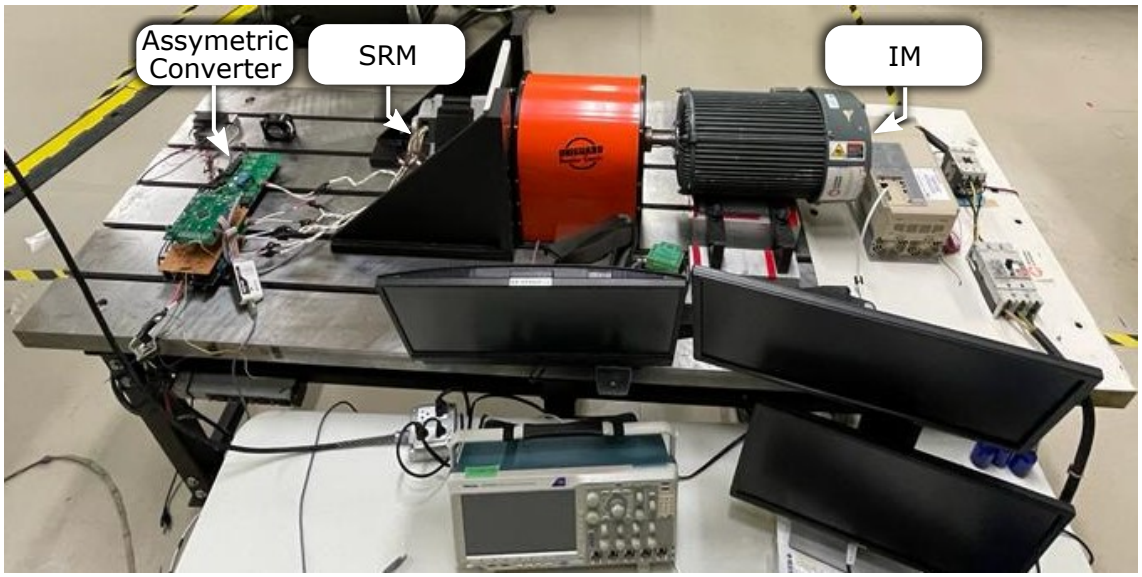

Figure 3.4: Experimental Setup

signal processor (DSP). A three-phase 11.2kW induction machine with a rated speed of 3600 rpm is used as a dyno, which operates in a speed controller loop. The complete setup is shown in Figure 3.4.

3.2.2 Non-linear Flux-linkage characterization

For the machine characterization, the dynamometer is decoupled from the system. The rotor position sensor and current sensors need to be calibrated for all the validation steps, reducing the measured errors and drifts from the real values, and the phase resistance needs to be measured at room temperature. The temperature variation can be neglected since the test is performed using short voltage pulses. As previously described, the flux-linkage profile of the SRM is a non-linear function of current and rotor position; therefore, to simplify the machine characterization, the rotor can be locked in pre-defined positions while the current varies from zero to the

rated current values, and the discrete flux-linkage profile can be derived by (3.1)

$$\lambda_k(\theta, i) = \sum_{0}^{k} (V_k - Ri_k)\,\Delta t \Bigg|_{\theta=const}, \tag{3.1}$$

where λ, V, R and i are the flux-linkage, phase voltage, phase resistance, and phase current, respectively, at time step k. The sampling time is represented by Δt.

The shaft can be locked at constant rotor positions using an indexer for the characterization procedure. A voltage pulse can be applied at discrete rotor position angles, building up the current to its rated value. The current data and rotor position during the transient response should be properly logged using a short sampling period since the system time constant will vary with rotor position. The rotor position information needs to be verified during the tests to evaluate the stiffness of the coupling between the rotor shaft and indexer since small displacements can occur, especially under high torque conditions.

The characterization data can then be used for an off-line calculation of the machine flux-linkage by (3.1), and the discrete data can be extrapolated. The resolution of the experimental data is dictated by the rotor position steps and acquisition sampling frequency. Figure 3.5 shows the comparison between the FEA and experimental validation. The experimental results show deviations from FEA, which can be caused by the 2D modeling assumptions, the stiffness of the motor/indexer coupling, and current/rotor positions measurement errors.

3.2.3 Non-linear Inductance Profile

From the experimental flux-linkage profile, the non-linear inductance characteristics can be derived by (3.2). The inductance amplitude has intrinsic information about

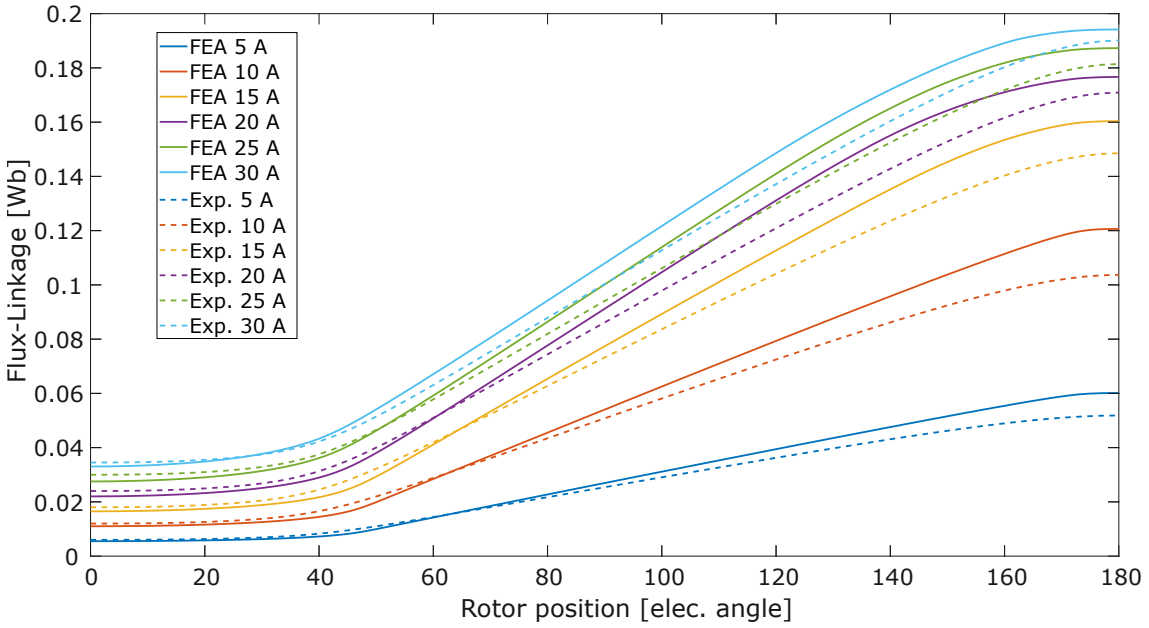

Figure 3.5: Flux-linkage comparison from FEA and experimental data

the machine control performance, where low inductance machines increase the control complexity, where short voltage pulse transients can cause high current spikes. The comparison between FEA and the experimental inductance profile is presented in Figure 3.6. It should be noted that the machine presents a symmetric characteristic; thus, only rotor angles from unaligned to aligned position (or vice versa) are required to model a complete electrical cycle.

$$L_k(\theta, i) = \left.\frac{\lambda_k(\theta, i)}{i_k}\right|_{\theta=const} \tag{3.2}$$

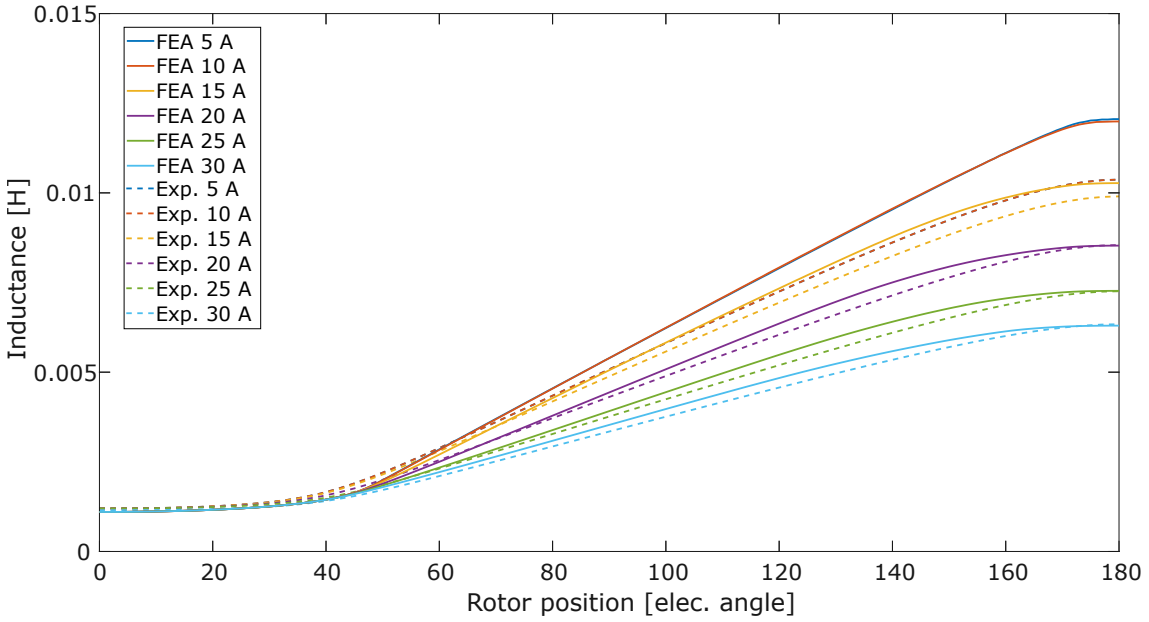

Figure 3.6: Inductance comparison from FEA and experimental data

3.3 Analytical Modeling

3.3.1 Linearized Model

Linearized models are more straightforward to be implemented, present low data allocation and low computational resources, but suffer from reduced model fidelity. Model linearization can be implemented using a trapezoidal model, which considers continuous phase current excitation for different rotor position angles. The self-inductance linear model can be constructed using the information of the aligned (L_{max}) and unaligned inductance (L_{min}). The angles for the model can be selected using (3.3). When considering the design of the four-phase 8/6 SRM, as presented in Figure 3.7 and Table 3.1, the angles for the linear model can be calculated considering the unaligned position (0°), initial alignment (48°), start fully aligned (174°), end fully

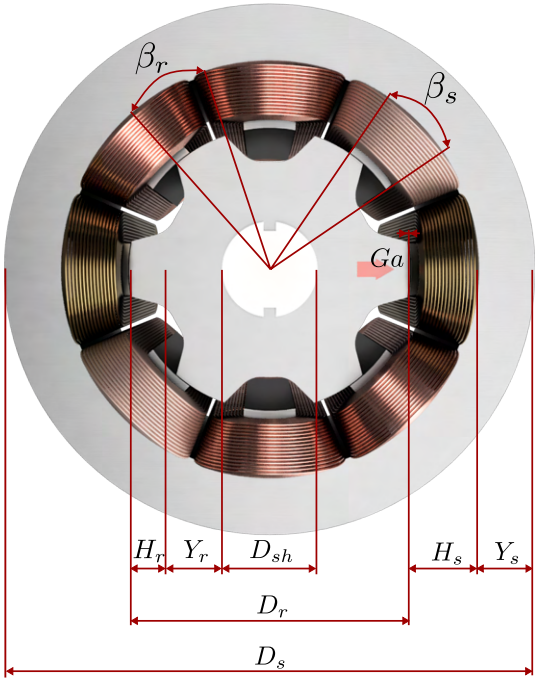

Figure 3.7: 8/6 SRM design specifications

aligned (186°), initial unaligned (312°), and unaligned (360°), where β_s is the stator pole arc angle, β_r is the stator pole arc angle, N_r is the number of rotor poles, and D_p is the arc length between two consecutive rotor poles.

$$
\begin{aligned}
D_p &= \frac{360 - N_r\beta_r}{N_r} \\
\theta_2 &= \frac{D_p - \beta_s}{2} N_r \\
\theta_3 &= \left(\beta_s + \frac{\theta_2}{N_r}\right) N_r \\
\theta_4 &= \left(\frac{\theta_3}{N_r} + \beta_r - \beta_s\right) N_r \\
\theta_5 &= \left(\frac{\theta_4}{N_r} + \beta_s\right) N_r
\end{aligned}
\tag{3.3}
$$

Symbol	Definition	Value
D_s	Stator outer diameter [mm]	170
D	Stator inner diameter [mm]	90
D_r	Rotor outer diameter [mm]	89.3
D_{sh}	Rotor shaft diameter [mm]	30
H_s	Stator pole height [mm]	23
H_r	Rotor pole height [mm]	10.15
β_s	Stator pole arc angle [deg.]	21
β_r	Rotor pole arc angle [deg.]	23
Y_s	Stator back iron thickness [mm]	17
Y_r	Rotor back iron thickness [mm]	19.5
Ga	Airgap [mm]	0.35

Table 3.1: Four-phase 8/6 SRM

The non-linear phase inductance obtained by FEA or experimental validation can be approximated using the linear models. There are several ways to represent the linearized characteristics of the machine, where additional steps can be added to improve the correlation between the non-linear and linear model. A single slope method is shown in (3.4), where only the aligned and unaligned positions are considered. The dual step method presented in (3.5) considers the initial alignment positions as a transition point. The triple slope technique shown in (3.6) presents an improved model fidelity at the cost of additional computational steps. All the methods present high deviation from the model under high saturation, where the flux path is non-linear at high currents due to the double-saliency nature of the machine. Figure 3.8 shows the comparison between common linearization methods when considering different saturation levels. The angles presented in (3.3) can be adjusted to compensate for the deviation caused by flux leakage, but requires additional steps on the modeling process, thus increasing complexity.

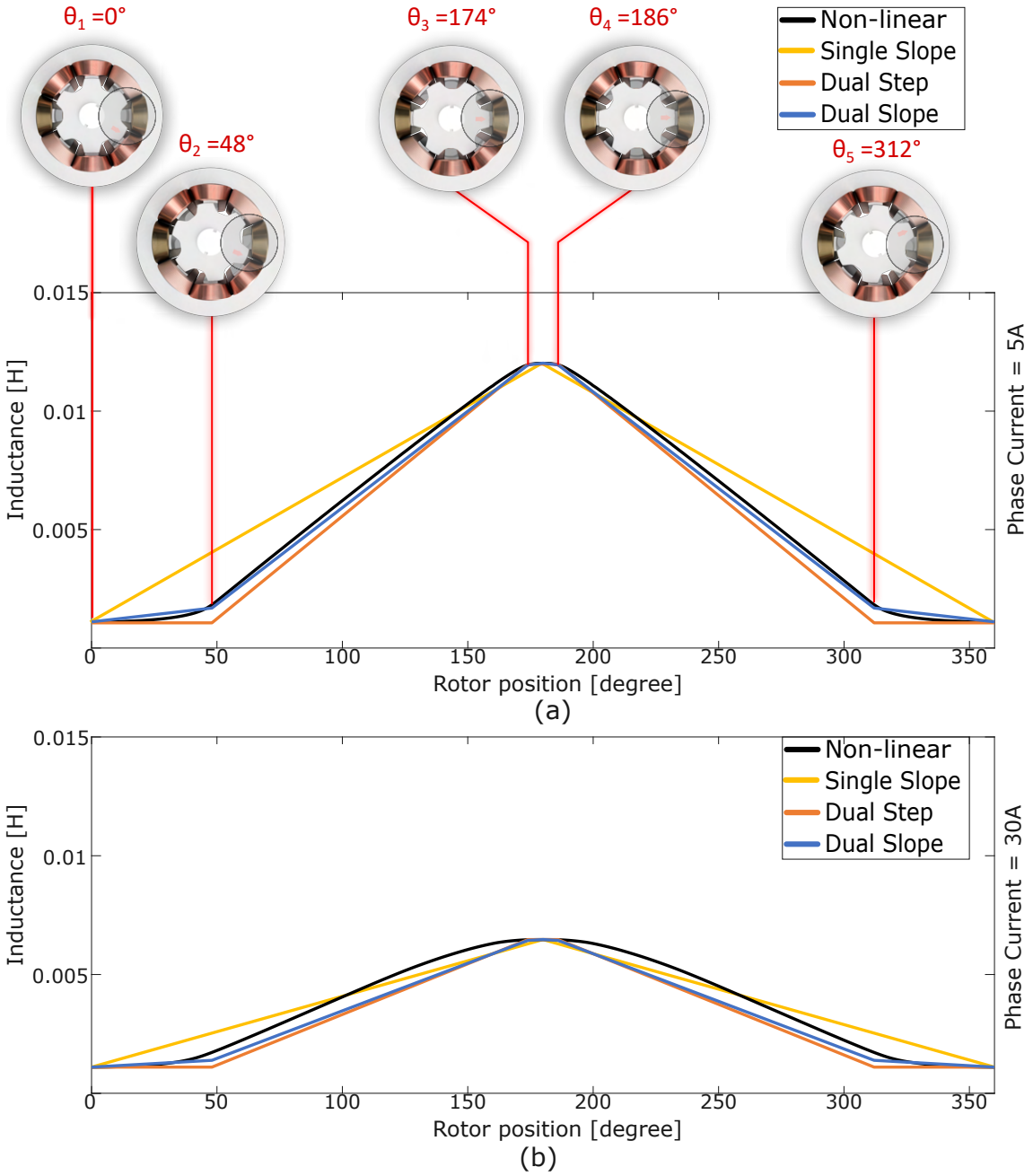

Figure 3.8: Linear model. a) Under 5A phase current, b) Under 30A phase current

$$L(\theta, i_k) = \begin{cases} \left(\frac{(L_{max}(i_k) - L_{min}(i_k))}{180}\right)\theta + L_{min}(i_k) & \text{if } 0 \leq \theta < 180 \\ \left(\frac{(-L_{max}(i_k) + L_{min}(i_k))}{180}\right)\theta + (2L_{max}(i_k) - L_{min}(i_k)) & \text{if } 180 \leq \theta < 360^\circ \end{cases} \tag{3.4}$$

$$L(\theta, i_k) = \begin{cases} L_{min}(i_k) & \text{if } \theta_1 \leq \theta < \theta_2 \\ \left(\frac{L_{max}(i_k) - L_{min}(i_k)}{\theta_3 - \theta_2}\right)\theta + L_{min}(i_k) - \left(\frac{L_{max}(i_k) - L_{min}(i_k)}{\theta_3 - \theta_2}\right)\theta_2 & \text{if } \theta_2 \leq \theta < \theta_3 \\ L_{max}(i_k) & \text{if } \theta_3 \leq \theta < \theta_4 \\ \left(\frac{-L_{max}(i_k) + L_{min}(i_k)}{\theta_5 - \theta_4}\right)\theta + L_{min}(i_k) + \left(\frac{L_{max}(i_k) - L_{min}(i_k)}{\theta_5 - \theta_4}\right)\theta_4 & \text{if } \theta_4 \leq \theta < \theta_5 \\ L_{min}(i_k) & \text{if } \theta_5 \leq \theta < 360^\circ \end{cases} \tag{3.5}$$

$$L(\theta, i_k) = \begin{cases} \left(\frac{L(\theta_2, i_k) - L_{min}(i_k)}{\theta_2}\right)\theta + L_{min}(i_k) & \text{if } \theta_1 \leq \theta < \theta_2 \\ \left(\frac{L(\theta_3, i_k) - L(\theta_2, i_k)}{\theta_3 - \theta_2}\right)\theta + L(\theta_2, i_k) - \left(\frac{L(\theta_3, i_k) - L(\theta_2, i_k)}{\theta_3 - \theta_2}\right)\theta_2 & \text{if } \theta_2 \leq \theta < \theta_3 \\ \left(\frac{L_{max}(i_k) - L(\theta_3, i_k)}{180^\circ - \theta_3}\right)\theta + L(\theta_3, i_k) - \left(\frac{L_{max}(i_k) - L(\theta_3, i_k)}{180^\circ - \theta_3}\right)\theta_3 & \text{if } \theta_3 \leq \theta < 180^\circ \\ \left(\frac{-L_{max}(i_k) + L(\theta_4, i_k)}{\theta_4 - 180^\circ}\right)\theta + L_{max}(i_k) + \left(\frac{L_{max}(i_k) - L(\theta_4, i_k)}{\theta_4 - 180^\circ}\right)180^\circ & \text{if } 180^\circ \leq \theta < \theta_4 \\ \left(\frac{-L(\theta_4, i_k) + L(\theta_5, i_k)}{\theta_5 - \theta_4}\right)\theta + L(\theta_5, i_k) + \left(\frac{L(\theta_4, i_k) - L(\theta_5, i_k)}{\theta_5 - \theta_4}\right)\theta_4 & \text{if } \theta_4 \leq \theta < \theta_5 \\ \left(\frac{-L(\theta_5, i_k) + L_{min}(i_k)}{360^\circ - \theta_5}\right)\theta + L_{min}(i_k) + \left(\frac{L(\theta_5, i_k) - L_{min}(i_k)}{360^\circ - \theta_5}\right)\theta_5 & \text{if } \theta_5 \leq \theta < 360^\circ \end{cases} \tag{3.6}$$

For different currents, the polynomial coefficients can be adjusted through a polynomial fitting to represent a wide current range. The order of the polynomial fitting can increase model accuracy at the cost of higher computational requirements.

3.3.2 Analytical Approximation Using Fourier Series

To overcome the problems presented by the linear approximation modeling, an analytical model using Fourier series expansion was proposed in [20], and implemented in [14, 21, 22]. Due to the phase inductance periodicity with respect to rotor position, the inductance profiles resemble a sinusoidal shape with a DC offset ($L_0(i)$), and can be modeled by a truncated Fourier series as presented in 3.7

$$L(\theta, i) = L_0(i) + L_1(i)\cos(N_r\theta + \varphi_1) + \sum_{k=2}^{\infty} L_k(i)\cos(k(N_r\theta + \varphi_k)), \tag{3.7}$$

where $L_k(i)$ are the inductance harmonics, φ_k is the phase shift, and N_r is the number of rotor poles.

For a four-phase 8/6 switched reluctance machine, it is observed that if one phase is at the aligned position ($L_a(i)$), there will be one unaligned phase ($L_u(i)$) and two phases at a mid-aligned position ($L_m(i)$), thus, the machine can be completely characterized using the inductances at these pre-defined positions. For a Fourier expansion truncated at the third term, 3.7 can be represented as 3.8.

$$L(\theta, i) = L_0(i) + L_1(i)\cos(6\theta + \varphi_k) + L_2(i)\cos(12\theta + 2\varphi_k) \tag{3.8}$$

Then, based on the machine geometry, 3.9 can be derived from 3.8.

$$\begin{aligned} L_a(i) &= L_0(i) + L_1(i)\cos(\varphi_k) + L_2(i)\cos(2\varphi_k) \\ L_m(i) &= L_0(i) - L_1(i)\sin(\varphi_k) - L_2(i)\sin(2\varphi_k) \\ L_u(i) &= L_0(i) - L_1(i)\cos(\varphi_k) + L_2(i)\cos(2\varphi_k) \end{aligned} \tag{3.9}$$

Referencing to the aligned phase (0°), 3.9 be represented in matrix form by 3.10

$$\begin{aligned} \begin{pmatrix} 1 & 1 & 1 \\ 1 & 0 & -1 \\ 1 & -1 & 1 \end{pmatrix} \begin{pmatrix} L_0(i) \\ L_1(i) \\ L_2(i) \end{pmatrix} &= \begin{pmatrix} L_a(i) \\ L_m(i) \\ L_u(i) \end{pmatrix} \\ \begin{pmatrix} L_0(i) \\ L_1(i) \\ L_2(i) \end{pmatrix} &= \begin{pmatrix} 0.25 & 0.5 & 0.25 \\ 0.5 & 0 & -0.5 \\ 0.25 & -0.5 & 0.25 \end{pmatrix} \begin{pmatrix} L_a(i) \\ L_m(i) \\ L_u(i) \end{pmatrix} \end{aligned} \tag{3.10}$$

The machine can be analytically represented using the aligned, unaligned, and mid-aligned inductances from FEA or experimental data for different current amplitudes. The truncated Fourier series expansion and the FEA data are compared in Figure 3.9.

For a complete analytical model, each coefficient $L_k(i)$ can be calculated by a polynomial expansion, where the model fidelity is proportional to the order of the polynomial fitting. As observed from Figure 3.9, when the machine operates under saturation, the inductance profile has a better match to the FEA, which is expected due to a higher magnitude of the low order harmonics. Higher-order polynomials for

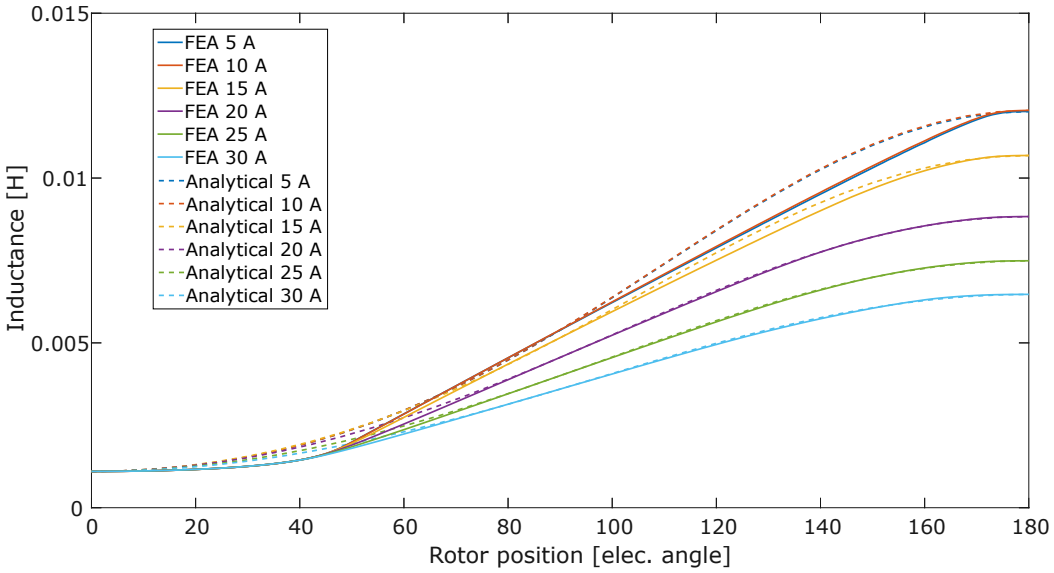

Figure 3.9: Analytical model using Fourrier Expansion compared to FEA

the truncated Fourier expansion need to be used to improve the analytical model, increasing the model complexity.

3.3.3 Least Square-Based Analytical Approximation

Polynomial regression models can be implemented to fit a general linear or non-linear set of data to an n^{th} degree polynomial equation, modeling the relationship between the target variables and the system's independent variables. If the number of data points is higher than the desired polynomial order, the system for coefficient determination is over-determined, meaning that there are more equations than unknowns. When the problem has no direct solution, the resulting polynomial can be approximated using a least square method, which minimizes the variance of the estimated coefficients, presenting a data-fitting polynomial model.

A least square-based analytical approximation (LSA) is proposed to improve the

model accuracy, presenting a reduction in system complexity compared to a high order Fourier series method. The inductance profile can be approximated by a polynomial regression model of order n by 3.11

$$L(\theta, i) = p_1(i)\theta^n + p_2(i)\theta^{(n-1)} + ... + p_n(i)\theta + p_{n+1}(i) + \varepsilon\big|_{i=const}\,, \tag{3.11}$$

where $p_1(i)$ to $p_{n+1}(i)$ are the unknown parameters for a constant current operation, θ is the independent variable, and ε is an unobserved random error with mean zero conditioned on the scalar variable θ. The problem can be arranged into a matrix-vector form, as shown in 3.12.

$$\underbrace{\begin{pmatrix} \theta_1^n & \theta_1^{n-1} & \cdots & 1 \\ \theta_2^n & \theta_2^{n-1} & \cdots & 1 \\ \vdots & \vdots & \ddots & \vdots \\ \theta_m^n & \theta_m^{n-1} & \cdots & 1 \end{pmatrix}}_{\mathbf{A}} \underbrace{\begin{pmatrix} p_1(i) \\ p_2(i) \\ \vdots \\ p_{n+1}(i) \end{pmatrix}}_{\mathbf{p}} + \underbrace{\begin{pmatrix} \varepsilon_1 \\ \varepsilon_2 \\ \vdots \\ \varepsilon_{n+1} \end{pmatrix}}_{\boldsymbol{\varepsilon}} = \underbrace{\begin{pmatrix} L_1(i) \\ L_2(i) \\ \vdots \\ L_{n+1}(i) \end{pmatrix}}_{\mathbf{b}} \tag{3.12}$$

Using the least square approximation, the vector of polynomial coefficients can be generated by 3.13.

$$\boldsymbol{p^*} = (\boldsymbol{A}^T\boldsymbol{A})^{-1}\boldsymbol{A}^T\boldsymbol{b} \tag{3.13}$$

The inductance analytical model is evaluated using different orders of polynomials, as shown in Figure 3.10.

Similar to the Fourier expansion, the least square-based method needs an additional polynomial expansion for each coefficient $p_1(i)$ to $p_{n+1}(i)$, where in the same

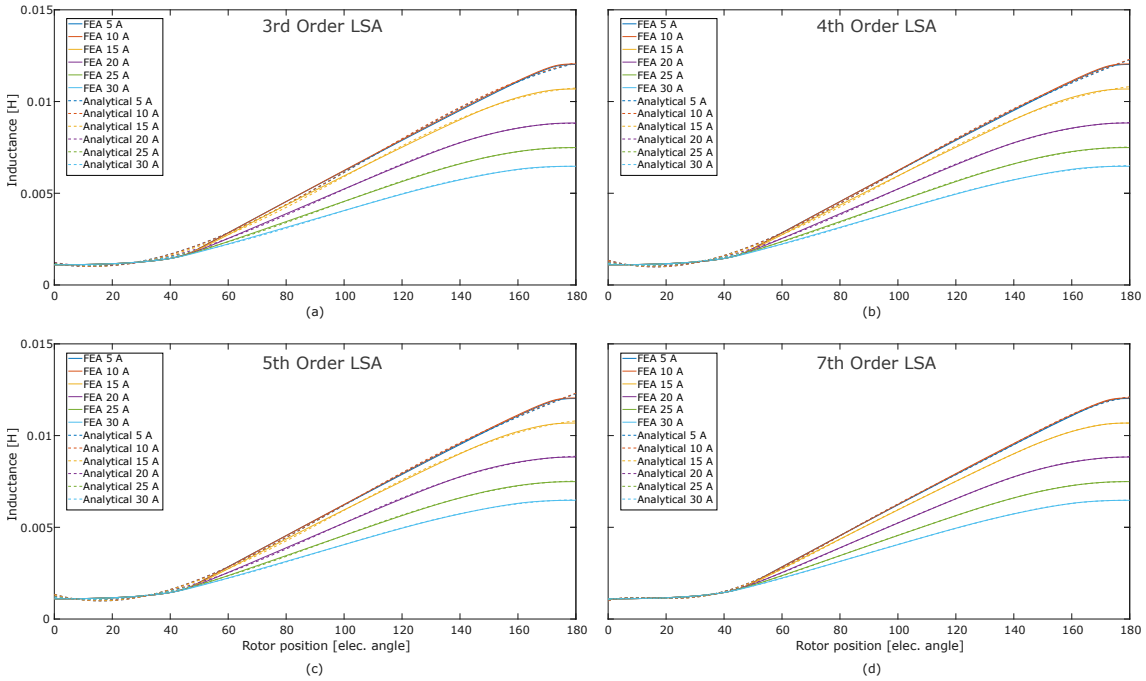

Figure 3.10: Analytical model using least square-based approximation compared to FEA. a) 3rd order polynomial approximation, b)4th order polynomial approximation, c) 5th order polynomial approximation, d) 7th order polynomial approximation

manner, the model fidelity is proportional to the order of the polynomial fitting.

3.4 Summary

To have an accurate model of the SRM, FEA or experimental validation can be used to characterize the machine. FEA is the common choice for motor design and evaluation, and can be used to define the expected performance and characteristics of the machine under different operating conditions. Unfortunately, the simulated values can deviate from the experimental validation since the 2D static electromagnetic simulation of the machine presents several assumptions, and the manufacturing process, including materials stress, mechanical tolerances, and assembly, are impossible to be precisely

modeled.

For optimal motor control, accurate machine representation is desired. There are several methods to properly represent the machine, which are mainly divided by LUT-based methods and analytical-based techniques. LUT-based methods present a simple solution and easy implementation, at the cost of high memory allocation. Analytical-based models are categorized by linearized and non-linearized methods. Linear approximation methods are simpler to implement, reducing the computational burden, but they can deviate from the real machine characteristics. The linearized methods can be represented by the single slope, dual step, and triple slope techniques. Non-linear modeling has the advantage of higher accuracy with an increase in complexity. The truncated Fourier expansion method and Least-square-based technique were presented, showing a reduction in the complexity when using the least-square-based technique while still improving the modeling accuracy. A comparison using a Root Mean Squared Error (RMSE) is shown in Figure 3.11

It should be noted that the analytical model deviation presented for the 8/6 SRM machine in this work might differ from other machines with different inductance or flux-linkage profile characteristics. The analytical model should be evaluated for each specific scenario and not as a one case fits all. When the machine is saturated, the analytical models present a better performance when compared to low-load conditions, which can be expected due to smoother inductance profile characteristics.

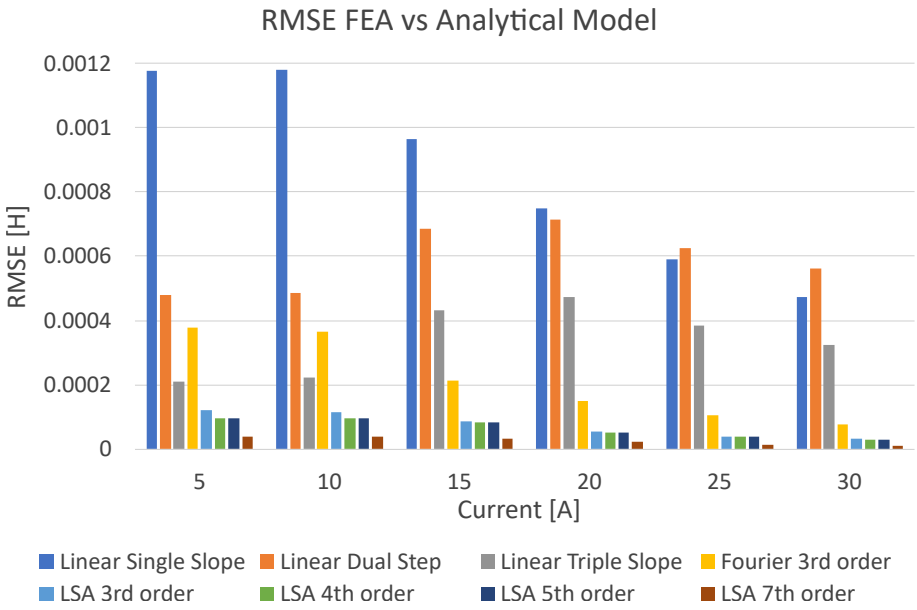

Figure 3.11: Analytical model using least square-based approximation compared to FEA. a) 3rd order polynomial approximation, b)4th order polynomial approximation, c) 5th order polynomial approximation, d) 7th order polynomial approximation

Chapter 4

Position Sensor Technology and Existing Sensorless Control Methods for SRMs

Precise information of the rotor position and speed is required for optimal control of electric machines, including SRMs, PMSMs, and IMs. The rotor position is commonly acquired using position sensors installed on the rotor or stator. A variety of sensors have been used in the industry depending on the reliability requirements, operating speed, precision, size, and mechanical installation, varying from low to high costs and low to high implementation challenges.

For applications that require a fail-safe operation, redundancy systems and premature fail detection are commonly used. System redundancy can drastically increase the costs, complexity, and system size, while a sensor fusion implementation with a decision-making algorithm needs to be implemented for failure detection. Therefore, this chapter reviews the position sensor technology for electric machines, presenting

the characteristics, advantages, and challenges. Besides, an analysis of the sensor failure modes and sensor failure detection is presented, showing the potential of sensorless control in fault detection and cost mitigation.

The chapter also reviews the position sensorless control methods proposed in the literature. The methods are classified based on the dependency of pre-defined machine magnetic characteristics or magnetic-parameter free methods, and the operating speed region, including startup, low-speed, and high-speed operations.

4.1 Position Sensor Technology

4.1.1 Hall-Effect Sensors

The Hall effect was first discovered by Edwin Hall in 1879 and is based on the Lorentz force law [23,24]. If a thin sheet of conductor or semiconductor material (Hall element) is perpendicularly placed into a magnetic field, and a current is flowing perpendicularly to the flux, by the Lorentz force law (4.1), a repulsion force to a certain angle is generated, creating a disturbance on the direction of the current

$$\overrightarrow{F} = q\left[\overrightarrow{E} + (\overrightarrow{v} \times \overrightarrow{B})\right] \tag{4.1}$$

where $\overrightarrow{F}$ is the Lorentz force, q is the charge moving with velocity $\overrightarrow{v}$, $\overrightarrow{B}$ is the magnetic flux density, and $\overrightarrow{E}$ is the electric field.

With the change in current distribution, the Hall voltage (V_{Hall}) is generated

perpendicular to both the field and the current ($\overrightarrow{I_E}$), as presented in (4.2) and Fig. 4.1

$$V_{Hall} \propto \overrightarrow{I_E} \times \overrightarrow{B} \tag{4.2}$$

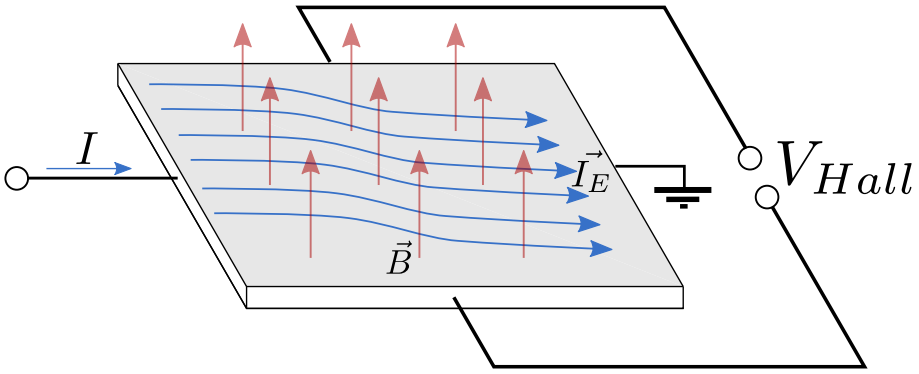

Figure 4.1: Hall operation principle

Due to the low amplitude of the generated voltage, the sensor has a signal conditioning circuit composed of temperature compensation, an amplifier, and a voltage regulator. There are two main commercial types of Hall effect sensors: Linear, which provides an analog voltage output, and Threshold type, which has a digital output signal.

Linear sensors provide a proportional output voltage depending on the strength of the magnetic field. The internal structure of the sensor is presented in Fig. 4.2. When there is no magnetic field applied, the output voltage has a fixed offset, which is achieved by a differential operational amplifier, making the voltage direction dependent on the orientation of the flux.

The threshold Hall-effect sensor is converted to digital by adding a Schmitt trigger to the previous circuit, which is used to compare the output of the differential amplifier with a preset reference as presented in Fig. 4.3. The digital output provides an

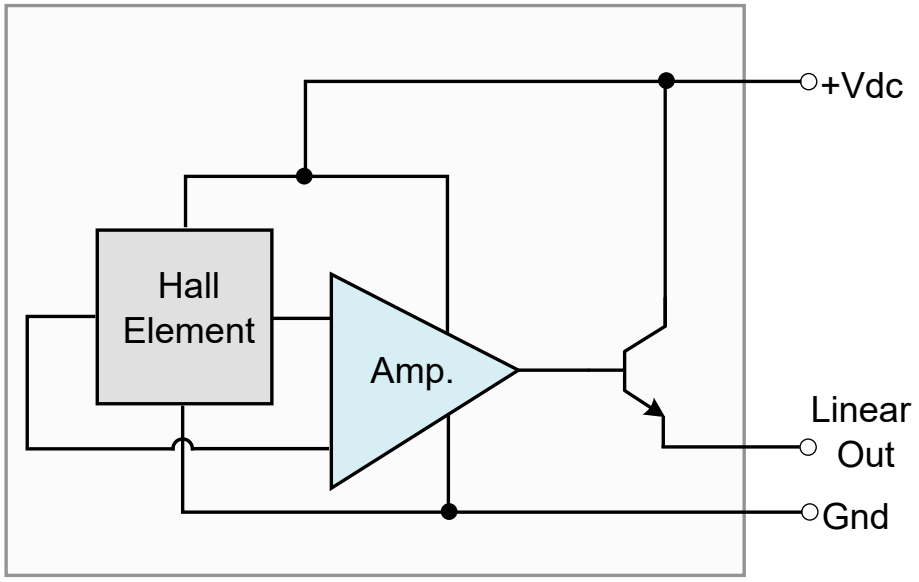

Figure 4.2: Linear Hall sensor

ON/OFF state depending on the field strength and polarity and can be configured as a latching device. The latching configuration can be implementing setting the device to an ON state when a south pole is detected, and OFF state at the north pole position.

Latching hall sensors are a low-cost solution for rotor position and speed measurements. For PMSMs, a common solution is to install an array of three hall sensors spaced by 120° electrical degrees. The rotor magnets are used to generate the magnetic field to the Hall sensors, and the sensor displacement gives a commutation pattern with eight possible states, where two states represent fault conditions Fig. 4.4. This type of configuration gives a low resolution of 60 electrical degrees, with a maximum variation of ± 30 degrees when a position shift is implemented. To improve position resolution during operation, a position extrapolation using the rotor speed information can improve the measurement, with some limitations at low speed and

under fast speed transients.

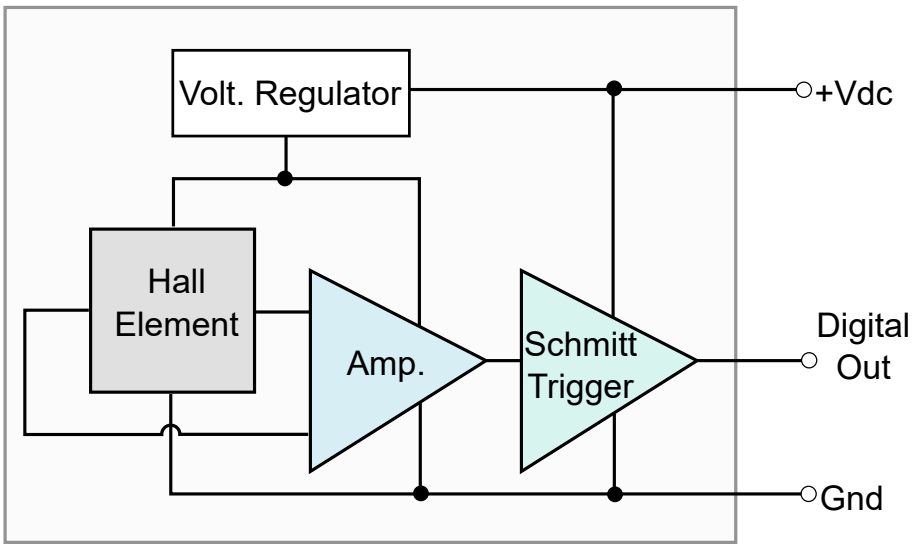

Figure 4.3: Threshold Hall sensor

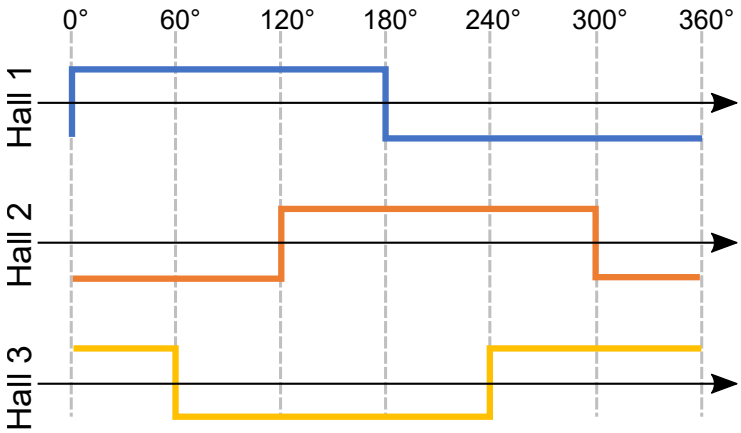

Sector	Hall state
0° - 60°	101
60° - 120°	100
120° - 180°	110
180° - 240°	010
240° - 300°	011
300° - 360°	001

Figure 4.4: Hall pulses and sector identification

Other than rotor position measurements, due to the simplicity and robustness of Hall-based sensors, they can also be found on safety systems like wheel speed sensors, drive-by-wire, and brake-by-wire pedals. For these applications, the field is generated

by a permanent magnet ring that provides pulses to the vehicle Electronic Control Unit (ECU) when the magnets pass the hall element. An absolute position value can be obtained if one of the magnets is removed from the ring, providing a zero position mark. An example of this implementation is presented in Fig. 4.5. Hall-based position sensors present a reliable solution due to their contactless nature, fast response, low cost, and small size. They do not need external signal processing or excitation signals, but they are not commonly used in electric and hybrid vehicles powertrains because of their low position resolution.

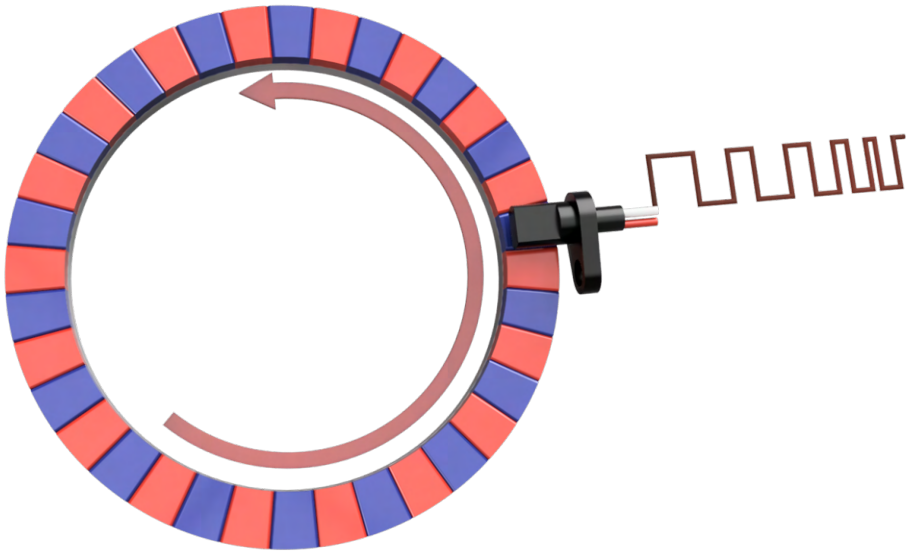

Figure 4.5: Hall effect sensor application using a permanent magnet ring.

4.1.2 Resolver

Resolvers are the go-to position sensors for automotive traction applications. They have great reliability, robustness, and good shock and vibration resistance. There are two main categories of resolvers: Brushed resolvers and Variable Reluctance resolvers (brushless). Brushed resolvers have a primary winding on the rotor and require slip

rings for rotor excitation, making this technology less reliable and less common in the automotive industry. The Variable Reluctance (VR) resolvers do not have a wounded rotor, presenting a simplified construction. It has all three coils positioned on the stator, where the primary is used for the excitation signal (reference coil), and the two secondaries are used for the position measurement (sine and cosine coils). The rotor is made of laminated steel and has a salient construction with a sinusoidal shape air gap, as shown in Fig. 4.6a, with the coil structure represented as Fig. 4.6b

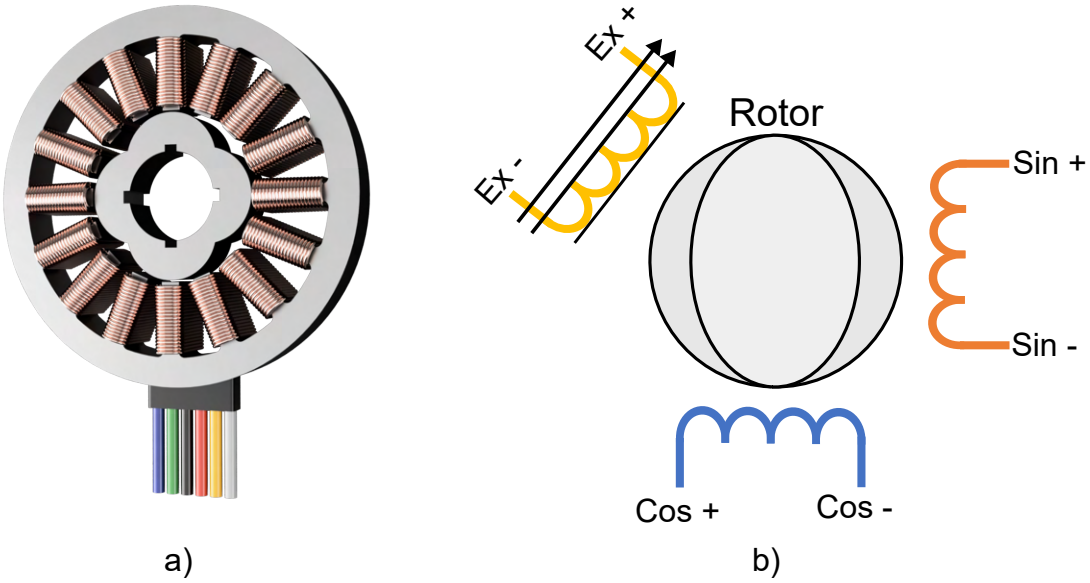

Figure 4.6: Resolver structure. a) rotor and stator b) coil configuration

The operation of the resolver consists of a high-frequency excitation signal applied to the primary coil, and because of the sinusoidal air gap shape of the rotor, it couples to the secondary coil as a sinusoidal variation signal [25]. The secondary coils are electrically displaced by 90°, generating an output signal that is phase-shifted by 90° in respect to each other. The input and output voltage of the resolver is represented

by (4.3)-(4.5)

$$V_{Ref} = E_0 sin(\omega_c t) \tag{4.3}$$

$$V_{Sin} = K E_0 sin(\omega_c t) sin(\theta) \tag{4.4}$$

$$V_{Cos} = K E_0 sin(\omega_c t) cos(\theta) \tag{4.5}$$

where E_0 is the excitation voltage magnitude, ω_c is the high-frequency sinusoidal carrier signal, K is the transformation ratio between primary and secondary, and θ is the resolver electrical angle. Because the output signals are trigonometrically related, the rotor position information is given by $\theta = \arctan(V_{sin}/V_{cos})$. The signal must be filtered and demodulated, which intrinsically inserts a speed-dependent phase lag. A position observer is one of the few methods that can be used to extract the position information and presents a simple and easy implementation on a microcontroller without the need of a dedicated IC [26]. The observer block diagram is presented in Fig. 4.7.

A bandpass FIR filter can be used to eliminate noise, offsets, and variations on the feedback signal, where the pass band is from $(\omega_c - 2\omega_r)$ to $(\omega_c + 2\omega_r)$, where ω_r is the maximum shaft speed. It should be noted that the accuracy is increased using higher sampling frequency and lower bandwidth. The bandpass filter can improve accuracy but not completely eliminate jitters, so an extra filter is needed.

To demodulate the signal, the ADC decimation is implemented to capture the cycle peaks, where the sampling is synchronized with the carrier, and the demodulated

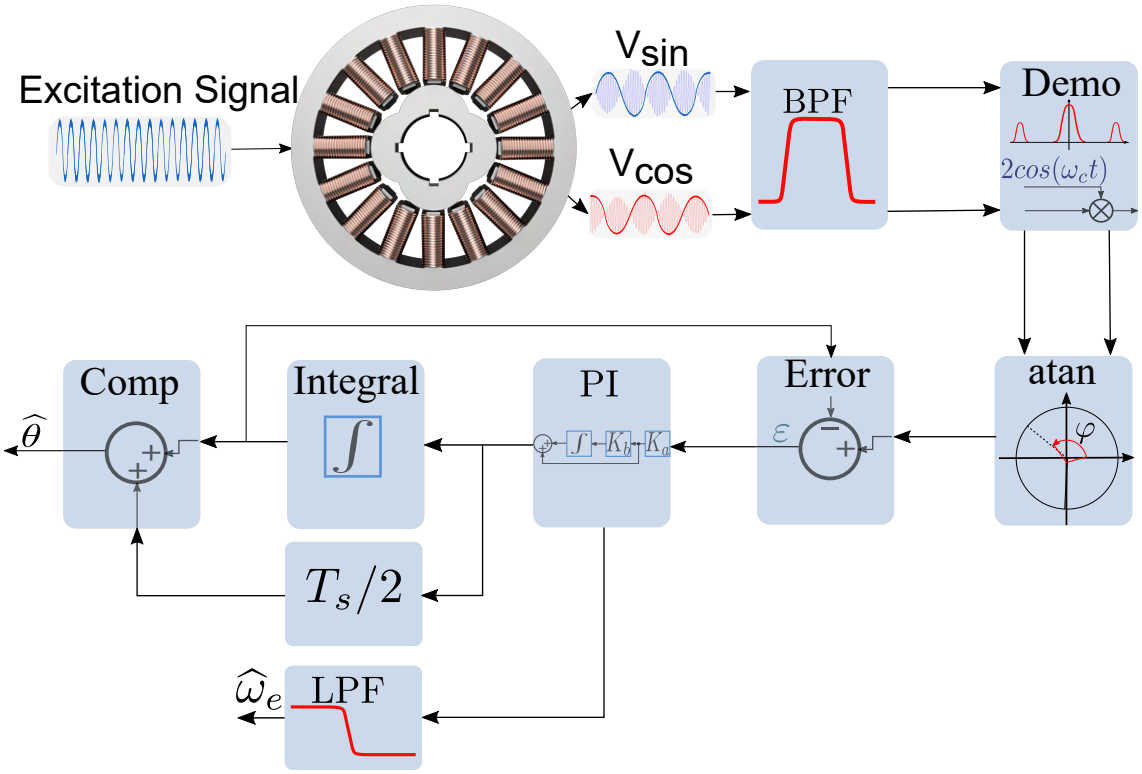

Figure 4.7: Resolver control diagram

signal frequency corresponds to the shaft speed.

The error signal is calculated by (4.6), and is used on the Phase Locked Loop (PLL)

$$\theta_{error} = \arctan\left(\frac{V_{sin}}{V_{cos}}\right) - \widehat{\theta} \tag{4.6}$$

The error can be filtered using a first-order low-pass filter, and the output can be compensated using a delay compensation block $T_s/2$, where T_s is the carrier sampling time.

To implement this method on a microcontroller, the resolver excitation is generated using a sinusoidal PWM signal and filtered in two stages to eliminate the

harmonic content. The sine and cosine feedback is filtered and scaled to fit the ADC range [26]. This type of implementation can eliminate the use of dedicated resolver-to-digital converter ICs like the AD2S1210 from Analog Devices, the PGA411-Q1 from Texas Instruments, or the RAA3064002GFP/RAA3064003GFP from Renesas Electronics, reducing the implementation costs but adding extra complexity and increasing the number of used GPIOs.

Resolvers have the advantage of high accuracy, high resolution, and high reliability and robustness in harsh environments. The main limitation of resolvers is the high costs, additional weight that causes additional rotor inertia, the need for a moderate space for installation, external signal conditioning and excitation signal circuits, and a limited speed operation, which is defined by the excitation signal frequency.

4.1.3 Magnetoresistive-effect sensor

The anisotropic magnetoresistive-effect (AMR) was first discovered by William Thomson [27] in 1857, which has similar working principles as the hall-effect sensor [28,29], and is also based on the Lorentz force law.

It was observed that the resistivity of ferromagnetic materials changed when the angle between an external magnetic field and the direction of the current was changed. This technology was applied only a century after the discovery and became popular on reading heads of magnetic hard disks [30]. Due to the low cost, robustness, and simplicity, it can be found in a wide range of applications, including the automotive segment. In 1988 this effect was observed in thin ferromagnetic films [31], and because the change in the magnetoresistance was much larger than the AMR, it was called giant magnetoresistive-effect (GMR). Development of new technologies has been made

like tunneling (TMR) or colossal (CMR) magnetoresistive sensors [32], but the AMR and GMR are the main types of magnetoresistive-effect sensors used in industry. When considering the AMR, the resistivity (ρ) changes depending on the angle (θ) between the orientation of the internal magnetization and the direction of the electric current as shown in (4.7)

$$\rho(\theta) = \rho_{\perp} + \frac{\Delta\rho}{\rho_{\parallel}} \cos^2\theta \tag{4.7}$$

where $\rho_{\perp}$ and $\rho_{\parallel}$ are the resistivity for $\theta = 90°$ and $\theta = 0°$, respectively, and $\Delta\rho/\rho_{\parallel}$ is the magnetoresistive coefficient, which is a reference of the magnetoresistive performance of the device. For the rotor position and speed measurements in electric machines, the sensors are designed to react to a strong magnetic field, reducing interference impact from the motor magnetic field. To compensate for temperature drifts and to generate a quadrature output, the magnetoresistive elements are combined into two Wheatstone bridges, where the second bridge has a 45° orientation, as presented in Fig. 4.8, enabling a quadrature signal, as shown in (4.8). The output signal is unambiguous in a range of 90°, providing an output measurement of 180°.

$$\theta = \frac{1}{2} \arctan\left(\frac{V_{sin(2\varphi)}}{V_{cos(2\varphi)}}\right) \tag{4.8}$$

The GMR uses a multilayer structure of ferromagnetic and non-ferromagnetic materials, interchangeably positioned, as presented in Fig. 4.9a, where the orientation of the magnetization of the ferromagnetic layers are antiparallel on the initial state, when there is no external magnetic field applied, and are forced to alignment when there is an external magnetic field applied. Their resistance dependency is presented

be Fig. 4.9b, and defined by (4.9)

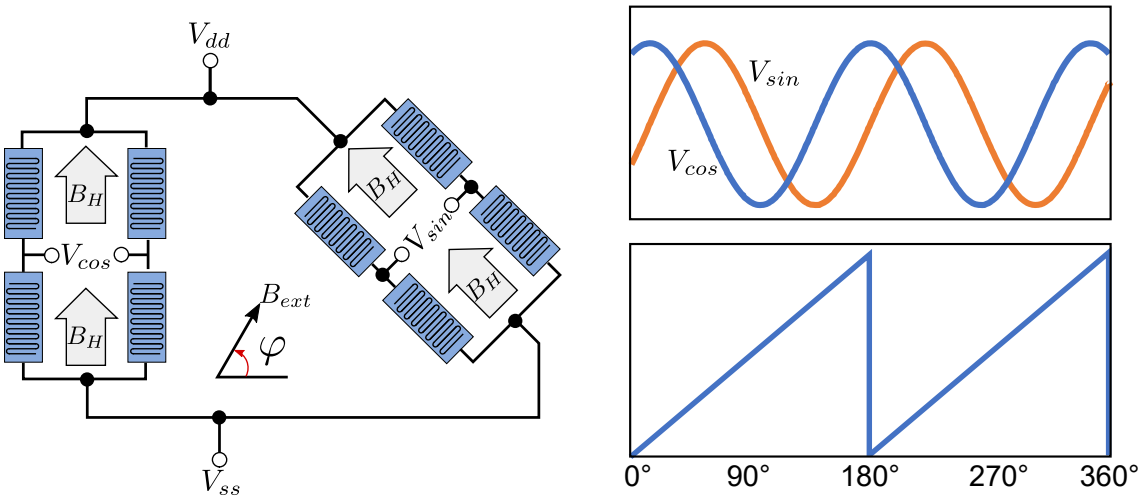

Figure 4.8: AMR sensor bridge circuit and output signal

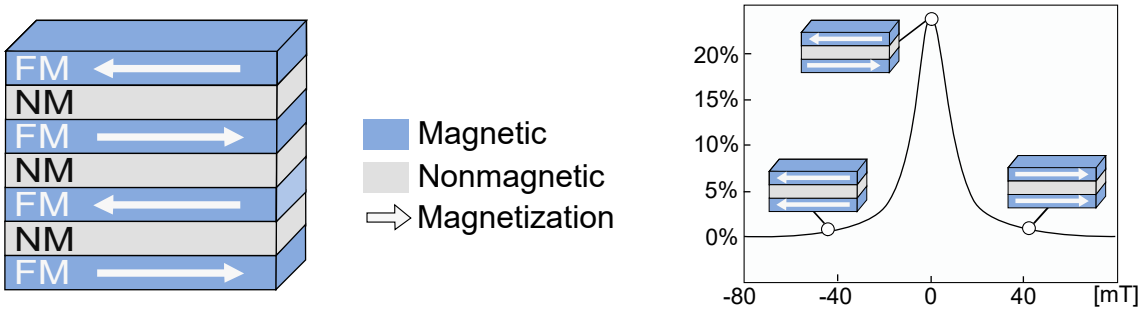

Figure 4.9: GMR operation

$$GMR = \frac{\rho_{ap} - \rho_p}{\rho_p} \tag{4.9}$$

where ρ_{ap} and ρ_p are the anti-parallel and parallel resistivity. Due to the GMR characteristics, the resistivity is proportional to the cosine of the angle (θ) of the

applied external magnetic field, as presented in (4.10)

$$\rho = \rho_{ap} - \Delta\rho\cos(\theta) \tag{4.10}$$

For rotor speed and position measurement, the GMRs are structured in a similar way as the AMR, by using two Wheatstone bridges, but with the bridges orthogonally oriented to each other, as shown in Fig. 4.10, providing a 360° measurement.

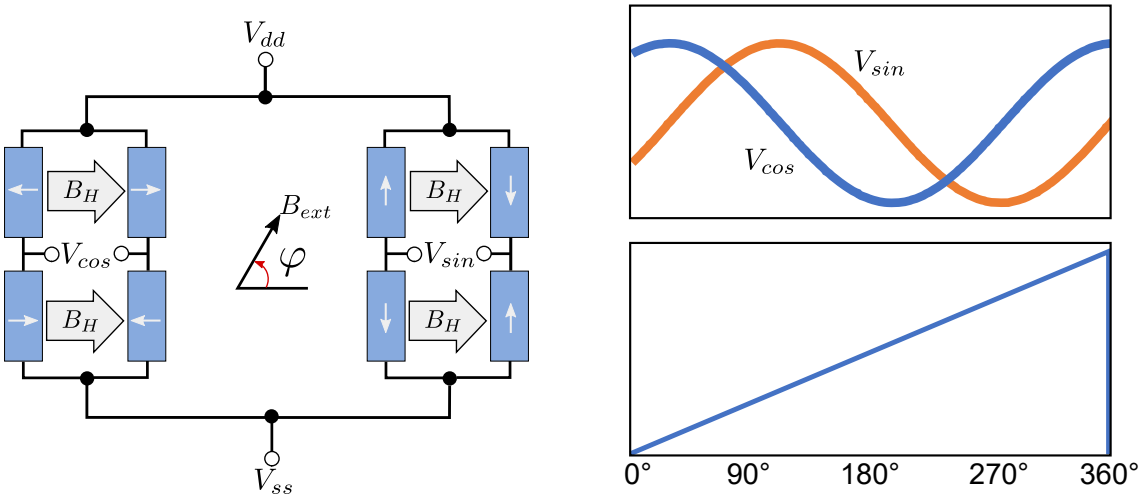

Figure 4.10: GMR circuit and output signal

The rotor position is measured by the magnetic field's orientation, determined by the resistance-dependent voltage. GMR sensors are robust against temperature changes and present a higher measurement signal, requiring magnets with lower field strength. For system redundancy, it is possible to have a combined GMR and AMR in the same package, like the TLE5309D from Infineon. The material and position of the magnets are essential in the design, where the magnets need to be magnetized diametrically and accurately aligned orthogonal to the sensing element. For the angular rotor position measurements, the end of the shaft and off shaft are possible

configurations [29], as presented in Fig. 4.11

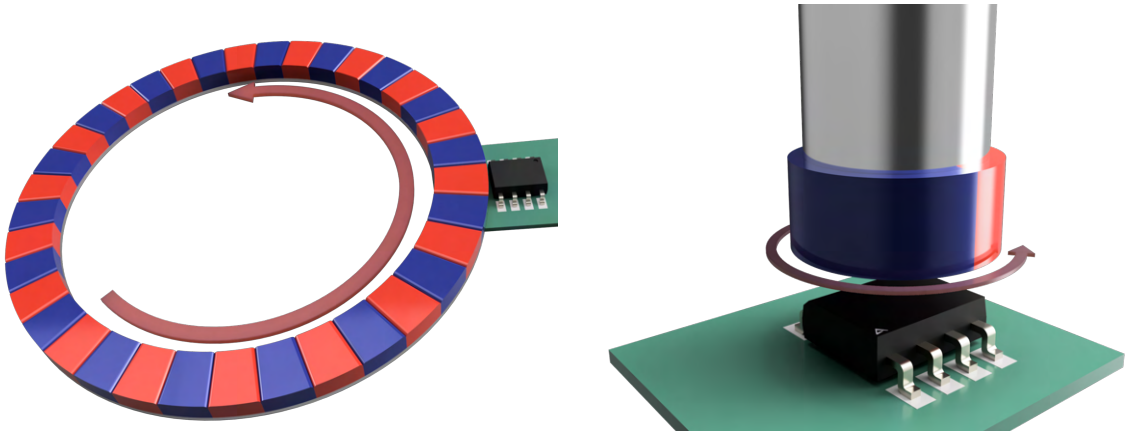

Figure 4.11: Magnetoresistive sensor implementation. a) off-shaft magnet configuration, b) end of shaft configuration

The AMR/GMR sensor design is susceptible to accuracy problems in the presence of mechanical variations, including eccentricity and air gap variations. The main advantages of this sensor technology are the reduced space needed for installation, accuracy, high-speed operation, and low costs.

4.1.4 Encoder

Encoders are one of the most common position sensors in industry and are used in several applications to convert a linear or angular mechanical motion to analog or digital signals. There are different encoder constructions, including the conductive encoder, magnetic encoder, and optical-based encoder. Optical encoders are the industry standard. They operate via a perforated disk with a distinct pattern that allows or blocks the light passing through it. A photosensitive sensor produces a digital or analog signal when the light passes through the disk.

Encoders can be categorized by absolute or incremental encoders. Absolute encoders can provide the absolute rotor position and are manufactured using multiple perforated rings (code rings) with different binary weights, providing data information of the position rater then single pulses. This encoder presents a high cost and complexity, especially for high-resolution types, and is applicable to solutions where homing the machine to a known position is not feasible, including electric machines used in traction application. The output data can be analog or digital, depending on the requirements

An incremental encoder does not report the absolute position when powered on. Optical encoders are constructed using a perforated disk with two (A and B) or three (A, B, and Z) output digital signals. The A and B signals operated in quadrature, similarly to the resolver previously presented, which can indicate the direction of rotation, and the pulsed frequency indicates the rotational speed. To sense the position of the rotor shaft, a third signal can be added (Z), which is presented as the index. The index produces a single pulse every 360° mechanical and is used as an absolute rotor position at that particular angle. The quadrature output of the incremental encoder is presented in Fig. 4.12.

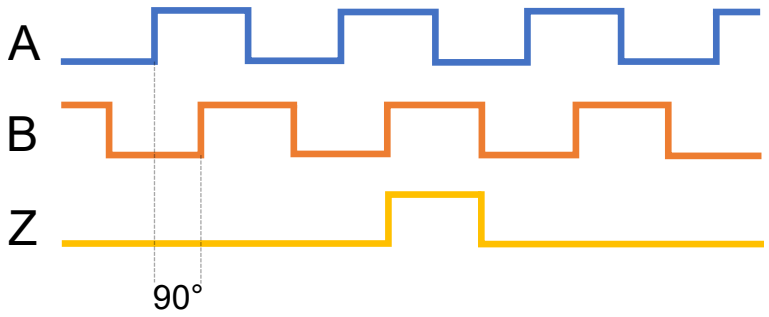

Figure 4.12: Quadrature output - incremental encoder

The rotor position resolution is dependent on the number of pulses per revolution

(ppr), and can be calculated as (4.11)

$$\theta_{inc} = \frac{2\pi N_{count}}{(ppr)}, \tag{4.11}$$

where N_{count} is the electrical pulses counter. The speed (ω) is then calculated by (4.12)

$$\omega = \frac{2\pi \Delta N_{count}}{T_{enc}\ (ppr)}, \tag{4.12}$$

where T_{enc} and ΔN_{count} are the sample time and the number of pulses between two sample times, respectively.

4.2 Position Sensor Failure Modes

Position sensor failure detection or early identification of near-to-failure sensors are crucial for the safe operation of electric machines, where some types of failures can present an unexpected dangerous operation. When a position sensor is identified, proper controls can be implemented to mitigate the fault, where in some cases, an under-fault operation can be triggered to improve system dependability.

For rotor position sensors, there are several types of possible failures. Complete outage failures are commonly easy to detect, and failure detection is usually implemented on a hardware level, where significant anomalies or signal loss are directly identified. Other types of failures do not present a simple identification procedure and are more challenging to be detected without a hardware redundancy, including loss of accuracy, offset and drift.

Analog position sensors, including resolver and AMR/GMR sensors, are prone to

loss of accuracy when the signal has additional noise or disturbances, discretization problems, mechanical variations, and hardware faults. The most common source of errors are signal phase shift, amplitude mismatch, fast accelerations, and offset.

Amplitude mismatch of the sine/cosine signal can be introduced on resolvers by variation in the resolver windings, which can happen during the manufacturing process, winding faults, or by the gain between the resolver and the ADC input. (4.5) can be modified to (4.13) to account for the amplitude mismatch [25]

$$V_{cos} = K(1+\delta)E_0 sin(\omega_c t)cos(\theta) \tag{4.13}$$

where δ is the percentage of amplitude mismatch from cosine signal relative to the sine. The error in radians can be represented by (4.14)

$$\varepsilon = \frac{\delta}{2}\sin(2\theta) \tag{4.14}$$

The error oscillates twice per cycle, with maximum amplitude at odd integer multiples of 45°, and is zero at multiples of 90°.

Other sources of error can be present, including differential phase shift and phase shift between the excitation signal and the sine/cosine signals. Depending on the amplitude of the error, it can cause variations in the speed estimation, variations in the current control, and system instability.

Rotor position sensors need to be compensated for position offsets during the initial setup, where the absolute rotor position needs to match the mechanical position of the sensor. Position offset problems can happen during changes in the hardware configuration or under mechanical faults. This type of failure can present serious

operation problems, including wrong commutations, inefficient operation, or reverse rotor direction.

Hardware redundancy can drastically increase manufacturing costs and system complexity; thus, software-based solutions are usually implemented. Several methods were proposed in the literature for rotor position sensor fault identification, especially when implemented on permanent magnet machines. Due to the fast response characteristics, the methods are mainly implemented as observer-based algorithms. Some of the methods proposed for synchronous and asynchronous machines are the Luenberger observers [33,34], Sliding Mode Observer (SMO) [34,35] Model Reference Adaptive System Observer (MRAS) [36–38], and Extended Kalman Filter [39, 40].

The Luenberger observers are simpler to be implemented and present a low computational demand, but outside its bandwidth, it presents low robustness to parameter variations. SMO, MRAS, and EKFs present higher robustness at the cost of increased complexity and convergence constraints. However, besides all these specific considerations, every observer approach needs an auxiliary source of information, and these additional signals are not always available. Sensorless control algorithms can present a viable solution on rotor position fault identification and the capability of sensor fusion application.

4.3 Position Sensorless Control

Switched reluctance motors (SRMs) present a simple and reliable construction, but to properly control the machine, the system is highly dependent on an accurate rotor position information. Position sensors, such as encoders, resolvers, Hall-effect sensors, magnetoresistive-effect sensors, or position measurement circuits [41–43] are

commonly used for position detection. However, the position sensor can potentially increase the overall volume of the machine, decrease system reliability, dependability, and lead to an increase in manufacturing costs. Additional manufacturing steps are required for the position sensor implementation, and when fault-tolerant requirements for critical systems are specified, the effects of electromagnetic interference, temperature, and vibration must be mitigated. Position sensorless algorithms can eliminate sensor-related issues and can be used for fault detection and sensor fusion technology. When considering low-cost applications, additional costs of sensors and the required circuit could be prohibited; thus, position sensorless control presents a viable alternative.

A classification of different sensorless techniques was proposed in [44] and further extended in [1], and [45]. Different position estimation methods can be categorized by their operating speeds, passive or active methods, and computationally intensive techniques. An additional classification is done in [46] by identifying if the method is parameter-dependent or parameter-free. An updated version of different sensorless control techniques is shown in Figure 4.13.

When considering the operating speed, position estimation methods can be categorized by standstill and low-speed sensorless controls, and high-speed sensorless techniques. At standstill and low speeds, the magnetic characteristics of the machine have a low or null back-EMF, which reduces the signal-to-noise ratio of the estimation algorithms, making the techniques unobservable, especially when considering the introduction of noise and discretization of the acquired data. Thus, by injecting a high-frequency signal into the idle phases, the magnetic quantities can become observable, making the sensorless control feasible at zero and low speeds. The magnetic

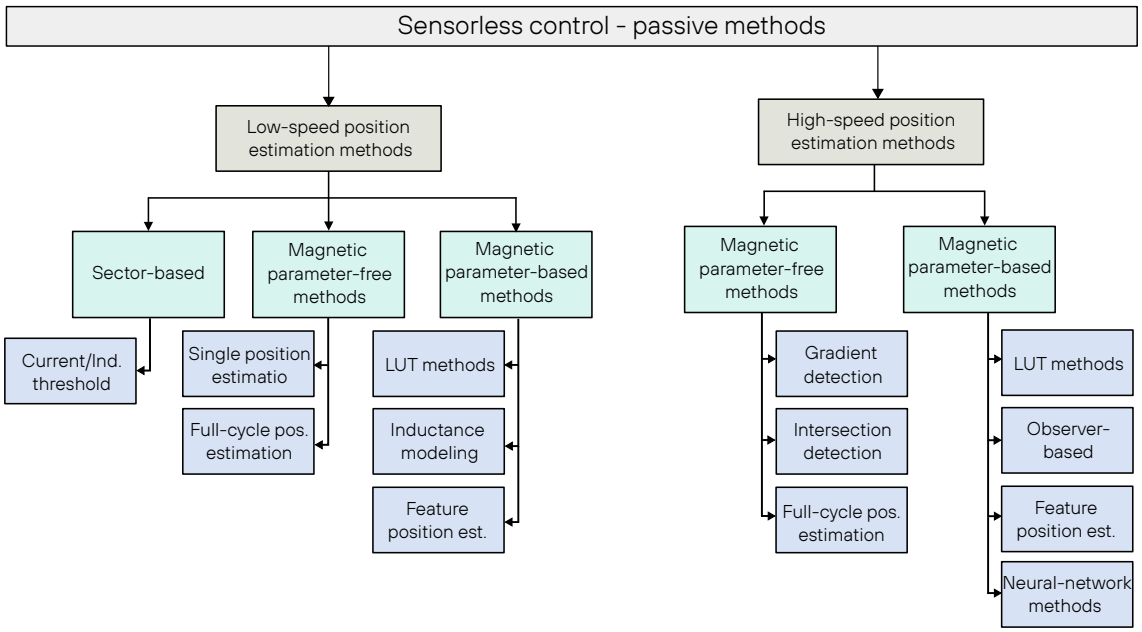

Figure 4.13: Classification of position sensorless control algorithms

characteristics can be obtained using the energized phases during commutation for high-speed operation, where the large back-EMF provides a high SNR.

Passive methods do not rely on additional hardware, using only the information of the terminal voltage, the phase current, and motor characteristics. Active estimation schemes require additional hardware [41–43, 47, 48], and are commonly implemented injecting a high-frequency signal into the inactive phases, where the induced current is measured, and the calculated inductance is used on the position estimation. Active methods are not commonly used in industry due to the additional hardware and high deviations at medium to high speeds. Computationally intensive methods, such as observer-based and neural networks, require high computational resources but present high robustness or model independence when compared to the previous methods.

4.3.1 Standstill and Low-Speed Sensorless Control

For a smooth and reliable start of the machine, rotor position information is required for proper phase commutation. For standstill startup, simultaneous pulse injection are widely implemented, as presented in [45,49–55]. The magnitude of the induced phase current or the phase inductance amplitude is used for sector identification. The sector is defined as a range of possible rotor positions and is directly proportional to the number of phases. Since the inductance is a periodic function of rotor angle, it has a maximum and a minimum value on the aligned and unaligned positions, respectively. To identify the initial sector of the rotor, all the phases are simultaneously excited with the same voltage pulse $V_{ph}\Delta t$, and the phase inductance can be calculated using (4.15). For a four-phase SRM, the electrical period can be divided into eight different sectors, with a 45° electrical degrees range, as shown in Figure 4.14. The phase located at the region of positive torque is selected as the initial driving phase. This method can be implemented in any SRM, but is only feasible at zero-speed conditions. An extended method using a single-current threshold was proposed in [50], where the initial rotor position can be identified when the rotor is rotating using the time for the current to reach a predefined threshold and the inductance calculation to estimate the commutation sector.

$$L_\theta = V_{ph}\frac{\Delta t}{\Delta i} \tag{4.15}$$

The sector identification is a crucial step for the excitation and sensing phase selection and is commonly implemented during the start of low-speed estimation methods. Low-speed sensorless control techniques rely on high-frequency pulses injection into

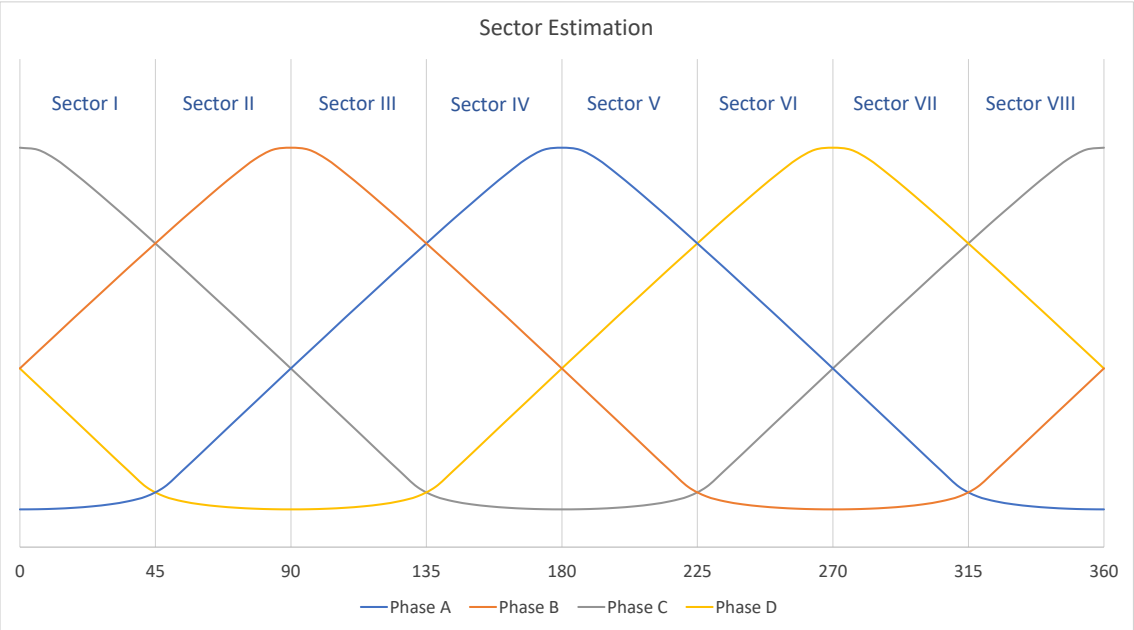

Figure 4.14: Inductance profile and sectors

the non-energized phases (sensing phases), with a voltage amplitude adjusted by the gate duty cycle, creating this way an induced high-frequency current signal. The rotor position-related induced currents are used for the flux-linkage-based or inductance-based sensorless control techniques. Low-speed position estimation can be categorized by sector-based methods, parameter-free-based methods, and parameter-based methods, as shown on Figure 4.13.

4.3.1.1 Sector-based methods

Sector-based methods do not estimate the exact rotor position, only the sector information for phase commutation. The two-current threshold method [49] is based on voltage pulse injection on idle phases and predefined thresholds. A low-current threshold is located close to the aligned position, where the inductance is higher, and

Phase Current	**Phase Ind.**	**Sector**	**Rotor Pos.**	**Sens. Ph.**
$I_A > I_D \geq I_B > I_C$	$L_C > L_B \geq L_D > L_A$	Sector I	0° to 44°	I_B
$I_D > I_A \geq I_C > I_B$	$L_B > L_C \geq L_A > L_D$	Sector II	45° to 89°	I_C
$I_D > I_C \geq I_A > I_B$	$L_B > L_A \geq L_C > L_D$	Sector III	90° to 134°	I_A
$I_C > I_D \geq I_B > I_A$	$L_A > L_B \geq L_D > L_C$	Sector IV	135° to 179°	I_B
$I_C > I_B \geq I_D > I_A$	$L_A > L_D \geq L_B > L_C$	Sector V	180° to 224°	I_D
$I_B > I_C \geq I_A > I_D$	$L_D > L_A \geq L_C > L_B$	Sector VI	225° to 269°	I_A
$I_B > I_A \geq I_C > I_D$	$L_D > L_C \geq L_A > L_B$	Sector VII	270° to 314°	I_C
$I_A > I_B \geq I_D > I_C$	$L_C > L_D \geq L_B > L_A$	Sector VIII	315° to 359°	I_D

Table 4.1: Initial rotor position identification and low-speed sensorless control of a four-phase SRM

the induced current produced by the injected voltage signal is smaller, which is used to define the sensing phase changes. A high-current threshold is located close to the pole alignment position and used to select the conduction phase.

This technique output signal is similar to a hall-effect-based control, where the rotor position is identified as sectors and not as precise angles, with the drawback of not having a precise position point, as is the case of hall-based position sensors. The two-current threshold method can control the machine under zero and low-speed operations, and does not need all-phase pulse injection during regular operation. A summary table for the four-phase 8/6 SRM is presented in Table 4.1.

Sector-base methods have very simple implementation and are independent of machine parameters, but they cannot estimate the rotor position, relying only on sector identification.

4.3.1.2 Parameter-free-based methods

Using only the sector information is not an optimal solution for high-performance SRM controls, where torque and current regulation require precise rotor position information. The rotor position can be extracted from the machine phase inductance, which can be calculated from the high-frequency induced currents at low speed. Machine parameter-free-based methods present an advantage of not needing the magnetic characteristics of the SRM, which can drastically reduce the implementation time of sensorless control on different machines since motor characterization and commissioning are not required.

The parameter-free-estimation algorithm relies on the assumption of a sinusoidal inductance characteristic, which was shown in section 3.3.2 to be a good approximation. A general diagram of the full-cycle position estimation at low speed is presented Figure 4.15. The phase inductance calculated from the induced currents is transformed using a Clark transformation, which can then be used to derive the sin-cos functions and estimate the rotor position using the arctangent calculation, similar to what is done in AC machines.

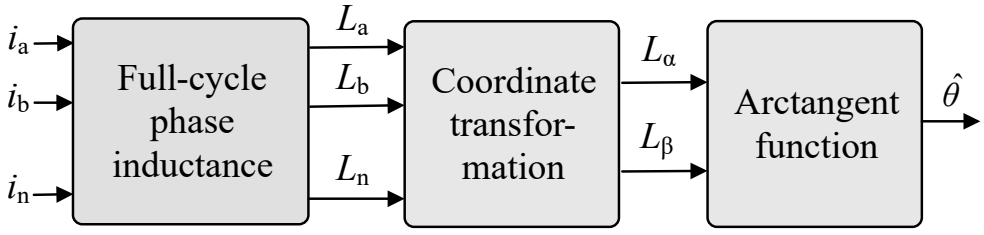

Figure 4.15: General diagram for the low-speed parameter-free-based methods

This method was implemented in [56] on a three-phase 12/8 SRM, to estimate the

initial position using the sinusoidal inductance profile, and the work was further modified in [54] to reduce modeling errors. In [57], the same technique was implemented for a low-speed operation, where the inductance from the idle and conducting phases was used on the rotor position estimation. The incremental inductance calculation from the induced currents for the turn-ON and turn-OFF periods present implementation advantages since the voltage drop and back-EMF can be canceled as presented in (4.16). The methods can be extended to multi-phase machines by changing the coordinate transformation algorithm.

$$\begin{aligned} L_{inc}(\theta) &= \frac{2V_{inj}}{\Delta i} \\ \Delta i &= \left.\frac{di}{dt}\right|_{ON} - \left.\frac{di}{dt}\right|_{OFF} \end{aligned} \tag{4.16}$$

Although the method presents advantages for not requiring the pre-defined data of the machine parameters, the inductance calculation is independent of the current amplitude, which can present high deviations when operating under saturated conditions.

4.3.1.3 Parameter-based methods

Parameter-based methods use an *a priori* information of the machine characteristics and present a superior position estimation accuracy and performance when compared to the sector-based and parameter-free-based techniques. The main drawback of these methods is the need for the machine's pre-defined magnetic characteristics, which can be acquired using the methods in Chapter 3.

Several parameter-based methods are presented in the literature, categorized as

LUT-based techniques, linear inductance methods, non-linear model-based algorithms, and feature-based methods.

LUT-based methods use pre-stored inductance information to estimate the rotor position. The inductance can be calculated using the current information from the injected signal, as presented in (4.15), and compared to an inductance-current-position dependent lookup-table, as shown in [58, 59], where the input data is the calculated inductance and current, and the output information is the rotor position. Since the excitation phase for the SRM is discontinuous, a logic algorithm needs to be implemented to get the full-cycle information. A simplified algorithm for a four-phase 8/6 SRM is shown in Figure 4.16, where 90° regions are considered for each phase. The estimation method's performance depends on the accuracy of the LUT and the measurement of the high-frequency induced current. This method has an additional drawback of extra memory allocation requirements for the pre-stored LUT.

Linear inductance methods use the linear model approximation presented in section 3.3.1. The region from the initial alignment to start fully alignment presents an unsaturated linear characteristic when operating in constant current conditions, which can be used for the position estimation methods [45,50,60–62]. The inductance calculation of the high-frequency pulse on the idle phases can be used to estimate the rotor position. In [45], a simplified version of (3.6) was implemented, where the rotor

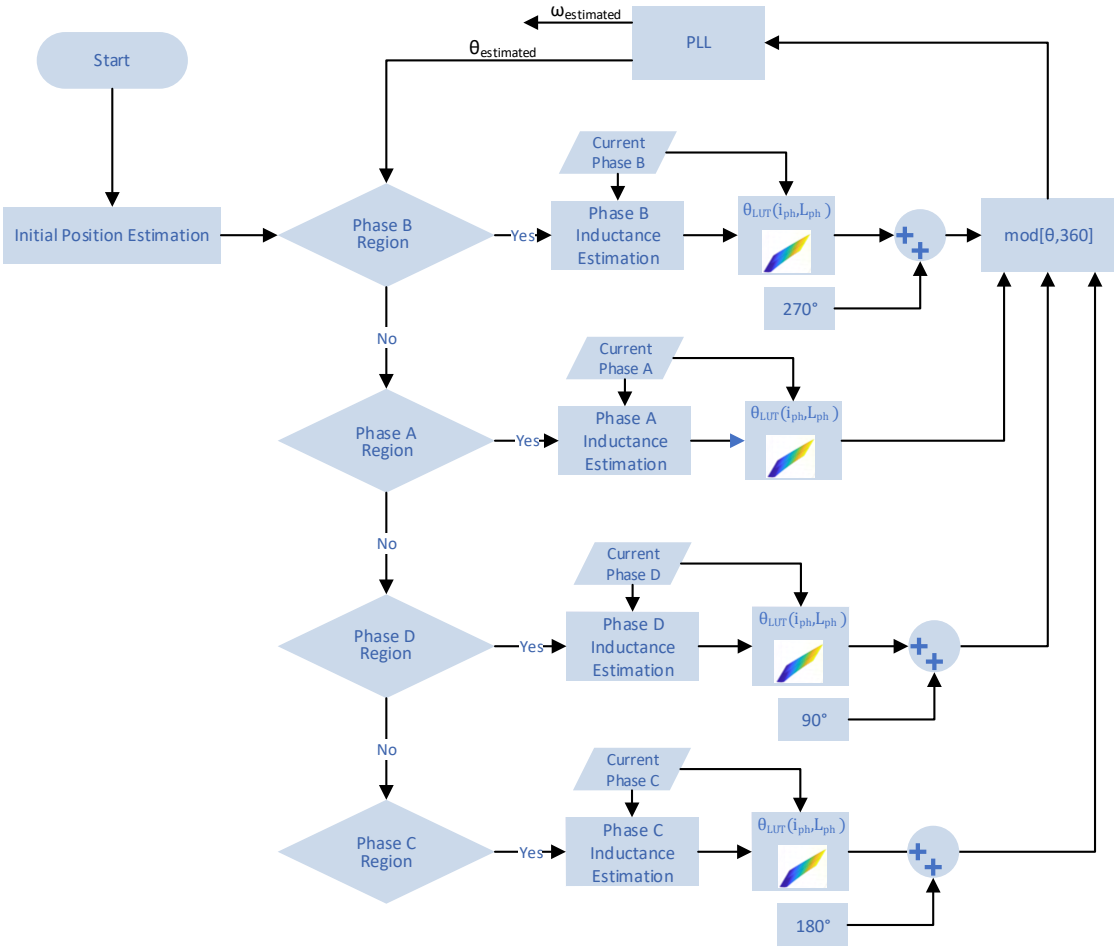

Figure 4.16: General diagram for the low-speed LUT-based methods

position can be estimated by (4.17) and (4.18) for a four-phase SRM

$$L(\theta,i_k)=\begin{cases}\left(\frac{L(\theta_3,i_k)-L(\theta_2,i_k)}{\theta_3-\theta_2}\right)\theta+L(\theta_2,i_k)-\left(\frac{L(\theta_3,i_k)-L(\theta_2,i_k)}{\theta_3-\theta_2}\right)\theta_2 & \text{if } \theta_2\leq\theta<\theta_3\\ \left(\frac{L_{max}(i_k)-L(\theta_3,i_k)}{180°-\theta_3}\right)\theta+L(\theta_3,i_k)-\left(\frac{L_{max}(i_k)-L(\theta_3,i_k)}{180°-\theta_3}\right)\theta_3 & \text{if } \theta_3\leq\theta<180°\end{cases} \tag{4.17}$$

$$\begin{aligned} \widehat{\theta} &= \frac{L_{max}(i_k) - L(\theta, i_k)}{N} + \theta_{initial} \\ N &= \frac{L_{max}(i_k) - L_{min}(i_k)}{90^\circ}, \end{aligned} \tag{4.18}$$

where θ_2 and θ_3 are the initial alignment to start fully alignment positions, i_k is current, N is the phase inductance slope, and $\theta_{initial}$ is the initial position value compensation. Similar to the LUT-based methods, the injected current and inductance calculation is discontinuous, and the information of all phases is required for a full-cycle estimation, as shown in Figure 4.17.

An improved work proposed in [60] extends the linear method to a three-phase unbalance inductance case. In [45], the inductance slope was considered only on the unsaturated region, where the inductance was independent of the current amplitude i_k. In [61], the author obtained the unsaturated inductance from the saturated incremental inductance under load conditions, where the mapping utilizes a second-order polynomial approximation.

The linear methods can be further extended to non-linear cases when considering the truncated Fourier series expansion presented in Chapter 3 section 3.3.2. In [21], the DC and first harmonic content were used to estimate the rotor position through an arccosine function. The work presented in [22, 63] extended the Fourier model to the second harmonics, improving the position estimation accuracy.

Feature position estimation methods use only the machine's partial inductance characteristics at predefined rotor positions. This can reduce memory allocation and computational burden compared to LUT-based methods and non-linear model-based algorithms, respectively, at the cost of lower accuracy, ultra-low speed operation

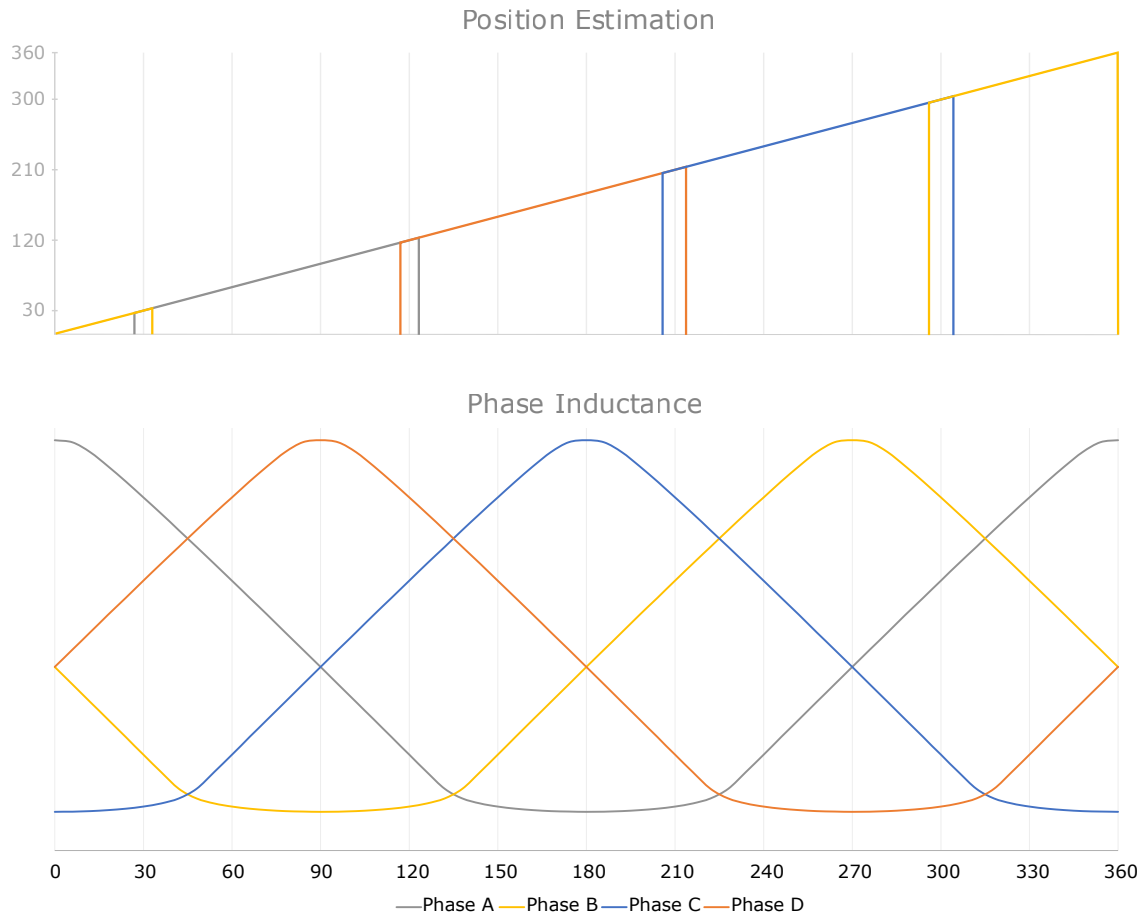

Figure 4.17: Discontinuous phase estimation for low-speed sensorless control techniques

problems, and inability to estimate the initial rotor position. The main limitation of the feature position estimation methods is the low resolution of the position estimation since only limited position points are detected over one electrical cycle, where it uses a similar concept of the sector-based methods, relying on a higher number of current/inductance thresholds to estimate the rotor position as presented in [53, 64, 65].

4.3.2 Position Estimation at High Speed

Low-speed estimation methods rely on high-frequency voltage injection to correctly estimate the rotor position, presenting a low performance at high speeds due to limited periods for pulse injection. Injection-based controls are often required to have a narrow operating region due to an additional torque ripple generation, acoustic noises, and additional losses. At high speeds, the electrical quantities of the SRM become observable, and high-speed sensorless control algorithms can be implemented. High-speed position estimation methods can be categorized by parameter-free and parameter-based methods.

4.3.2.1 Parameter-free sensorless control

Magnetic parameter-free methods can present a good solution when the machine characteristics are not pre-defined, drastically reducing the commissioning time and machine characterization during product development, especially considering manufacturing processes can cause noticeable deviation from the FEA model, as shown in section 3.2.

Sector-based algorithms are mainly used for the rotor speed estimation, and present similarities from the low-speed sector-based methods. In [66], the sector is identified by the intersection points of phase inductances during conduction, and a logical relationship of the phase inductance amplitude is used for the sector identification.

A current-gradient method is proposed in [67], and is applicable to the single pulse operation region, where the DC-link voltage regulates the current gradient. The phase

current has a non-linear shape during commutation on single pulse operation, where it only increases from the unaligned to the beginning of alignment position, and presents a null current derivative at the beginning of alignment of the rotor and stator pole. This feature position can be used for rotor position detection without the need for pre-defined magnetic characteristics of the machine. However, this method can present problems under magnetic saturation, where the rotor position can present a phase-shift, and a stored compensation table is needed for proper position estimation [65]. Inductance gradient methods [68] can be used to identify when the rotor and stator are at an aligned position, where the inductance value presents the peak value, and the inductance gradient is null. The gradient methods present a simple implementation and parameter independence; however, they are sensitive to measurement noises and have a discontinuous operation, reducing machine performance.

4.3.2.2 Parameter-based sensorless control

The control performance at high-speed operation can be significantly improved using parameter-based algorithms. Pre-defined information of the position-related flux-linkage or inductance profile of the machine is required for the position estimation algorithms. The parameter-based methods can be categorized by LUT-based algorithms, observer-based methods, feature position estimators, and neural-network-based techniques.

LUT-based methods present simple implementation and good tracking performance at the cost of high memory allocation of pre-stored information of the machine. The position information can be extracted using a singular relationship between flux-linkage or inductance information, and the rotor position angle. In [69], the sensorless

control was implemented using the flux-linkage information of the machine, where the flux-linkage LUT was inverted as a function of phase current, directly estimating the rotor position as a function of current and flux, as shown in Figure 4.18. Since the rate of flux variation with respect to the position change is reduced on the aligned and unaligned positions, there is an accuracy reduction in these regions. This implementation presents very high memory requirements, where a single LUT used in this work required 64kb of memory. LUT-based methods can present limitations at low to mid-speed operation, where high deviations can occur due to the accumulated error during flux calculation. A resistance estimator is proposed in [69] to extend the estimation speed range. Considering the flux-linkage at the end of the phase excitation period (T_0) is zero, the phase resistance can be estimated as (4.19).

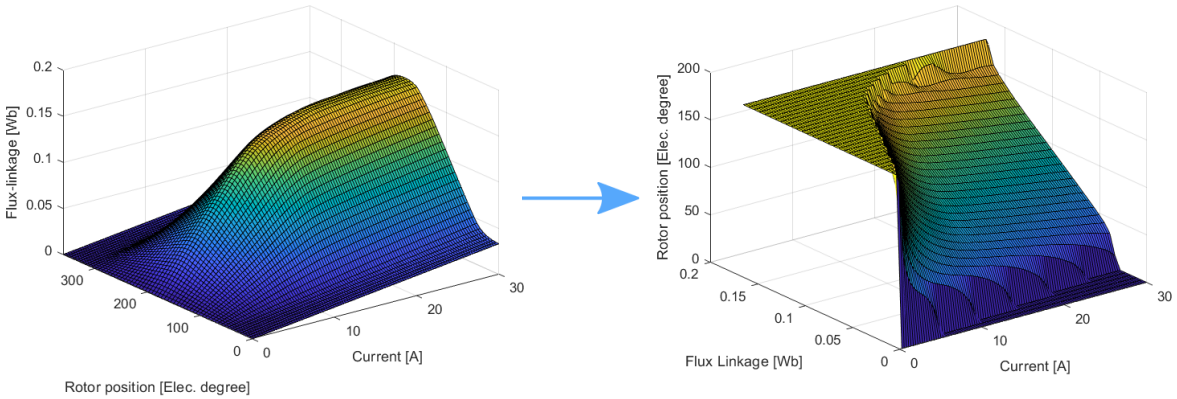

Figure 4.18: Rotor position as a function of current and flux-linkage

$$\lambda_{ph} = \int_0^{T_0} U_{ph}(t)dt - R\int_0^{T_0} i_{ph}(t)dt = 0|_{t=T_0}$$
$$R = \frac{\int_0^{T_0} U_{ph}(t)dt}{\int_0^{T_0} i_{ph}(t)dt} \tag{4.19}$$

In [70], a method was developed to avoid pure integrations, which can improve the estimation accuracy and parameter sensitivity, and in [71], an off-line mutual-coupling compensation table was proposed to compensate the errors of flux calculation.

Position observers can present an excellent alternative to the parameter uncertainties and distortions, mitigating the problems of easurement and sampling noises that can affect the performance of LUT-based methods. The rotor position can be indirectly estimated, providing good filtering capability and higher reliability. The position estimation observers present a structure of prediction error correction between measured data and predicted data, which can be estimated by the SRM analytical model. Different observers can be identified by the estimator type, including sliding-mode observer (SMO), Extended Kalman-filter-based observers (EKFO), and model reference adaptive systems (MRAS) [45, 72–74].

Sliding-mode observers present excellent dynamic performance and have been extensively researched for SRM sensorless control. The observer uses state-space functions based on a high gain nonlinear controller, usually implemented using a sign or sat function, driving the state variables to reach a predefined sliding surface. This method presents low steady-state errors and fast convergence, but since perfect surface tracking is hard to be implemented due to the nonlinear switching function and high gains, the SMO suffers from chattering problems during estimation. To mitigate chattering, low-pass filters can be used to remove the fast oscillations, but this solution can limit the system's dynamic performance, as previously discussed, and can lead to a large phase delay and system instability.

Extended Kalman-filter-based observers have also been implemented in the literature [73, 75], and provide exceptional performance in filtering noises and model

uncertainty, but are still limited in practical application due to high computational requirements, complex parameter calibration, and low performance at ultra-high speeds. The MRAS methods use machine analytical models to compare with measured data. The error is then used to force the estimation to converge to the actual value, which is commonly employed using a proportional-integral (PI) controller. Since this method is based on a PI loop, the convergency rate is highly dependent on the bandwidth design of the controller, which can be hard to design due to the high nonlinearities of the SRM.

The main challenge with magnetic parameter-based sensorless control is the increase in memory allocation for the magnetic characteristics of the machine. To overcome this issue, methods based on neural networks (NN) have been widely researched in a variety of applications, including position estimation algorithms for switched reluctance motors [76–79]. The NN uses a data set generated from the magnetic characteristics of the machine, which is done offline. The data is used to generate a mapping from the electrical input such as flux-linkage, inductance, and currents, which can present good performance results with reduced memory and computational requirements; however, these methods require a high number of training sets to reduce the estimation errors and improve performance, which can extend the validation and development time in commercial applications.

4.3.3 Challenges in Commercial Applications

The main challenges for SRMS rotor position estimation in a commercial application are the limitations of each presented method and the machine construction.

First, since the SRM does not have permanent magnets into the rotor cores, no flux

is produced when the coils are not energized; therefore, it is impossible to estimate the rotor position during free-wheeling operation, limiting the effectiveness of the system depending on the application. This issue can be mitigated if a pulse is injected into the idle phases, but this technique increase losses, acoustic noise and produces additional negative torque, which is not always acceptable. The initial rotor position estimation during no standstill positions is challenging to implement, especially at high speeds.

Second, a four-quadrant operation, represented by a rotation direction change, motoring to generation change, or both, can be challenging for SRM sensorless control. Since sensorless control algorithms are based on logic implementation, the motoring to generation region, or vice-versa, present implementation complexities to adapt to the change in the commutation angles. For the quadrant change regarding the rotation direction, the zero-crossing is challenging since the speed error estimation at close to zero speed is proportionally high, causing possible system instabilities in this region.

Third, memory allocation and computing power are limited in low-cost applications, where high-performance DSPs are usually price prohibitive. SRMs greatly rely on LUT-based approaches for optimal control, including angle optimization, acoustic noise reduction LUTs, and torque ripple minimization. An additional LUT for sensorless control could become a challenge. Computational burden is also a limiting factor when implementing high-performance methods, so algorithm optimization must be implemented.

In addition to the mentioned challenges, the operation using position estimation methods needs to be reliable. Changes in machine parameters like eccentricity, which can be caused by bearing faults, changes in inductance that inter-turn shorts of the windings can cause, and changes in the overall characteristics of the machine that can

happen during the manufacturing process can present a big challenge for the sensorless implementation. All these problems need to be identified during the control system development and mitigated to provide safe control, low manufacturing costs, high performance, and high reliability for commercial applications.

4.4 Summary

Position sensorless control for electric machines has been of interest to researchers and industry due to their elimination of rotor position sensors, overall costs reduction of the system, position sensor failure identification, under-fault operation, and high reliability. To better understand the implementation challenges and limitations of rotor position sensors, a comprehensive analysis of different sensors was presented, showing the advantages and disadvantages of each implementation.

The fail-safe, under-fault, and premature failure mitigation are important topics in the industry. The position sensor failure modes like complete outage, loss of accuracy, position offset, and drift are presented in this work, providing a good understanding of the importance of sensorless control algorithms on rotor position fault detection, under-fault operation, and possible use in sensor fusion application.

The second part of this chapter presents the different methods of position sensorless control. These strategies were classified according to a particular speed operation or dependency of the machine's pre-defined magnetic characteristics. Table 3.1 summarizes the main sensorless control techniques.

A general overview of the challenges in commercial applications is then presented.

Categories	**Sensorless Method**	**Magnetic Charac.**	**Low-speed**	**High-speed**	**Advantages**	**Disadvantages**
Sector-based	Threshold based method [49]	No	Yes	No	Robust in running conditions	No position estimation, sector only
	Intersection detection [66]	No	No	Yes	Simple implementation	Noise sensitivity and no position estimation
Magnetic parameter-free	Continuous estimation [54,56,57]	No	Yes	No	Continuous estimation	Unavailability with load
	Gradient detection [65,67,68]	No	No	Yes	Simple implementation	Single pulse operation only, noise sensitivity and discontinuous operation
Magnetic parameter-based	Pulse injection LUT-searching [58,59]	Yes	Yes	No	Simple implementation	Large storage space and noise sensitivity
	Pulse injection linear inductance [45,50,60-62]	Yes	Yes	No	Low memory requirement	Low estimation accuracy, noise sensitivity and increased complexity in saturation cases
	Pulse injection inductance-model [21,22,63]	Yes	Yes	No	Low memory requirement	Low estimation accuracy
	Pulse injection feature position estimation [53,64,65]	Yes	Yes	No	Low computational burden	Discontinuous operation, low accuracy and no initial position estimation
	LUT-based [69-71]	Yes	No	Yes	Simple implementation	Large storage space and noise sensitivity
	Observer-based [45, 72-75]	Yes	No	Yes	Low noise sensitivity	Complex implementation
	Neural-network [76-79]	Yes	No	Yes	Low memory requirement	High offline training and large training set

Table 4.2: Summary of position estimation methods proposed in the literature

Chapter 5

Proposed Unified Nonlinear Optimization-Based Method for a Wide Speed Operation

Rotor position estimation in SRMs for the low and high-speed operations has been discussed in Chapter 4. From the presented review, position observer-based sensorless control methods can present high robustness to non-ideal distortions, such as current measurements, sampling noises, and parameter uncertainty, which highly affect the LUT and feature position estimation methods. Position-sensorless control techniques early discussed are effective for a narrow speed region, either low speed or high speeds, but not both. For wide-speed operation, several techniques were proposed in the literature by combining both the low-speed method and the high-speed methods, including the hysteresis [21] and linear switching control [80]. However, they present stability challenges since two different methods need to be combined for a wide-speed operation. An additional computation load is required during the transition

between methods since the two processes need to be running simultaneously during the transition.

This chapter presents a unified wide-speed range optimization-based sensorless control algorithm for switched reluctance machines for a wide-speed operation. In this method, a cost function is defined from the machine voltage equation, where the phase voltage and current information are used as inputs, and the rotor position is extracted from the position-dependent inductance profile. Short voltage pulses are injected in all phases for the initial position estimation during startup, and the initial sector is identified. Subsequently to the initial step, the rotor position can be estimated and used as the initial condition for the low-speed sensorless control. Since the method is implemented in a four-phase machine, each phase is responsible for 90° electrical degrees. After the first step, the machine can run using the low-speed sensorless control, where pulses are injected into the idle phases, and the inductance information is estimated and used in the sensorless control. At high speeds, the estimation method is the same, but there is no need for pulse injection due to an increase in back-EMF and reduction of the integration period of the flux linkage. The performance of the proposed method is evaluated under different speeds, load conditions, and transients.

5.1 Proposed Nonlinear Optimization-Based Estimator

Figure 5.1 shows a simplified block diagram of the proposed unified nonlinear optimization-based sensorless control method. First, the rotor position under standstill operation

can be estimated using a pulse injected into all phases, where the sector estimation method using the current magnitude comparison can be implemented as presented in section 4.3.1. Using the initial sector identification, a high-frequency square-wave voltage pulse is injected into the sensing phase, and the optimization-based sensorless control is used for the rotor position estimation during standstill and low-speed. When the rotor speed increases, the signal-to-noise ratio is improved due to the increase of the back-EMF, the phase inductance becomes observable under fundamental excitation region, and the pulse injection can be disabled when the rotor speed reaches a certain threshold. The same optimization-based method can be used, which provides a single estimation technique over a wide speed range, avoiding transition problems between distinct estimation methods.

For the proposed method, the position estimator is based on the voltage equation of the machine (5.1)

$$\begin{aligned} V_{ph} &= Ri + L(\theta, i)\frac{di}{dt} + \frac{dL(\theta, i)}{dt}i \\ V_{ph} &= Ri + L(\theta, i)\frac{di}{dt} + \frac{\partial L(\theta, i)}{\partial \theta}i\omega_e + i\frac{\partial L(\theta, i)}{\partial i}\frac{di}{dt} \end{aligned} \tag{5.1}$$

The equation is then converted to a discrete representation for digital implementation. If the motor parameters, the phase terminal voltage, and the phase current is known, it is possible to solve the nonlinear equation for the estimated position $\hat{\theta}(k)$,

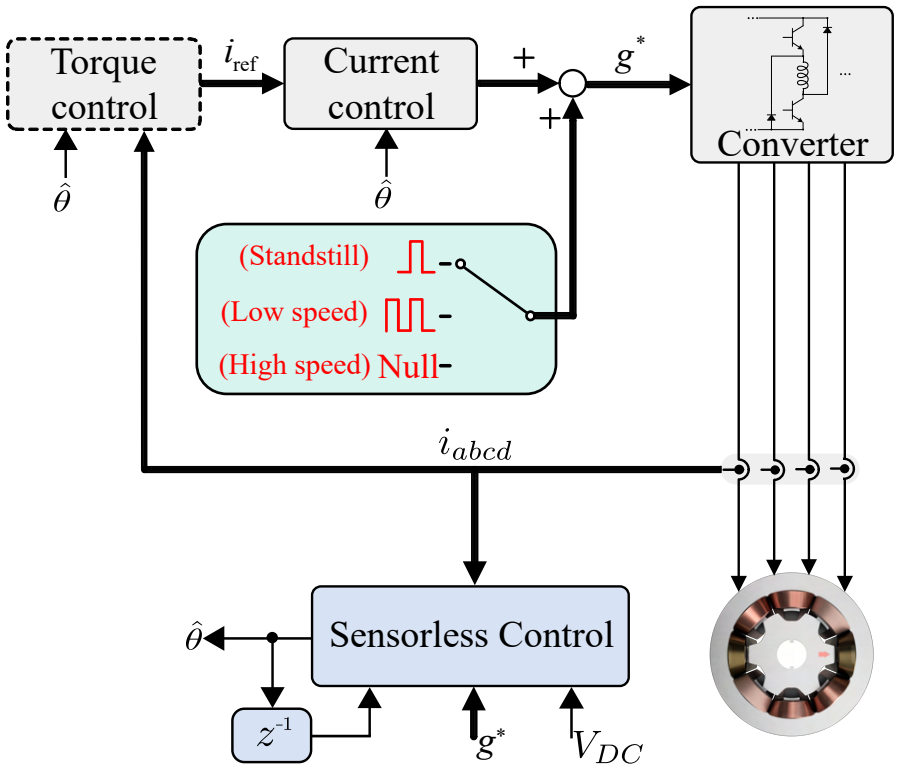

Figure 5.1: Control diagram of the proposed unified nonlinear optimization-based sensorless control for a wide speed estimation

as shown in (5.2) and (5.3)

$$\begin{aligned} V_{ph}(k) =& Ri(k) + L(\widehat{\theta}(k), i(k))\frac{i(k) - i(k-1)}{T_s} \\ &+ i(k)\left(\frac{L_{calc}(\theta(k), i(k)) - L(\widehat{\theta}(k), i(k))}{T_s}\right) \end{aligned} \tag{5.2}$$

$$L_{calc}(\theta(k), i(k)) = \begin{cases} V_{ph}(k)\left(\frac{T_s}{i(k)-i(k-1)}\right) & \text{, LS pulse injection} \\ \left(\frac{(\lambda_{ph}(k-1)+(V_{ph}(k)-Ri(k))T_s)}{i(k)}\right)\Big|_{i>0} & \text{, HS (no injection)} \end{cases} \tag{5.3}$$

where $i(k)$ and $i(k-1)$ are the phase current at time step k and $k-1$, respectively, $L(\hat{\theta}(k), i(k))$ is the estimated inductance at time step k, T_s is the sample time, $\lambda_{ph}(k-1)$ is the flux-linkage calculated at time step $k-1$, LS is the low-speed estimation region and HS is the high-speed estimation region.

When considering the phase inductance modeling benchmark presented in section 3.4, the proposed least-square-based method (LSA) showed good performance when compared to the linear and the truncated Fourier expansion methods. Another advantage of the LSA is the reduced complexity when implementing on digital signal processors (DSPs). Polynomial-based models can present a better performance since reduced computational cycles are required, and techniques like Horner's rule can be implemented to optimize the algorithm execution time on multiply and accumulate (MAC) architectures.

In this work, to further reduce the computational burden of the proposed method, a truncated 5^{th} order least-square-based polynomial expansion is used for the inductance profile approximation, providing a good trade-off between computational demand and accuracy, as presented in Chapter 3. It should be noted that the inductance is a non-linear function of rotor position and current, and the inductance changes related to the current variation also need to be approximated. For the numerical modeling methods shown in Chapter 3 and proposed in the literature, the current coefficients are approximated by a polynomial equation. To simplify the model, current-varying inductance information is also approximated by a 5^{th} order polynomial.

Since SRMs are symmetric on the positive and negative slope of phase inductance, only the first half-cycle (0° to 180° electrical or unaligned to aligned position) needs to

be approximated, as presented in Figure 5.2. The red dots represent the experimental inductance data, and the surface represents the approximated fitted curve using a 5^{th} order polynomial.

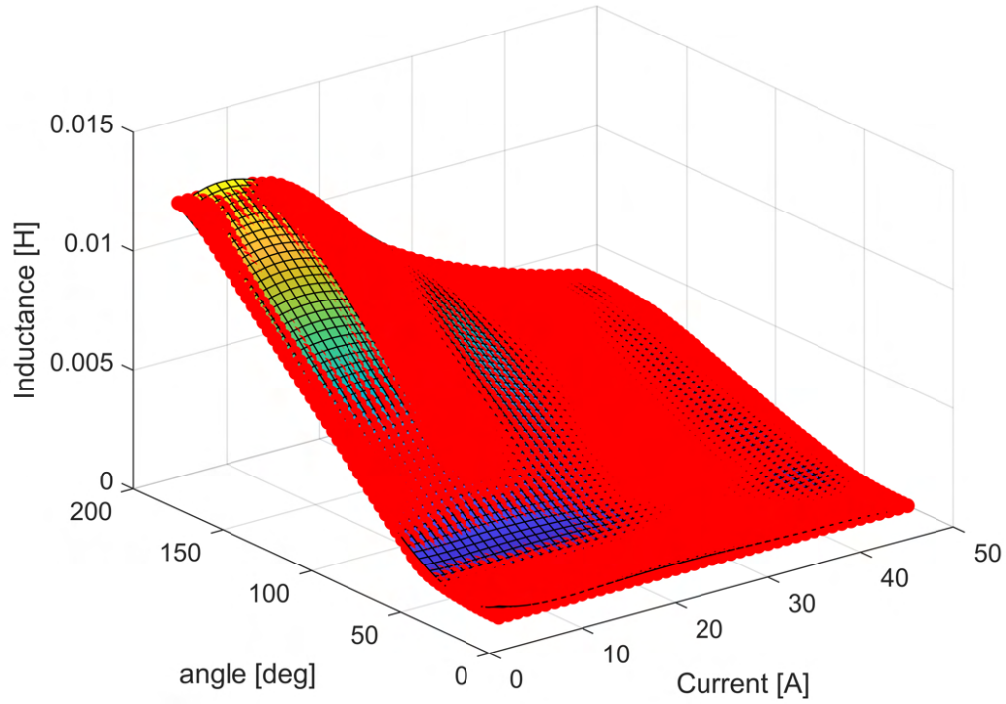

Figure 5.2: 5^{th} order least-square-based polynomial expansion, where the surface is the polynomial approximation, and the red dots are the experimental data

With the inductance analytical model and the machine voltage equation, the rotor position can be extracted by solving the nonlinear equation in (5.3). (5.3) can then be converted to a cost function format, as presented in (5.4), where the estimated position is equal to the actual position at the local minimum. Using a convex optimization algorithm, the error from the actual rotor position and the estimated rotor position

can be minimized by searching for the minimum of the cost function.

$$min_{\theta(k)} G(\hat{\theta}(k)) = \left\| V_{ph}(k) - Ri(k) - L(\widehat{\theta}(k), i(k)) \frac{i(k) - i(k-1)}{T_s} - i(k) \left(\frac{L_{calc}(\theta(k), i(k)) - L(\widehat{\theta}(k), i(k))}{T_s} \right) \right\|^2 \tag{5.4}$$

Similar approaches of convex-optimization-based sensorless control were used in PMSMs by [81–84]. Switched reluctance machines present additional challenges since the inductance profile varies with current and rotor position, and uses a discontinuous phase excitation control for the machine control algorithm. The position estimation needs to be implemented in a logical algorithm using the discontinuous current information, switching between phases for complete electrical cycle information. When considering the four-phase 8/6 SRM used in this work, each phase can contribute with 90° electrical degrees, making it possible to continuously estimate the complete 360° of the electrical period.

Another important consideration for the SRM is the non-observability during the aligned and unaligned rotor positions, since there is not a unique solution in these regions as presented in Figure 5.3. When operating under different current amplitudes and rotor position close to the unaligned (region A) and aligned position (region B), the rate of change of inductance regarding the rotor position is very low, and the position cannot be estimated in this region.

For the unaligned region, the solution presents a singular inductance amplitude for different current amplitudes and rotor position variation, which does not contain a singular rotor position information when solving the non-linear problem. This

shortcoming is noticed in every position sensorless control for SRMs, and is not an isolated problem to the convex optimization-based method. To overcome this issue, the phases used to estimate the position are selected concerning the observable region (40° to 160° or 200° to 320°). Figure 5.4 shows the contour plots of the cost function for different rotor conditions, when considering the rotor position ranging from 40° to 160° using 20° steps. From the contour plots, it can be observed that the cost function decreases as the estimated position approach the actual position. However, as mentioned previously, the function is not observable close to aligned and unaligned position, and the convexity reduces at rotor positions closer to these operating points.

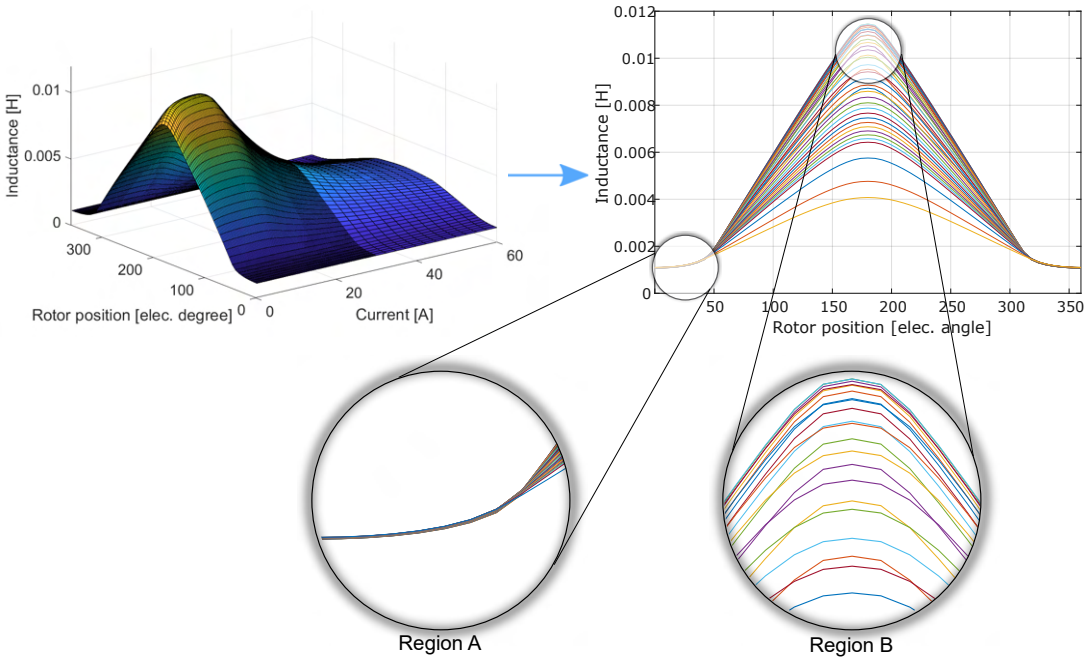

Figure 5.3: Observable regions. Region A shows the unaligned position and Region B shows the aligned position

The cost function has three local minimums in the positive and negative torque region. The first local minimum is at close to unaligned position, the second local

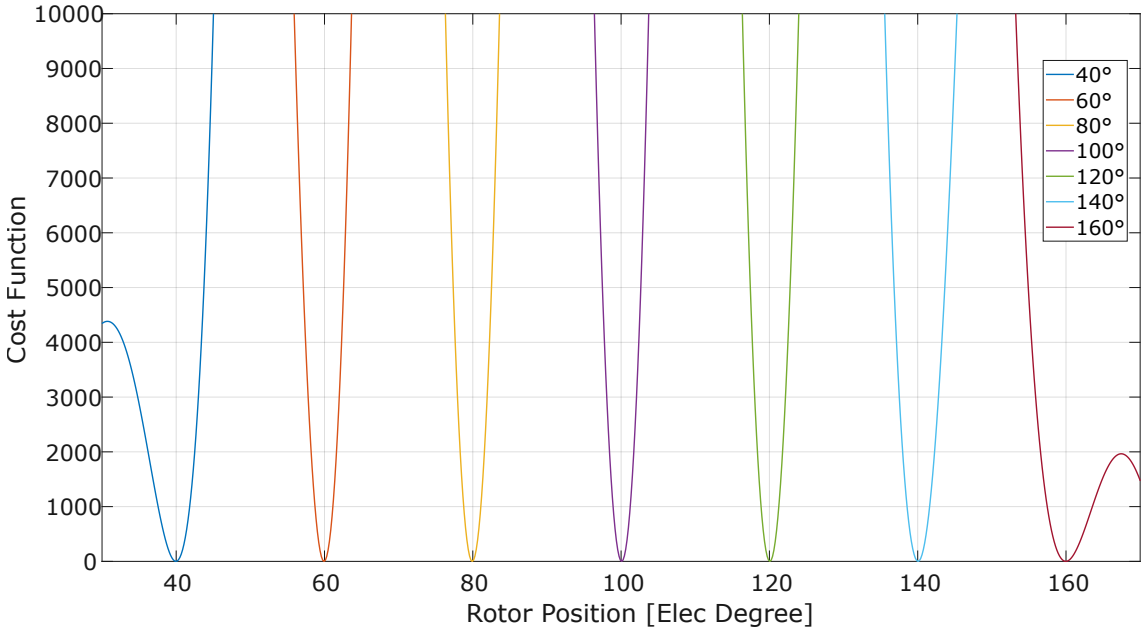

Figure 5.4: Countour plot for different rotor position

minimum is at the correct rotor position, and the third local minimum is at close to aligned position, as shown in Figure 5.5. Therefore, the position estimation becomes an online nonlinear optimization problem that can be solved by minimizing the cost function. The cost function minimization is only possible if, and only if, the function is locally convex and if the estimation is around the expected local minimum after a finite number of iterations. A cost function is convex if the second derivative is positive semi-definite in the convex region. The convergence of the proposed method is guaranteed if the position errors are within the observable regions. Outside these regions, convergence cannot be guaranteed.

Newton's method can present a fast convergence rate, but it does not guarantee convergence to a local minimum. As observed in Figure 5.5, local maximums can happen in the observable region if the initial value is not close enough to the actual

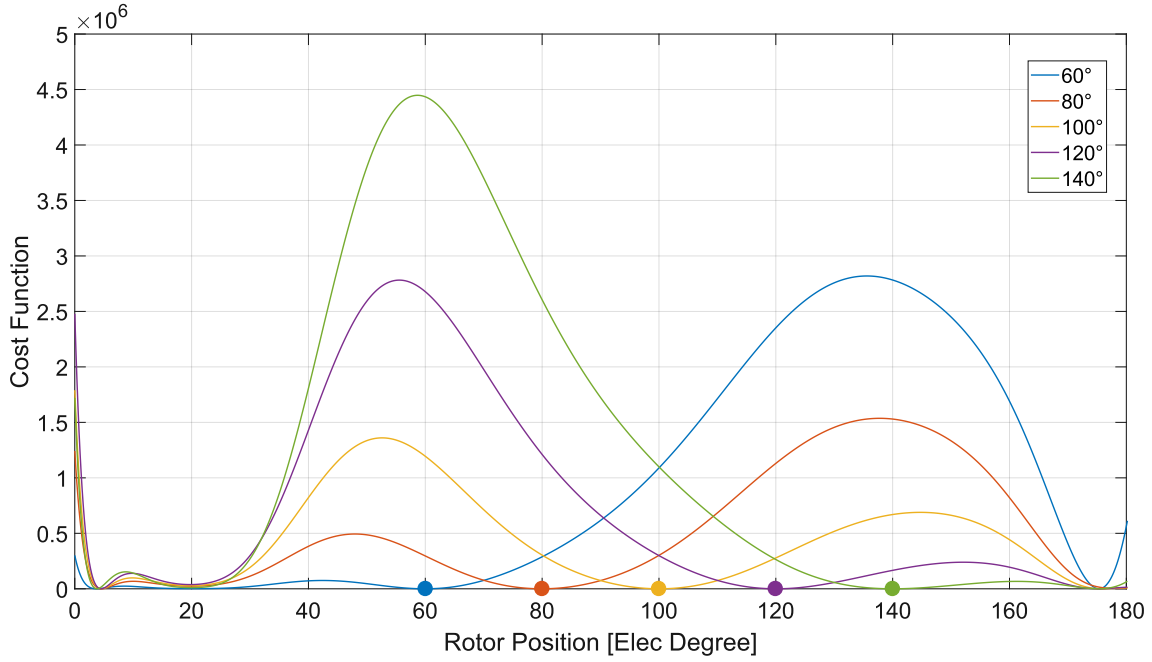

Figure 5.5: Convex region for rotor position from 60° to 140°

value. To address this problem, the Levenberg-Marquardt method can be implemented, which presents a combination of Newton's method for optimization and the steepest descent method, as shown in (5.5). When ξ is small enough, the second derivative dominates, and the step becomes a Newton's step. When ξ is large, the gradient dominates, and the step is approximated in the steepest descent direction. The Levenberg–Marquardt method starts each iteration with a small value of ξ, thus increasing the weight of Newton's step. If the objective function is reduced, the new point is accepted, and ξ is reduced. Otherwise, the value of ξ is increased until a reduction in the objective function is obtained.

$$\hat{\theta}(k) = \hat{\theta}(k-1) - \left(\frac{\partial G(\hat{\theta}(k-1))}{\partial \hat{\theta}(k-1)}\right)\left(\frac{\partial^2 G(\hat{\theta}(k-1))}{\partial \hat{\theta}^2(k-1)} + \xi\right)^{-1} \tag{5.5}$$

5.2 Wide Speed Range Operation Analysis

The voltage equation is used for the position estimation by minimizing the proposed cost function based on phase currents and voltage measurements. Since the induced voltage is low or null at low speeds, an additional signal must be injected to enable the rotor position estimation in this operating region. An additional regularization term is added to the cost function to act as a penalty condition, where position estimation errors and oscillations around the estimated value can be reduced by the low-pass filter characteristics of this term. The rotor speed can be estimated using a simple moving average filter or a Phase-Locked-Loop (PLL). At high speeds, the high-frequency injection signal is not required. The position estimation uses a single algorithm under a wide operating region without switching between different methods.

5.2.1 Sensorless Control Implementation

For the position observer implementation, the cost function is modified, and a regularization term K is added, penalizing the function if there is a high rate of change in rotor position, creating a low-pass filter characteristic, and reducing the estimation oscillation. The full cost-function for a wide speed range is show in (5.6), where the $(k|k)$ is the calculation at time step k using the information from k, and $(k|k-1)$ is the calculation at time step k using the initial condition from $k-1$. The initial rotor position condition can also be compensated, if needed, using the information of the rotor speed, so the convergence rate can be improved when the initial value is close

to the real value (5.7).

$$min_{\theta(k|k)} G(\hat{\theta}(k)) = \Bigg\| V_{ph}(k) - Ri(k) - L(\widehat{\theta}(k|k-1), i(k)) \frac{i(k) - i(k-1)}{T_s} - i(k) \left(\frac{L_{calc}(\theta(k), i(k)) - L(\widehat{\theta}(k|k-1), i(k))}{T_s} \right) \Bigg\|^2 + K(\hat{\theta}(k|k) - \hat{\theta}(k|k-1))^2 \tag{5.6}$$

$$\hat{\theta}(k|k-1) = \hat{\theta}(k-1) + \omega_{mech} \frac{N_r * 360}{60} Ts \tag{5.7}$$

where $\hat{\theta}(k|k-1)$ is the initial condition for the optimization algorithm and ω_{mech} is the mechanical speed of the machine in rpm.

5.2.1.1 Standstill/Start Operation

For the initial rotor position identification during startup, a voltage pulse is injected into all phases, and the position sector can be identified as presented in Section 4.3.1.1. Figure 5.6 shows a simplified current profile of the four-phase SRM, where each sector represents a 45° region. Table 4.1 can be used to estimate the initial condition for the optimization-based method. By convention, the 0° electrical is considered to be at the unaligned position, as presented in Figure 4.14. The phase selection is made by using the region with the highest convexity, which is demonstrated to be in the quasi-linear region (position variation) of 90° to 135°, or 270° to 315° as shown in Figure 5.3. Since the inductance profile is symmetric for the positive and negative torque regions, the cost function and inductance characterization do not need to be modified for the negative slope of the inductance, where a simple angle correction of 180° can be implemented. To reduce the convergence time, the initial rotor condition

can be approximated to the center value of the sector at 112.5°.

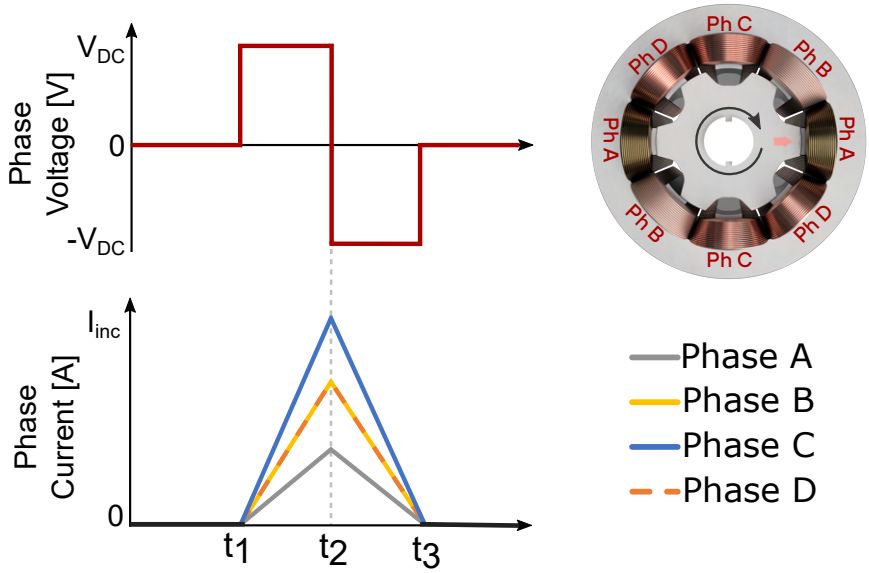

Figure 5.6: Simplified current profile for a multi-phase pulse injection during initial position estimation

This step only needs to be performed during the machine's startup, and the wide speed range sensorless control algorithm can be used during the operation condition. Since the injection period is short, there is a negligible torque generated by this method, and there is no rotor movement during this process, which presents an essential requirement for some applications. The same optimization-based technique is used for the standstill operation even when using a different injection method.

5.2.1.2 Low-Speed Operation

The SRM sensorless control relies on acquiring the inductance or flux-linkage, which has the rotor position information. The back-EMF is low or negligible at low speeds, and flux-linkage calculation can have high deviations due to the resistance error integration, measurement noise, and inverter non-linearities, making the sensorless control

unfeasible. Implementing a pulse injection algorithm on the idle phases can solve this problem, as presented in Section 4.3.1.

The ohmic voltage drop and back-EMF terms are not considered when assuming a high injection amplitude frequency, and the current-derivative and injection voltage information is used for the incremental inductance calculation ($L_{calc}(k) = V_{ph}(k) - \Delta t/\Delta i$).

After the initial step of position estimation during startup, the motor can effectively run using the proposed optimization-based low-speed sensorless control algorithm, which is implemented using the high-frequency voltage signal injection into the idle phases. The phase inductance, as presented in [57, 85], can be calculated as shown in (5.8), and the inductance information is used for the low-speed position estimation. The pulse injection profile is shown in Figure 5.7, where in this work, a pulse with voltage amplitude V_{DC} is applied at time step k, a $-V_{DC}$ pulse is applied at time step $(k+1)$, and to guarantee that the current is reduced to zero before the next pulse, a $0V$ voltage is applied to the idle phase at time step $(k+2)$.

$$L(\theta(k), i(k)) = \begin{cases} \dfrac{V_{Inj}}{di/dt|_P} & \text{, Turn-ON slope} \\ \dfrac{2V_{Inj}}{di/dt|_P - di/dt|_N} & \text{, Turn-OFF slope} \end{cases} \tag{5.8}$$

If the terminal currents, voltages, and motor parameters are known, the rotor position can be estimated by searching the minimum of the nonlinear equations in (5.6). The pulse injection is sequentially applied to the idle phases, where for the four-phase machine, each phase is responsible for 90° of the electrical period. The general overview of the low-speed position estimation algorithm is presented in Figure 5.8.

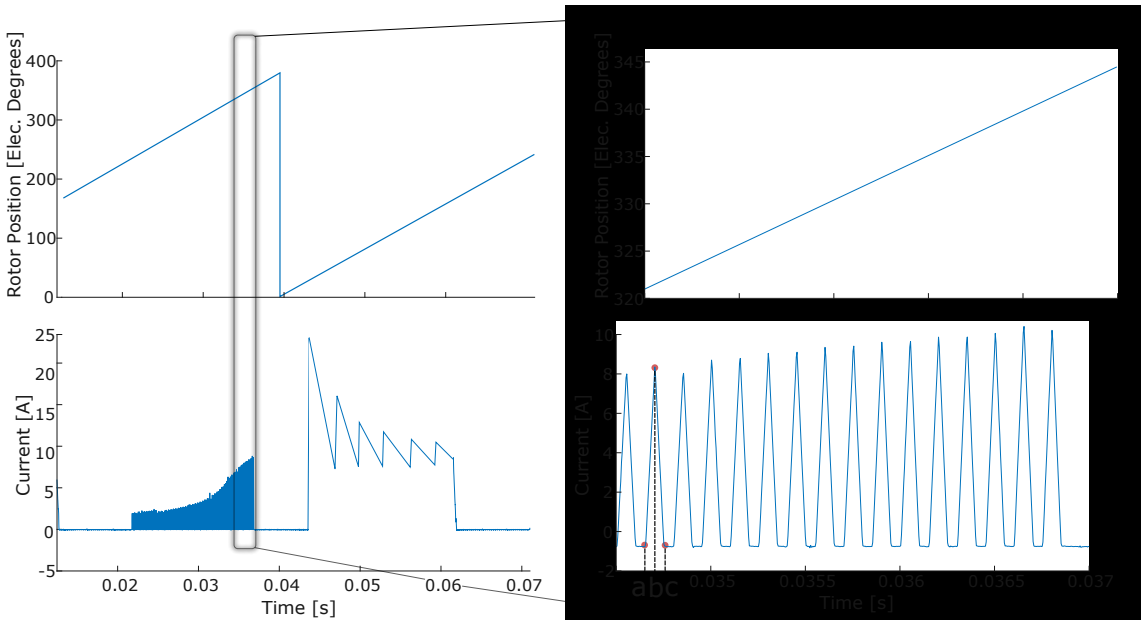

Figure 5.7: Current waveform during pulse injection, where a is at time step k, b is at time step $(k+1)$, and b is at time step $(k+2)$

5.2.1.3 High-Speed Operation

At high speeds, the time derivative of rotor position increases, reducing the number of data samples, which leads to an inaccurate rotor position estimation when using most of the pulse-injection methods. In addition to reduced accuracy at high speeds, the pulse injection on idle phases produces a negative torque, additional torque ripple, and acoustic noise, which can reduce efficiency, making this solution unattractive for a wide-speed operation. For these main reasons, the control algorithm needs to be optimized to reduce the operation band of the pulse-injection-based methods, while still maintaining a stable and reliable operation.

For the high-speed sensorless control, the SNR is increased due to an increase in the back-EMF. The electrical quantities of phase inductance become observable under

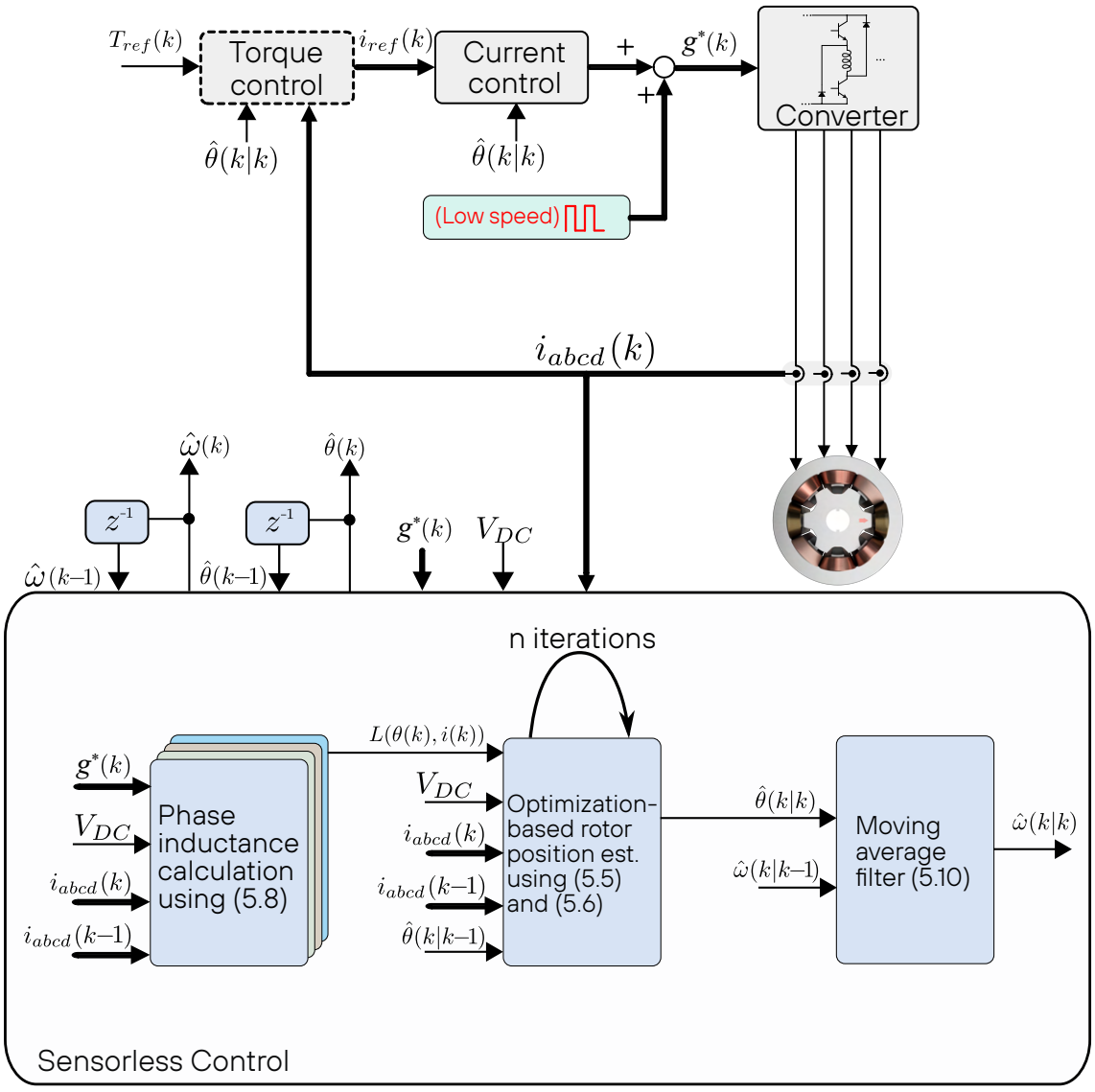

Figure 5.8: Block diagram of the low speed sensorless control implementation

fundamental excitation conditions, without the need for an additional pulse injection signal on idle phases. When considering sensorless control for traction application, the dynamics and stability of the system are extremely important. High accuracy and robustness under fast transient response must be guaranteed over the entire operating region.

A transition from the low to high speeds, or vice-versa, is implemented using a hysteresis band with lower and upper limits, as shown in Figure 5.9. The hysteresis band improves the system stability since there are no constant changes from one method to another at the boundaries. In this work, the limits are empirically selected around 10% of the rated speed, which was validated to provide a good estimation accuracy using both schemes, with the hysteresis boundaries of $\omega_{\text{low}} = 600\text{rpm}$, and $\omega_{\text{high}} = 800\text{rpm}$. A 200 rpm band avoids constant changes during the transition period.

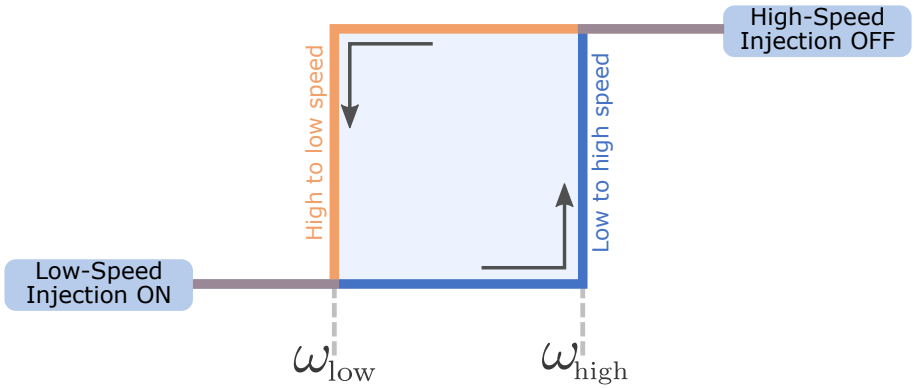

Figure 5.9: Sensorless control transition method from different operating conditions

During the high-speed estimation method, the phase inductance is observable and can be calculated by (5.9). The rotor position estimation is implemented using the Levenberg-Marquardt method, numerically minimizing the cost function presented in (5.7), where the phase current and voltage is employed for estimation at the sampling frequency, and the previous sampling time position information, $\hat{\theta}(k|k-1)$, is used as the initial condition for the optimization. The regularization term K is linearly reduced as the speed increases, compensating for the increase in the position error

caused by the discretization period of $\hat{\theta}(k)$ and $\hat{\theta}(k-1)$.

$$L_{calc}(k) = L_{calc}(k-1) + \left.\frac{\Big(V_{ph}(k) - Ri(k)\Big)T_s}{i(k)}\right|_{i(k)>0} \tag{5.9}$$

5.3 Experimental Validation

For the experimental setup, the 8/6 SRM and the IM dyno described in Section 3.2.1 are used. The control board is based on a 32-bits 150Mhz Texas Instrument DSP (TMS320F28335). The motor control was implemented using a torque/current loop, and the IM machine, used as a load, was controlled in speed mode. A 220V DC-link was used on the test bench, where the two machines shared the same DC-bus in a back-to-back configuration.

In all cases, the control/sampling frequency was set to 20 kHz, and the switching frequency was variable depending on the hysteresis control, with a maximum switching frequency of 10kHz. The turn-on and turn-off angles for the current hysteresis control were constant at 20° and 160°, respectively, to simplify the comparison between the implemented methods. To verify the accuracy of the estimated position, the actual rotor position was measured using a resolver installed on the SRM shaft and discretized using a 12bit Analog-Digital-Converter (ADC), but was only used to calculate the estimation errors. The actual and estimated position estimation was then presented using a Digital-Analog-Converter (DAC), and the data was recorded using a Tektronix® MDO4024C oscilloscope.

For the low-speed estimation, the injection frequency was selected as 33% (6.667kHz)

of the control frequency (20kHz), with an injection waveform presented in Figure 5.7. Since the speed bandwidth is lower than the rotor position, the speed ($\omega(k)$) was estimated using a simple moving average filter (MAF) using the rotor position variation as presented in (5.10), where $\omega_{accu}(k)$ is the cumulative value at time step k of n speed samples. The microcontroller implementation of this method uses a cumulative data storage and bit shift operation to reduce the memory allocation and system complexity, while still providing acceptable results under steady-state and transient response. The MAF implemented in this work used 64 samples ($n = 64$).

$$\begin{cases} \omega_{accu}(k) = \left(\omega_{accu}(k-1) - \dfrac{\omega_{accu}(k-1)}{n}\right) + \dfrac{(\hat{\theta}(k) - \hat{\theta}(k-1))}{T_s} \\ \omega(k) = \dfrac{\omega_{accu}(k)}{n} \end{cases} \tag{5.10}$$

For the parameters selection of the proposed method, the parameter K of the cost-function, which is used as a regularization term and presents a low-pass filter characteristic, was selected to linearly vary from 1000 to 100, for motor speeds of 0 rpm to 4000 rpm, respectively, providing a good rotor position estimation and dynamic response.

5.3.1 Initial Consideration and Setup Limitations

When considering the system implementation, current sensor measurement noises, rotor eccentricity, DC-link voltage oscillation, and other parameters can highly affect the estimated position. Since the estimation is based on instantaneous values of current and inductance/flux-linkage, the noises can be filtered by a Phase-Locked-loop (PLL), which is commonly implemented in conventional sensorless control techniques,

reducing the estimation oscillation and error. To provide a stable operation, the PLL gains need to be adjusted for a specific operating condition of the motor, reducing the position error during the steady-state operation or reducing the errors under transients, but usually not both. In traction application, load conditions and torque requests can abruptly change during the motor/generation operation, while stable operation must be guaranteed in all scenarios. Variable gain PLLs can be implemented to mitigate the mentioned problems, but they can drastically increase system complexity, commissioning time and validation time. The observer structure using a PLL in series is presented in Figure 5.10. To avoid the use of a PLL and to reduce the system complexity while still providing high transient performance, the regularization term K of the proposed methods is used as a low-pass filter, where it can be dynamically adjusted for a wide speed range, working as a penalization term for the cost function at high-frequency position oscillations.

Rotor eccentricity can cause changes in the air gap depending on the rotor mechanical position, which then causes a variation in the flux-linkage/Inductance profile. The machine was tested under low DC link voltage on a single pulse operation to verify the rotor eccentricity. Since the DC-link voltage is low (20 V for this test), the machine achieves the single-pulse operation at low speeds, providing a better position discretization and more accurate control. As can be observed in Figure 5.11, the current amplitude varies during one mechanical cycle, which indicates a change in the inductance amplitude, showing later as harmonic contents on the position estimation. This issue is challenging to be mitigated since a compensation algorithm is hard to be implemented due to the unavailability of an absolute mechanical position, but the deviation does not present a considerable error generation on position

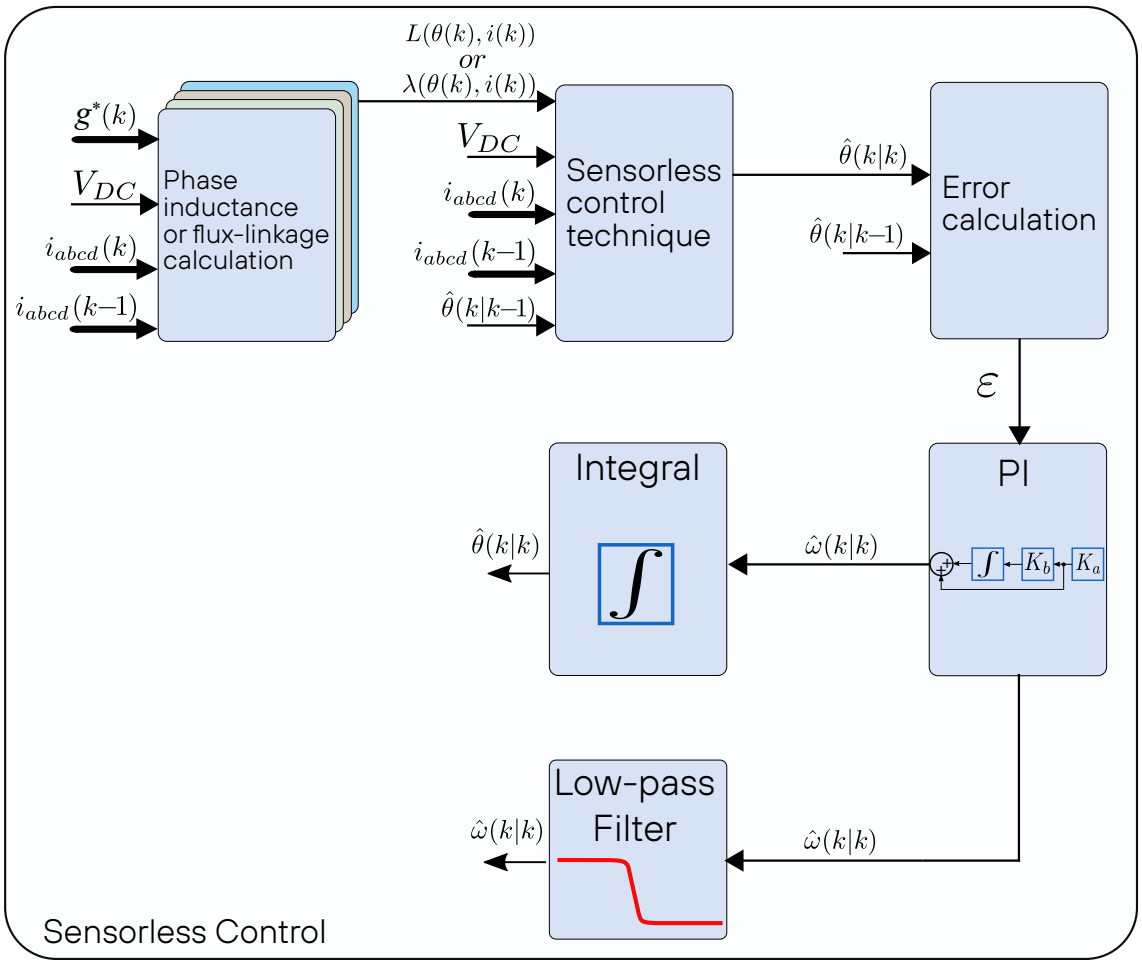

Figure 5.10: Generic PLL diagram

estimation. The same phenomenon is observed on the inductance estimation at the high-frequency injection region, where amplitude variation is more evident closer to the aligned position and under low core saturation, and less noticeable when closer to unaligned position and high core saturation, as expected due to the inductance profile of the SRM shown in Figure 5.3.

Another limitation of the setup is that the induction machine used as a dynamometer has a maximum mechanical operating speed of 3600 rpm, limiting the maximum

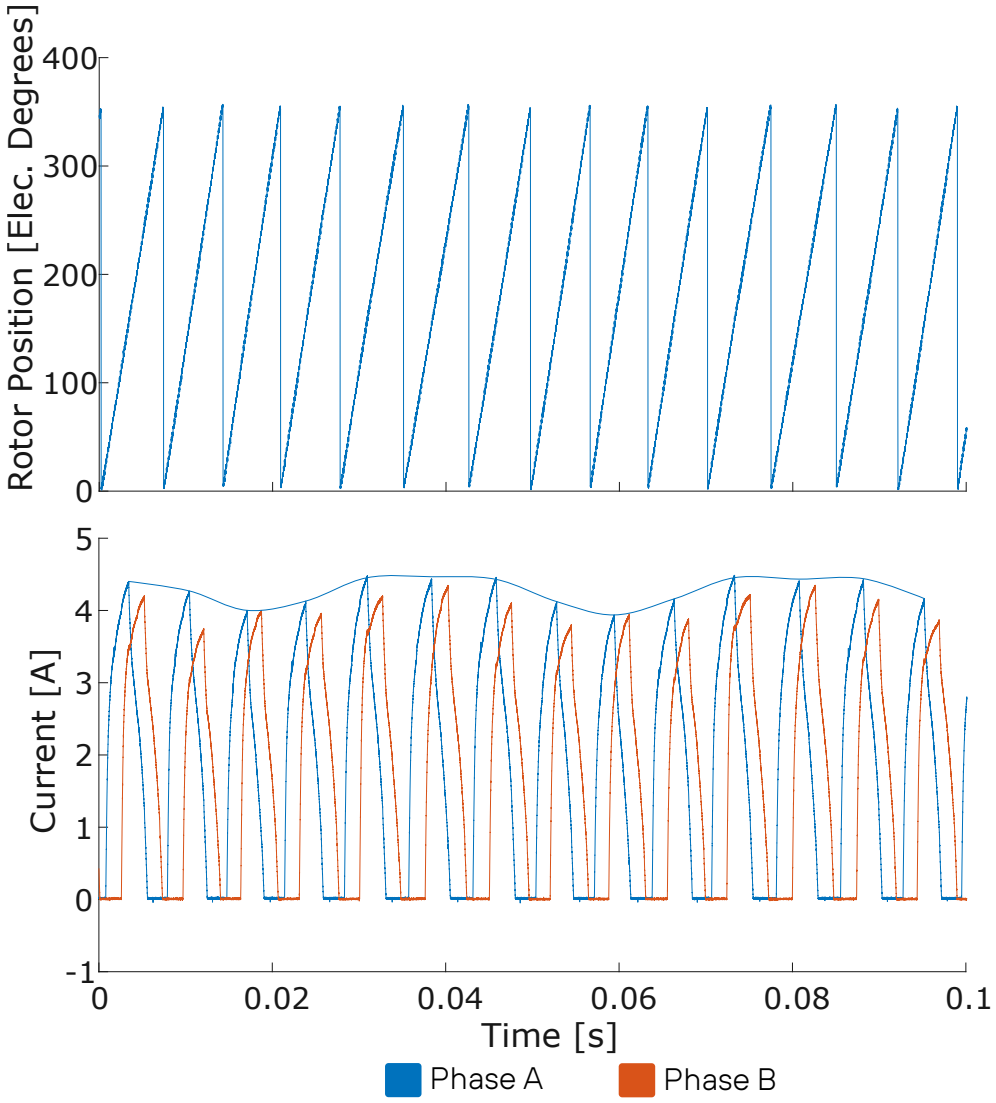

Figure 5.11: Induced current under low DC-link voltage - single pulse operation

capable speed of the SRM. Due to the inherent torque ripple of switched reluctance machines, the speed loop control of the IM cannot provide a fast response to the torque variations, presenting high-speed oscillations. When operating close to the rated speed, the dyno can reach the protection limits, causing the SRM to shortly operate under no-load conditions until the SRM motor drive protection is triggered,

turning off the system. Due to these limitations, the tests were limited to 3000 rpm.

5.3.2 Low-Speed Estimation Performance

After the startup stage presented in 5.2.1.1, the initial rotor position is identified. The unified non-linear optimization-based (UNLO) sensorless control is then started by injecting the high-frequency pulses into the idle phases, and using the initial condition from the startup process.

For the real-time implementation, the Levenberg-Marquardt method is applied for minimizing the cost function presented in (5.6). The DC link voltage amplitude and the measured currents of the injected signal are used for the phase inductance estimation. First of all, the estimated position from the previous sample time is used as the initial condition for the optimization; then, the search direction is calculated by the first and second derivatives of the cost function. After a finite number of iterations, if the initial condition is defined in a convex region, the estimated rotor position $\hat{\theta}(k|k)$ should converge to the actual rotor position $\theta(k|k)$. The new estimated value is then used as the initial condition for the subsequent estimation.

The inductance can be estimated using the information of the phase voltage and phase current, as presented in (5.8). As previously mentioned, the inductance waveform presents amplitude variations due to the rotor eccentricity and spikes due to current measurement noise. Figure 5.12 shows the inductance waveform under no-load condition using only the pulse injection for estimation. The inductance estimated from the pulse injection in (5.8) is compared to the phase inductance estimated using a pre-stored lookup table and actual rotor position (resolver information), $L(\theta(k), i(k))$. It can be observed that the estimated inductance presents good convergence with the

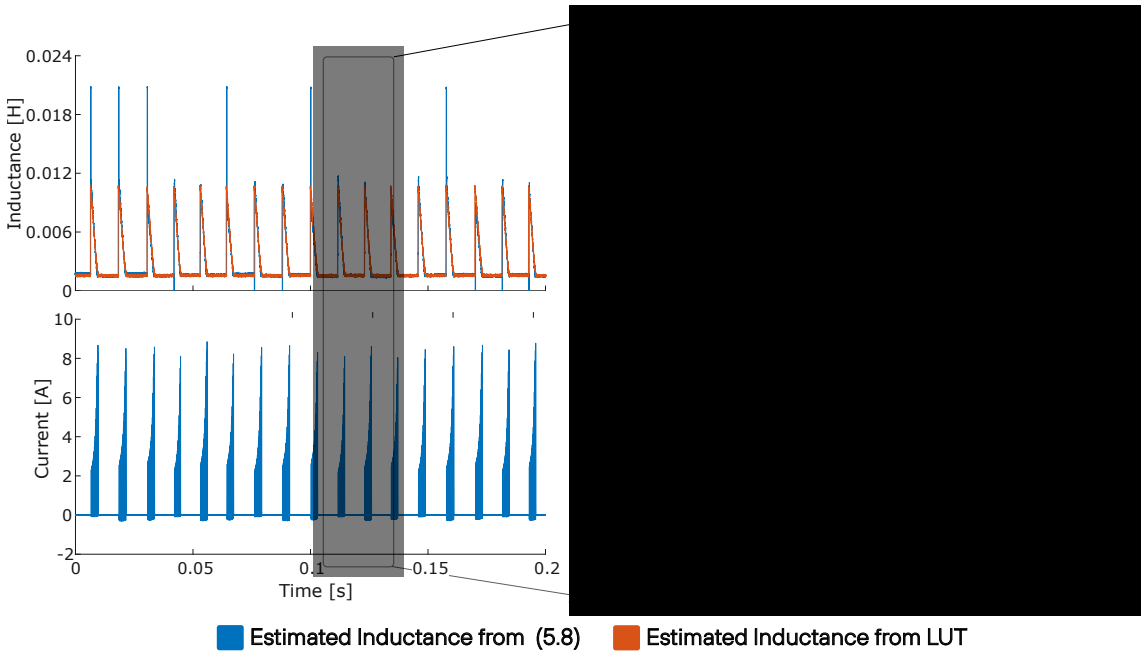

Figure 5.12: Inductance profile comparison at 300 rpm under no load condition, and using the band from 230° to 340°

pre-store inductance information.

Figure 5.13 shows the SRM operating at 200 rpm under low-load condition (20%). The induced current generated by the voltage pulses injected into the idle phases is used for the phase inductance calculation, while these values are set to zero when there is no injection. Since only 90° are required per phase for a complete electrical period, the pulses were injected from 230° to 340°, which gives a ±10° band, reducing additional losses and acoustic noise generation.

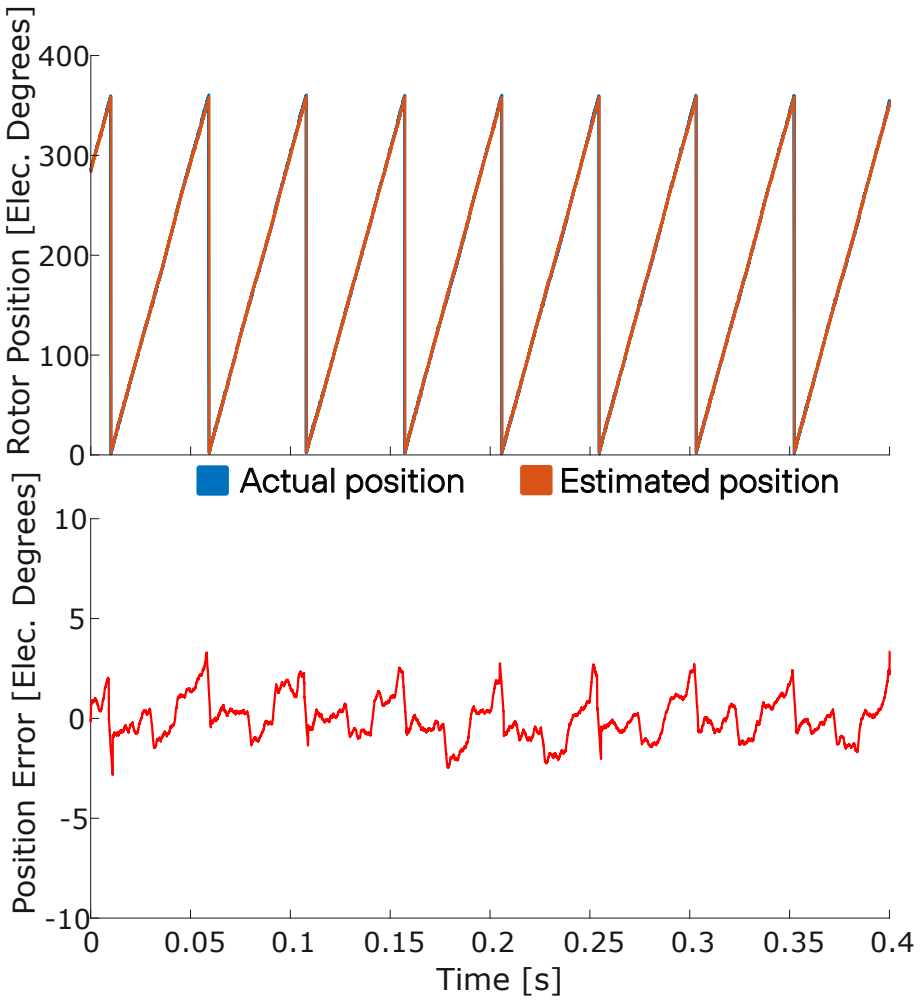

Figure 5.13: Low speed sensorless control at 200 rpm under low-load condition

The estimated and actual position at 500 rpm is presented in Figure 5.14. Similar to the results of 200 rpm, the proposed method can accurately estimate the rotor position. By convention, all errors and rotor position are represented in electrical degrees, which has an order of magnitude six times higher for the 8/6 SRM. For the proposed low-speed method, the load condition has no effect on the position estimation errors, since only the idle phases are used for the sensorless control.

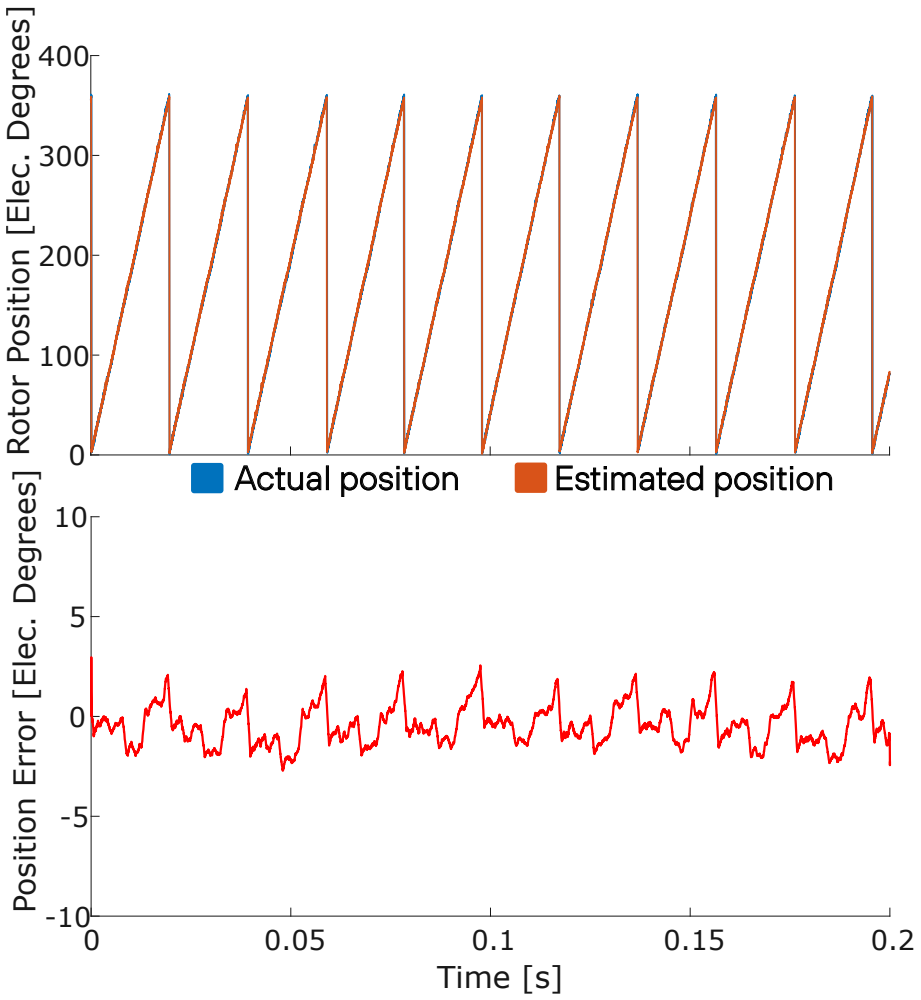

Figure 5.14: Low speed sensorless control at 500 rpm under low-load condition

As previously mentioned, the regularization term K linearly changes with the rotor position and acts as a low-pass filter for the position estimation. Figure 5.15 presents a comparison using the regularization term and a PLL strategy, showing that the error amplitude is similar, with the advantage of the proposed method using the regularization term to reduce the complexity and improve the dynamic response.

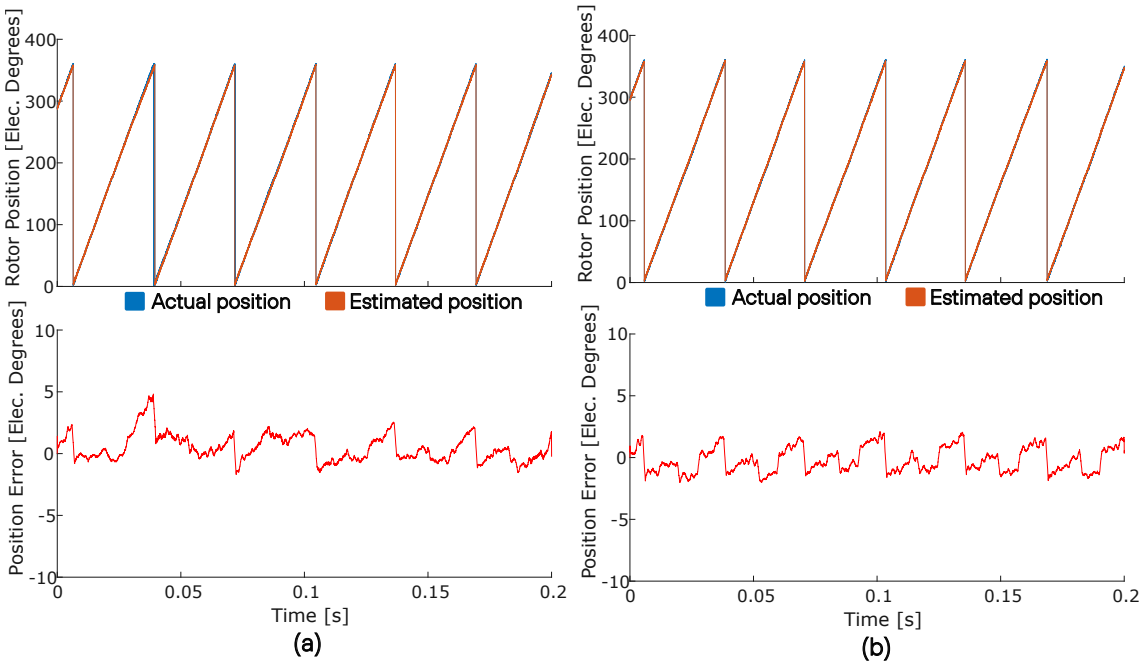

Figure 5.15: Low speed sensorless control at 500 rpm under low-load condition. a) using a PLL-based algorithm and b) using the regularization term K

5.3.3 High-Speed Estimation Performance

The pulse injection is not needed for the high-speed sensorless control, and the phase inductance can be calculated using the information from the energized phases. The initial condition for the optimization comes from the previous low-speed step. Figure 5.16 presents the steady-state performance of the UNLO sensorless control at 3000 rpm under different load conditions. The proposed sensorless control shows good convergence to the measured position, with an error within $\pm 5^{\circ}$ electrical degrees, while still presenting good stability under different load conditions.

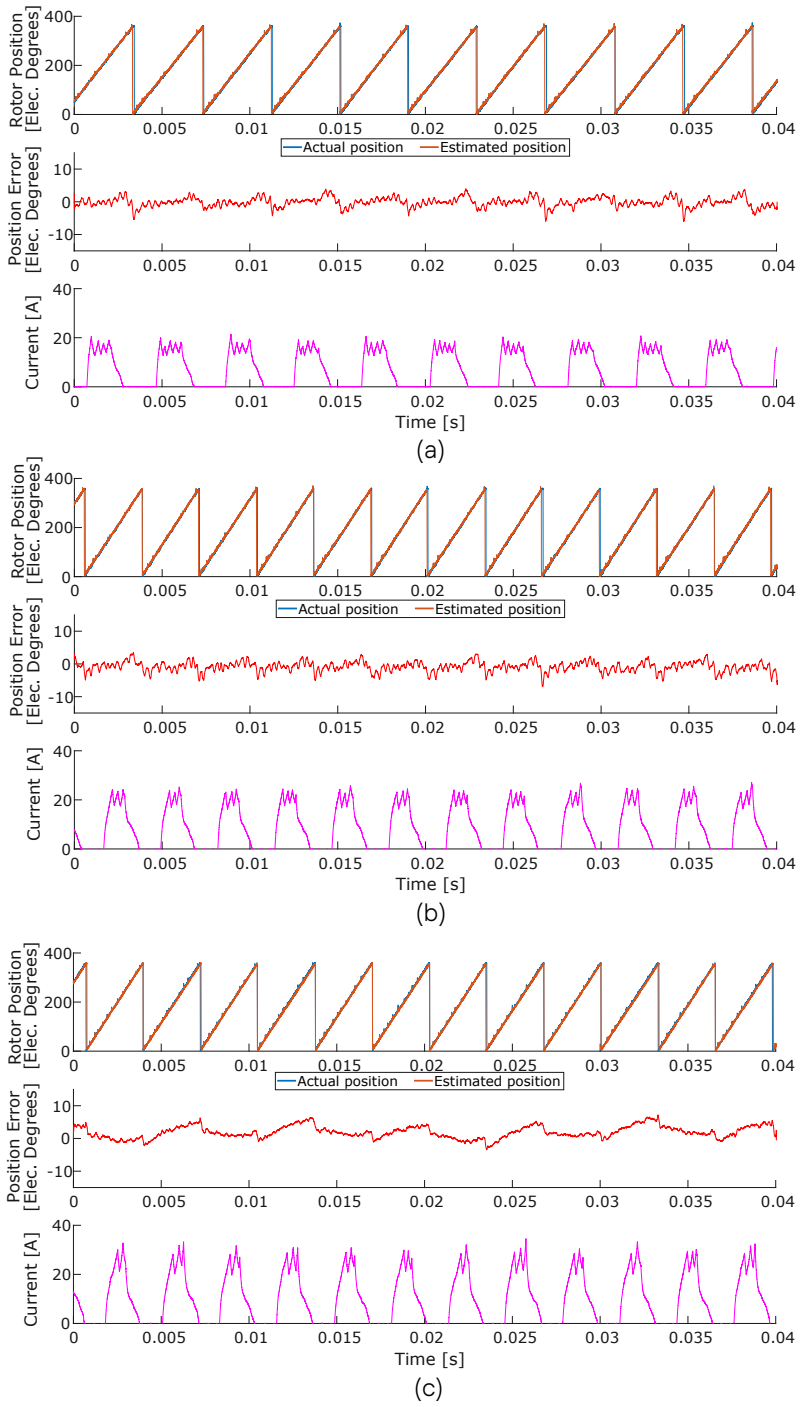

Figure 5.16: High speed sensorless control at 3000 rpm under different load conditions. a) 30% load, b) 70% load, and c) 100% load

Under high currents, the rotor eccentricity is less noticeable due to high core saturation, presenting a smaller amplitude variation when compared to low-load cases, as shown by the flux-linkage calculation at 2500 rpm in Figure 5.17, which improves the performance of the proposed and conventional methods.

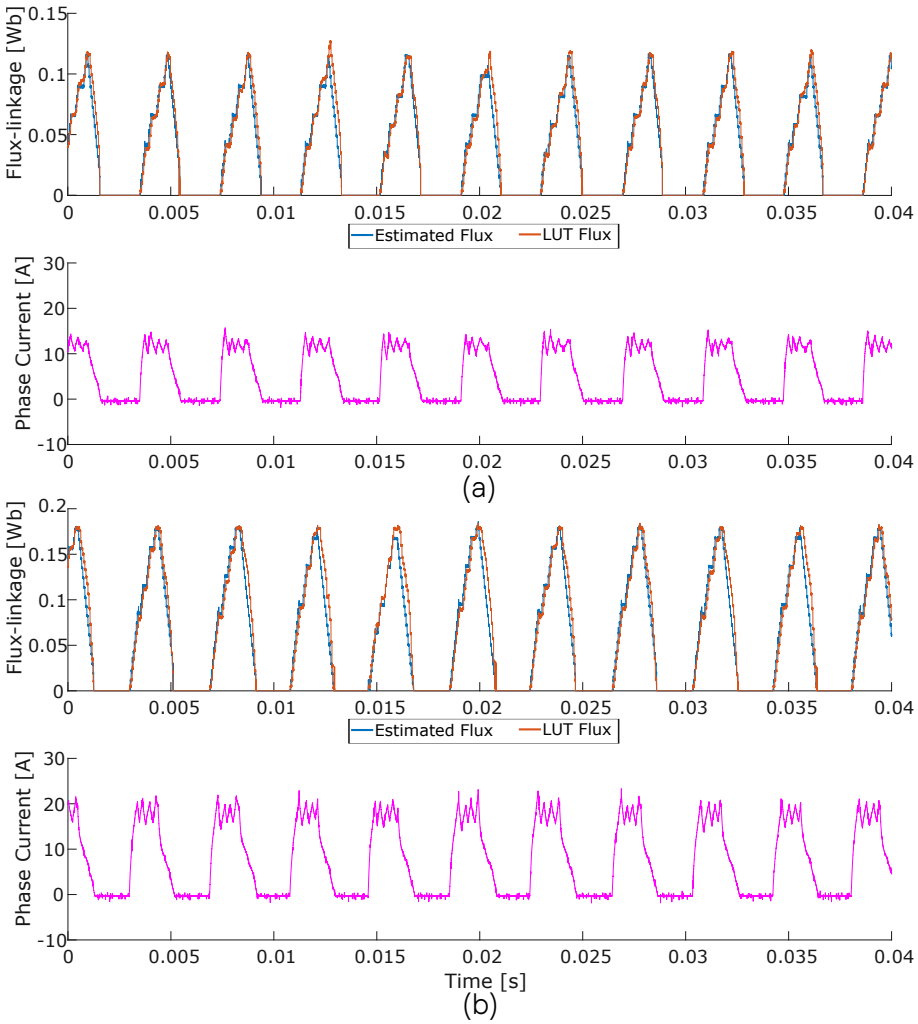

Figure 5.17: Flux-linkage estimation at 2500 rpm under different load conditions. a) low load, b) medium load

Figure 5.18 shows the performance comparison of the sensorless control with a

regularization term and with a series PLL. Similar to the low-speed case, the regularization term presents a good filtering performance of the position deviation, without the trade-off of increased complexity and reduced dynamic performance, since a convergency time of the PI loop is not required.

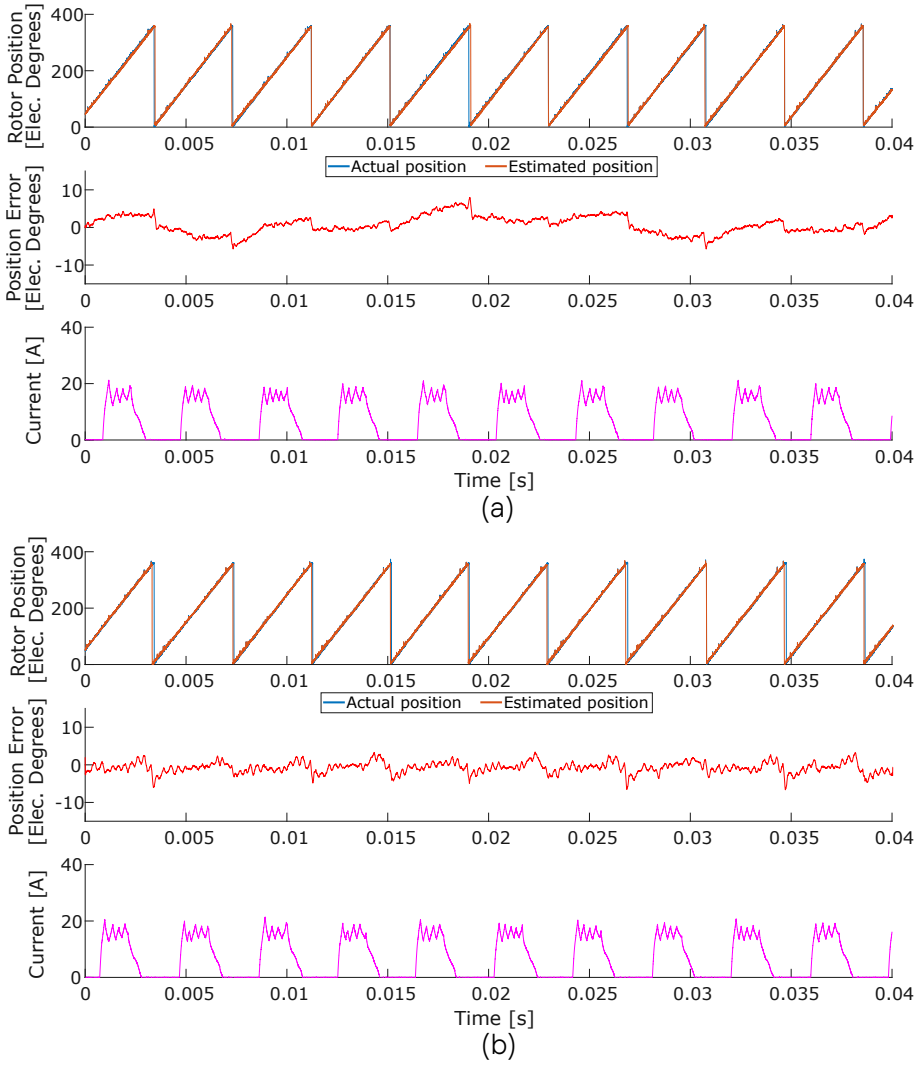

Figure 5.18: High speed sensorless control at 2500 rpm. a) using PLL b) Using regularization term K

5.3.4 Speed Transient Performance

The proposed unified nonlinear optimization-based sensorless control performance is validated during speed-transients over a wide speed range, where speed sweep tests are conducted under different load conditions. The speed changes are commanded as a step response to the dynamometer, where the transient time is dependent on the load condition. Figure 5.19 shows the speed transient performance at a transient from 200 rpm to 1500 rpm, at 30% rated load. The same test is repeated for high to low-speed estimation from 1500 rpm to 200 rpm, as shown in Figure 5.20. The sensorless control was implemented with the regularization term instead of a PLL in both cases.

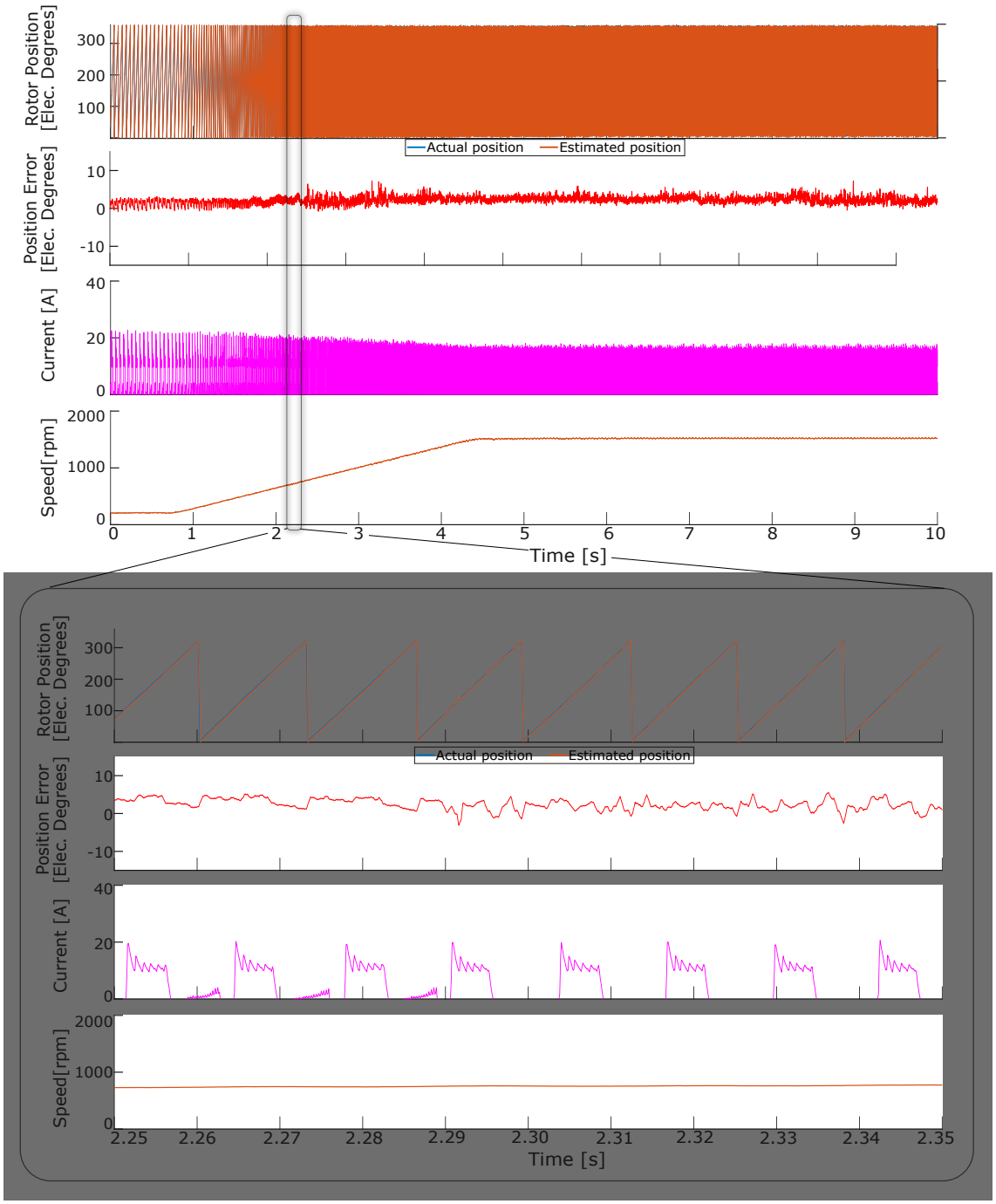

Figure 5.19: Transient performance under low-load condition from 200 rpm to 1500 rpm

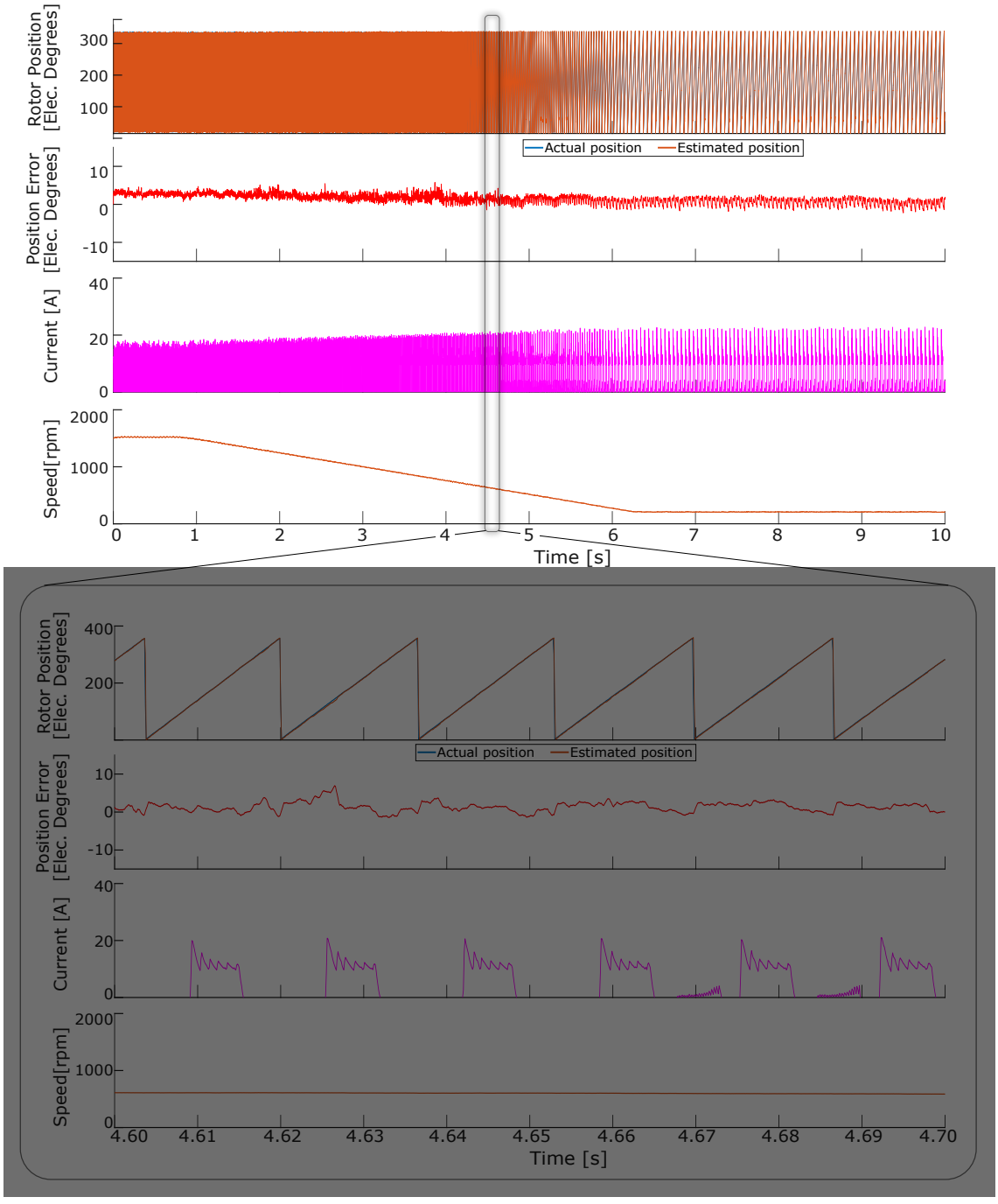

Figure 5.20: Transient performance under low-load condition from 1500 rpm to 200 rpm

5.4 Summary

This chapter proposes the feasibility of the novel unified nonlinear optimization-based sensorless control for a wide-speed operating condition. A cost function was defined using the machine voltage equation and the analytical model using the least-square-based approximation. The rotor position information can be extracted using the Levenberg-Marquardt method for optimization, numerically minimizing the cost function. An aditional high-frequency voltage is injected at low speed to make the system observable, where the extracted inductance information is used on the optimization algorithm. Since the position estimator method remains the same from low and high speeds, a unified position estimator is proposed for a wide speed range. The effectiveness of the cost functions has been validated with a convexity analysis, and the method was experimentally validated. The performance under a wide range of speeds, load conditions, and speed transients was conducted, demonstrating that the proposed method can accurately estimate the position with fast convergence at a wide speed range conditions.

Chapter 6

Benchmarking of the Proposed Method

This section presents a performance benchmark against conventional position estimation techniques. Magnetic parameter-based methods are implemented on the 8/6 switched reluctance machine for a fair comparison.

For the low-speed estimation, a linear inductance-based sensorless control is implemented. A LUT-based method is tested at high speeds, where a hysteresis band with the same lower and upper limits, as proposed for the nonlinear optimization-based method, is used during the transition from different operating speeds. A performance comparison with the UNLO sensorless control is then presented.

6.1 Conventional Sensorless Control Methods

6.1.1 Low-Speed Inductance-Based Signal Injection Position Estimation

For the low-speed estimation, the proposed unified method performance is compared to the linear inductance-based signal injection position estimation method proposed in [45]. This method has a simple implementation using the unsaturated linearized relationship between the phase inductance and rotor position, as presented in section 4.3.1.3. The system was tested using a 6.66kHz injection pulse into the idle phases, where the inductance was calculated using (6.1), and the rotor position was estimated using (6.2).

$$L(\theta(k), i(k)) = \begin{cases} \dfrac{V_{Inj}}{di/dt|_P} & \text{, Turn-ON slope} \\ \dfrac{2V_{Inj}}{di/dt|_P - di/dt|_N} & \text{, Turn-OFF slope} \end{cases} \tag{6.1}$$

$$\begin{aligned} \widehat{\theta} &= \frac{L_{max}(i_k) - L(\theta(k), i(k))}{N} + \theta_{initial} \\ N &= \frac{L_{max}(i_k) - L_{min}(i_k)}{90^\circ}, \end{aligned} \tag{6.2}$$

Figure 6.1 shows the simulation results of the inductance-based signal injection sensorless control under startup conditions and speed varying from 0 rpm to 400 rpm. It should be noticed that the startup routine uses a pulse inject into all phases, as previously discussed in Chapter 4, where the initial sector is identified, and the

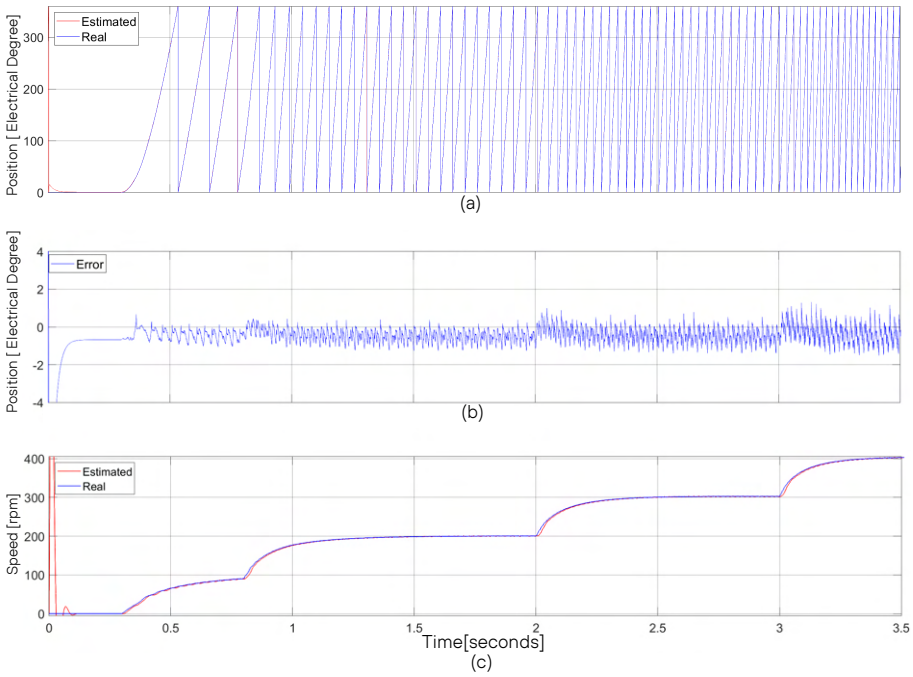

Figure 6.1: Simulation results of the conventional linear inductance-based signal injection position estimation method from 0 to 400 rpm. a) rotor position, b) position error and c) speed

sensing phase can be selected.

This method presents a very simple implementation but is sensitive to current sampling noise and system modeling accuracy, where variations on phase inductance or current noises can produce high errors in the position estimation. In the region where the inductance does not match perfectly the rotor position, the rotor position errors increase, and a PLL algorithm needs to be implemented to reduce the oscillations caused by the current measurement noises and parameter variation. The PLL can limit the system bandwidth depending on the filtering requirements, which becomes a problem during fast-speed transients. Figure 6.2 shows the comparison of open-loop control of the conventional low-speed sensorless control without PLL and

with PLL implementation. The open-loop control operation uses the actual position as feedback to the control loop, where the estimated position is observed. During the test without a PLL, the sensorless algorithm failed to estimate the rotor position correctly, causing the system to become unstable. It can be observed that the rotor position can be estimated with a PLL structure but presents high errors.

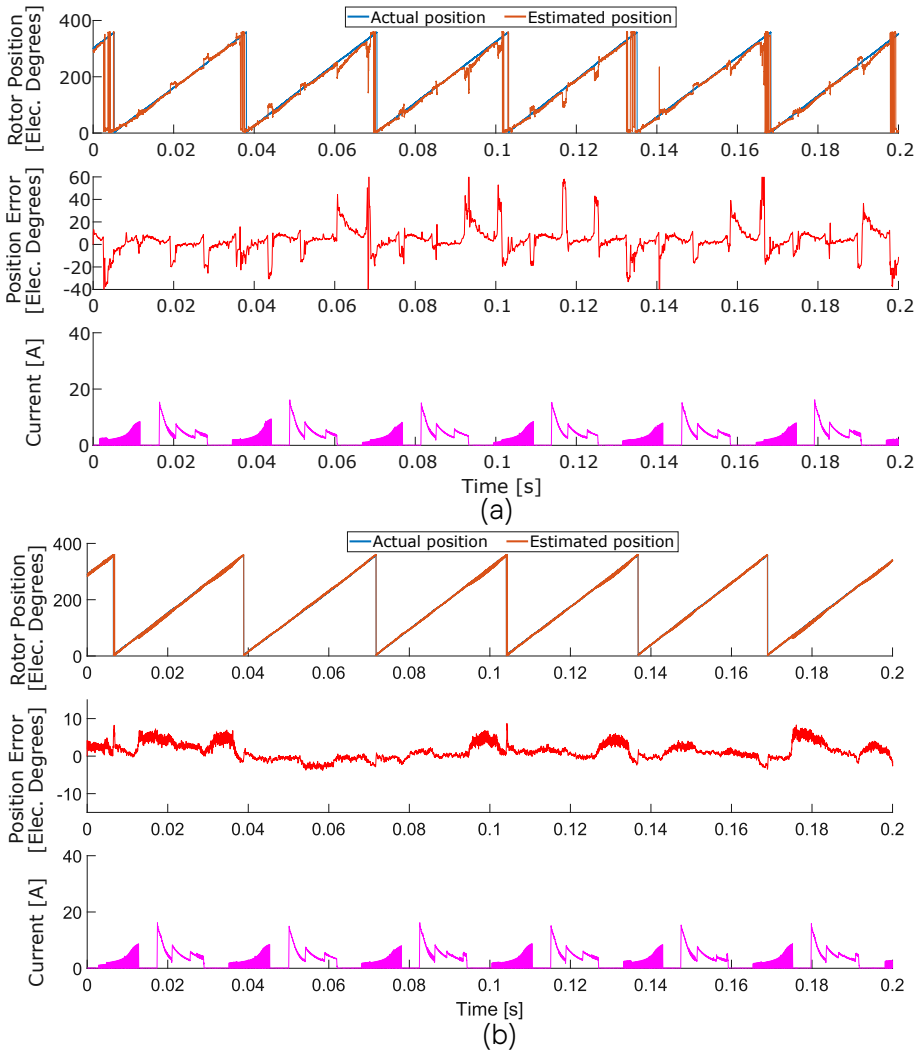

Figure 6.2: Comparison of conventional low-speed position estimation a) whithout a PLL and b) with a PLL

The algorithm was then tested under low load conditions and compared to the proposed nonlinear optimization-based algorithm in Figure 6.3.

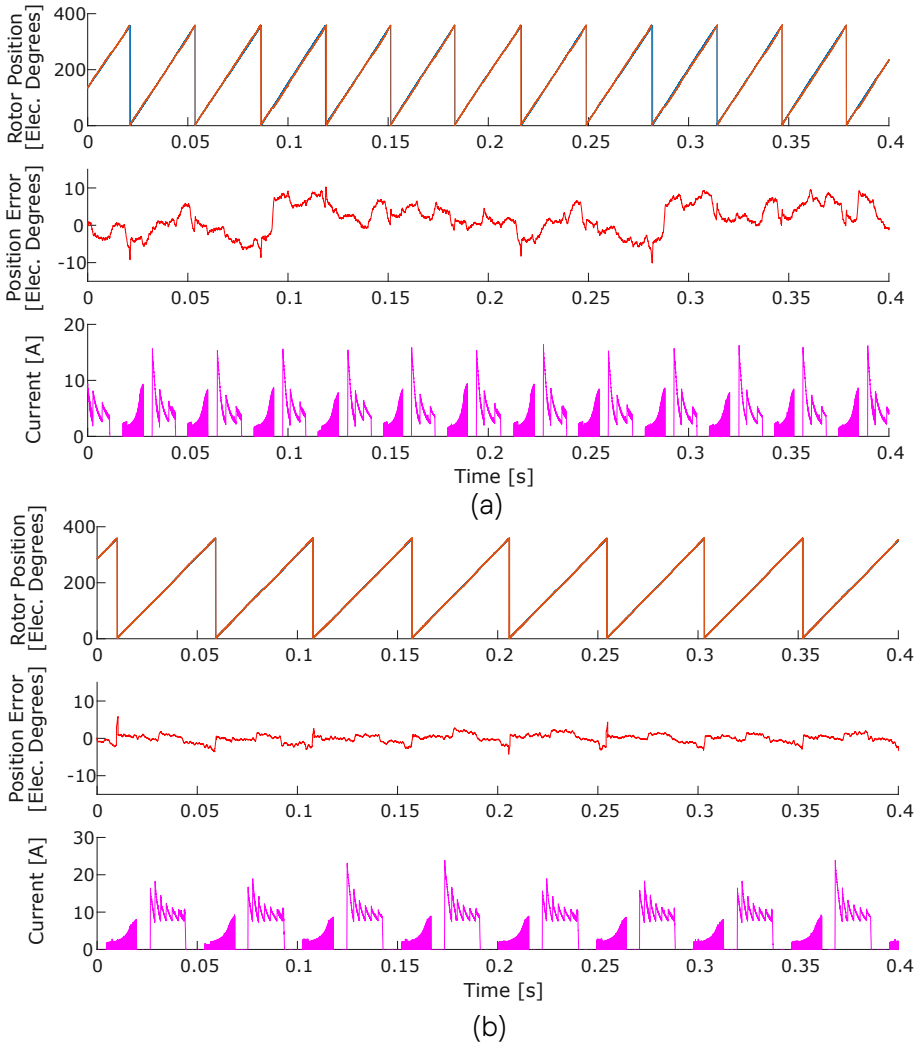

Figure 6.3: Experimental sensorless control comparison. a) Conventional sensorless control at 500 rpm, b) UNLO sensorless control at 200 rpm

Both methods use the same inductance calculation scheme. In this comparison, the conventional method showed high rotor position variations, even after the rotor

position signal is filtered through a PLL algorithm. The proposed method is implemented using the regularization term K without a phase-locked loop, presenting a low oscillation around the measured position.

6.1.2 High-Speed Flux-Linkage LUT-Based Position Estimation

When considering the high-speed benchmark, the LUT-based sensorless control proposed in [69] was selected for comparison. This position estimation class presents good position tracking capability without high computational requirements; although, they require a large storage memory for the lookup table. A 61X45 LUT was implemented for this method with an interpolation algorithm. The same data set used for the proposed UNLO sensorless control was used for the LUT-based estimator for a fair comparison. As presented in Chapter 4 and [46], LUT-based sensorless control algorithms can present a medium noise sensitivity to current sampling errors and parameter mismatch, where the estimated position can deviate from the actual position. Figure 6.4 shows a comparison of the estimated position without and with a series PLL. The PLL can work as a low-pass filter, filtering the oscillations from the measured errors and parameter mismatch, but can also reduce the transient performance under high-speed changes.

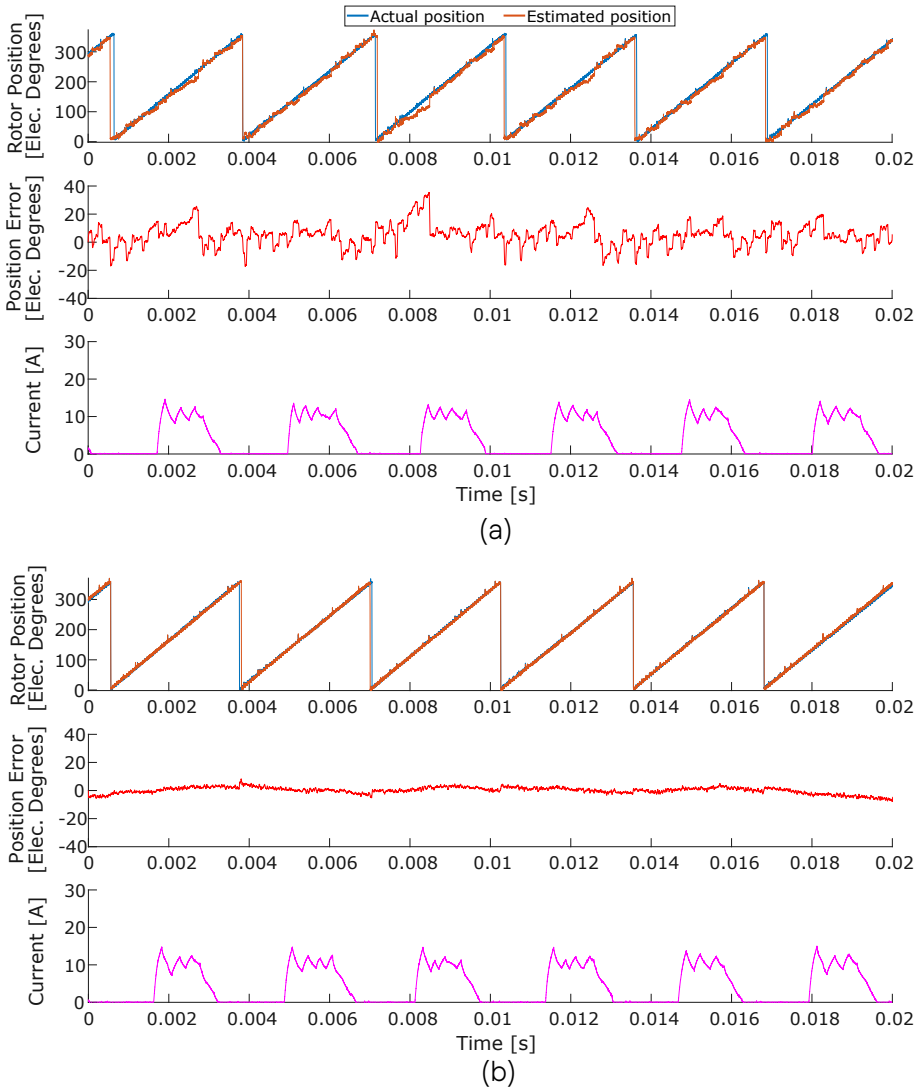

Figure 6.4: Experimental sensorless control comparison at 3000 rpm a) without a PLL, b) with a PLL

Due to the high position errors, a PLL was used during all the tests to improve system reliability and stability. Figure 6.5 shows the performance of the LUT-based algorithm compared to the proposed UNLO.

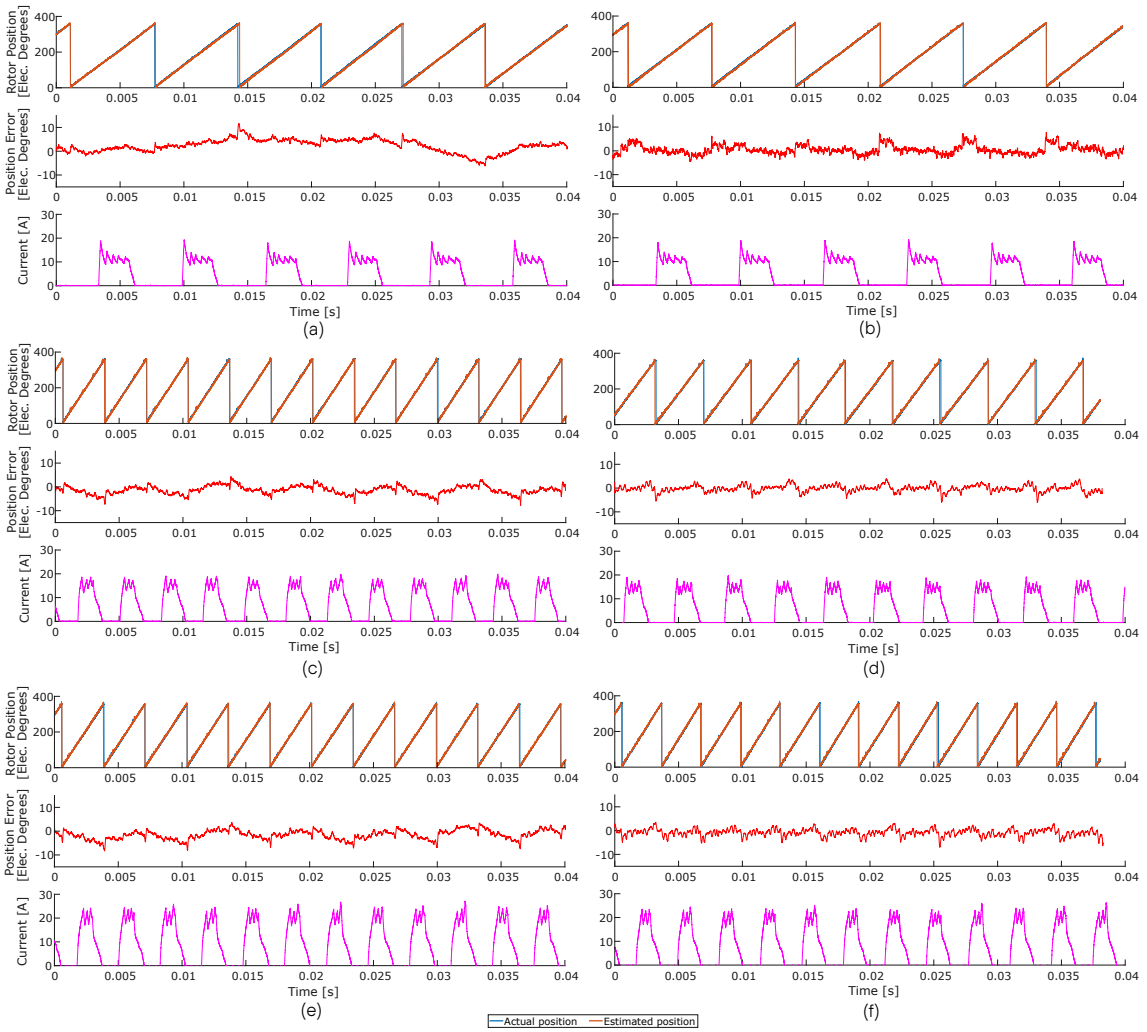

Figure 6.5: Experimental sensorless control comparison a) LUT-based conventional at 1500 rpm, b) low-load UNLO at 1500 rpm, c) mid-load LUT-based at 3000 rpm, d) mid-load UNLO at 3000 rpm rpm, e) high-load LUT-based at 3000 rpm, and f) high-load UNLO at 3000 rpm rpm

For a wide-speed range implementation, a transition algorithm similar to the one proposed in Figure 5.9 was implemented. Additional complexity is added for the conventional sensorless control techniques during the transient between the two

methods since a fast convergence from one method to another has to be guaranteed. The PLL gains have to be adjusted to perform stably during a wide speed range, which presents a trade-off between fast convergency and filtering capability. The wide-speed range from 200rpm to 1500 rpm is presented in Figure 6.6

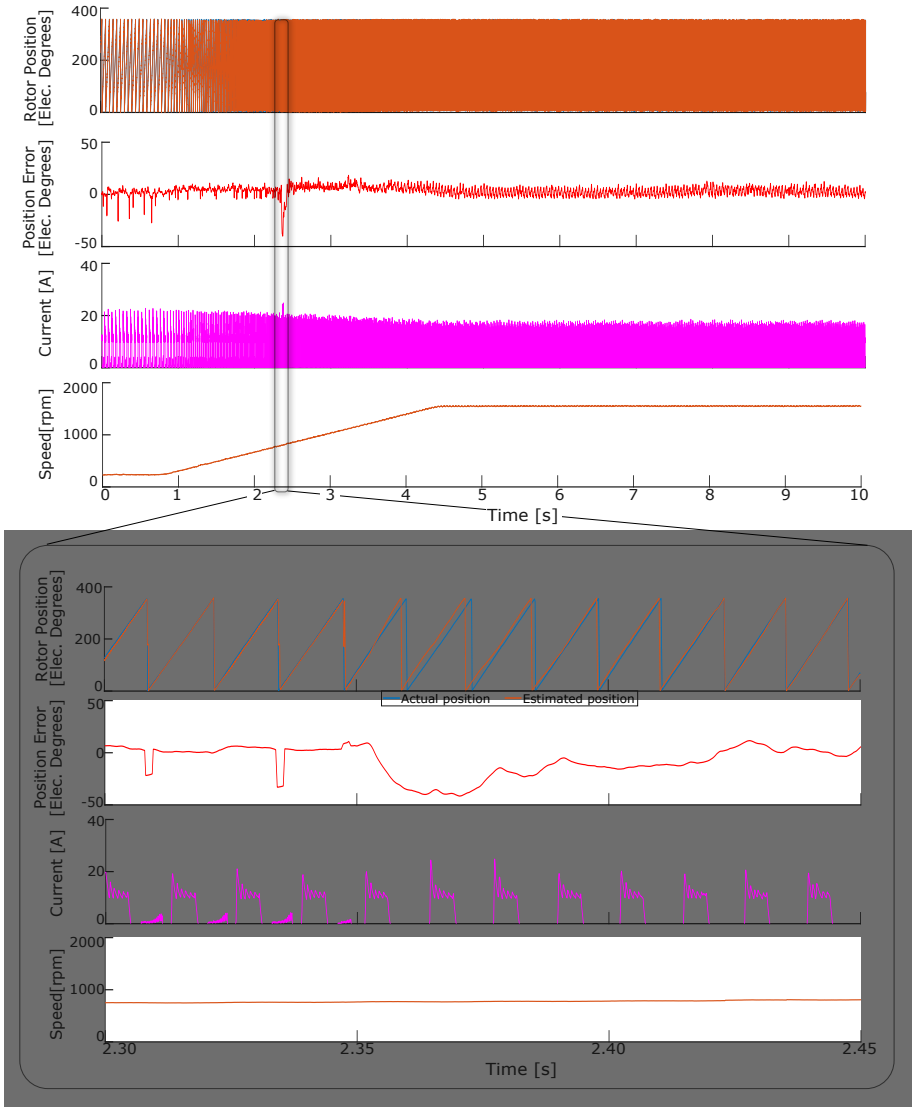

Figure 6.6: Experimental sensorless control during speed transients

As observed, the high gains of the PLL showed high oscillations at low-speed

operation and low deviations at high-speed. To have a stable transition, the PLL gains must be increased to reduce the convergency time. The proposed method shown in Figure 5.19 does not present a similar problem since the same algorithm is used for the entire operating region, and no PLL is required.

6.2 Computational Burden Analysis

The online optimization-based algorithm used in the real-time implementation was introduced in Chapter 5. It requires a defined number of iterations to converge from the initial condition from the time step $(k-1)$ to the actual position (k), searching the optimal coefficient ξ and the cost in a certain decent direction. In this work, three iterations were used, requiring a total of 37μs to compute the optimization algorithm for the proposed nonlinear optimization-based sensorless control method. The computational time of the methods used as benchmark were 16μs and 14μs for the low and high speed, respectively. For the conventional method, both algorithms run in parallel during the transient period, which increases the execution time to a total of 30μs. The combined execution time is required to be allocated for the sensorless control in a real-time implementation. The control frequency of all methods was performed at 20kHz.

Storage space represents an important aspect when implementing the proposed sensorless control algorithms in a microcontroller. The method used in high-speed operation requires a large LUT with a size of 61X45. The proposed method uses a fifth-order polynomial, requiring a 6X6 LUT for the polynomial coefficients storage, significantly reducing the required memory size.

6.3 Summary

In this chapter, the proposed unified nonlinear optimization sensorless control previously investigated in 5 was compared to conventional magnetic parameter-based sensorless controls for low and high-speed operation.

The linear inductance-based techniques were used for low-speed estimation under the same test conditions as the proposed method. A series PLL was implemented to reduce the position estimation errors. The LUT-based sensorless control was implemented and validated under different load conditions at high speeds.

A hysteresis transition loop from low to high speeds was implemented, and the PLL loop was adjusted to provide a stable operation under high-speed transients while still providing a fair estimation accuracy for the conventional methods. Under the same conditions, the proposed UNLO method outperformed the conventional techniques during the steady-state and dynamic performance.

Additionally, the unified wide-speed characteristics of the UNLO can reduce the complexity during the transition from one method to another and drastically improve the dynamic performance of the system. When considering the computational burden, a combined technique presented a similar execution time as the proposed method while requiring a large memory allocation.

Chapter 7

Conclusions and Future Work

7.1 Conclusions

This thesis presents a position estimation method based on a unified nonlinear optimization method for a wide speed range, which improves the system's dynamic performance while maintaining low memory usage and reducing computational requirements.

The performance of optimal controls and magnetic parameter-based sensorless control for SRMs are highly dependent on the nonlinear magnetic characteristics of the machine. Lookup-table-based models are simple to implement but suffer from high memory allocation, which is not desired depending on the proposed application and the available memory size. Analytical-based models represent an excellent alternative option for the magnetic parameter representation and can be defined as linearized and nonlinearized models. Linearized models present simple implementation but have a low model fidelity; therefore, Fourier approximations are usually implemented in the literature to improve the representation accuracy of the machine's magnetic

properties. To further improve the analytical modeling of SRMs, a least-square-based analytical approximation is proposed, showing a substantial improvement from the previous methods, reducing the implementation complexity and computational requirements.

A comprehensive analysis of the commercial rotor position sensors was then presented, showing the advantages and drawbacks of each technology, presenting the main advantages of sensorless control techniques in an overall system cost reduction, increased reliability, position sensor fault detection, fail-safe operation, and possibility in sensor fusion technology.

The unified wide-speed range optimization-based sensorless control algorithm is presented, where a novel cost function is defined from the machine voltage equation, where the rotor position is extracted from the position-dependent inductance profile. The same method is used for the complete speed range. The optimization algorithm is established using a Levenberg-Marquardt method, which combines Newton's method for optimization and the steepest descent method. An additional regularization term using the error from the rotor position at time step $k-1$ and time step k is implemented, reducing the errors in position estimation without the need of a series PLL. The method is then validated at steady-state operation under a wide load condition and fast speed transients. The proposed UNLO method was compared to a conventional linear inductance-based for low-speed estimation and a LUT-based sensorless control for high speeds. The proposed method presented the advantage of reduced complexity during the transition from one method to another; a drastic improvement in the dynamic performance due to the elimination of a PLL loop, a similar execution time when compared to the wide-speed operation of the combined conventional

methods, and a reduced memory requirement.

7.2 Future Work

Related research topics which can be further investigated in future developments are listed as follows:

1. Investigation of the proposed method in a four-quadrant operation and on speed-loop control.

2. Investigation of the performance using a lower-order analytical model of the machine to reduce computational burden.

3. Investigation of different SRM configurations and number of phases.

4. Implementation of the proposed method in a sensor-fusion algorithm for rotor position fault detection and under-fault operation.

5. Investigation of system's robustness under machine fault operation, including inter-turn short, bearing fault, and higher eccentricities. Sensitivity analysis of noises on current and voltage measurements.

6. Investigation of position estimation performance under reduced pulse injection amplitudes and frequencies. Acoustic noise and losses reduction for pulse injection operation.

7. Investigation of performance degradation on torque ripple and acoustic noise reduction algorithms under different rotor position deviations.

7.3 Publications

7.3.1 Journals

S. R. Filho, A. D. Callegaro, G. Fang, D. Xiao and A. Emadi "Unified Nonlinear Optimization-Based Sensorless Control for Switched Reluctance Machine drives" (To be submitted)

D. Xiao, **S. R. Filho**, G. Fang, J. Ye, and A. Emadi "Position-Sensorless Control of Switched Reluctance Motor Drives – A Review," in IEEE Transactions on Transportation Electrification, July 2021.

D. Xiao, S. Nalakath, **S. R. Filho**, G. Fang, A. Dong, Y. Sun, J. Wiseman, and A. Emadi "Universal Full-Speed Sensorless Control Scheme for Interior Permanent Magnet Synchronous Motors," in IEEE Transactions on Power Electronics, vol. 36, no. 4, pp. 4723-4737, April 2021.

Z. Xia, **S. R. Filho**, D. Xiao, G. Fang, Y. Sun, J. Wiseman, and A. Emadi "Computation-Efficient Online Optimal Tracking Method for Permanent Magnet Synchronous Machine Drives for MTPA and Flux-Weakening Operations," in IEEE Journal of Emerging and Selected Topics in Power Electronics, 2020.

7.3.2 Conference

S. R. Filho, L. Sun, T. Lambert, M. Ikhlas, Y. Yang and A. Emadi, "Low-Speed Sensorless Control of a Surface Mounted Permanent Magnet Motor in an e-Bike Application," 2021 IEEE Transportation Electrification Conference and Expo (ITEC), pp. 414-421, 2021.

X. Wang, S. Nalakath, **S. R. Filho**, G. Zhao, Y. Sun, J. Wiseman, and A. Emadi, "A simple and effective compensation method for inverter nonlinearity," in Proc. IEEE Transportation Electrification Conference and Expo (ITEC), pp. 638-643, June 2020.

D. F. Valencia, **S. R. Filho**, A. D. Callegaro, M. Preindl, and A. Emadi, "Virtual-Flux Finite Control Set Model Predictive Control of Switched Reluctance Motor Drives," IECON 2019 - 45th Annual Conference of the IEEE Industrial Electronics Society, Lisbon, Portugal, 2019, pp. 1465-1470.

References

[1] B. Bilgin, J. W. Jiang, and A. Emadi, *Switched Reluctance Motor Drives: Fundamentals to Applications*. Boca Raton, FL: Taylor & Francis, first ed., 2019.

[2] B. Bilgin, P. Magne, P. Malysz, Y. Yang, V. Pantelic, M. Preindl, A. Korobkine, W. Jiang, M. Lawford, and A. Emadi, "Making the case for electrified transportation," *IEEE Transactions on Transportation Electrification*, vol. 1, pp. 4–17, June 2015.

[3] J. W. Jiang, B. Bilgin, and A. Emadi, "Three-phase 24/16 switched reluctance machine for a hybrid electric powertrain," *IEEE Transactions on Transportation Electrification*, vol. 3, pp. 76–85, March 2017.

[4] A. D. Callegaro, B. Bilgin, and A. Emadi, "Radial force shaping for acoustic noise reduction in switched reluctance machines," *IEEE Transactions on Power Electronics*, vol. 34, no. 10, pp. 9866–9878, 2019.

[5] G. Fang, J. Ye, D. Xiao, Z. Xia, and A. Emadi, "Low-ripple continuous control set model predictive torque control for switched reluctance machines based on equivalent linear srm model," *IEEE Transactions on Industrial Electronics*, pp. 1–1, 2021.

[6] G. Fang, J. Ye, D. Xiao, Z. Xia, and A. Emadi, "Computational-efficient model predictive torque control for switched reluctance machines with linear-model-based equivalent transformations," *IEEE Transactions on Industrial Electronics*, pp. 1–1, 2021.

[7] J. Ye, B. Bilgin, and A. Emadi, "An offline torque sharing function for torque ripple reduction in switched reluctance motor drives," *IEEE Transactions on Energy Conversion*, vol. 30, no. 2, pp. 726–735, 2015.

[8] H. Li, B. Bilgin, and A. Emadi, "An improved torque sharing function for torque ripple reduction in switched reluctance machines," *IEEE Transactions on Power Electronics*, vol. 34, no. 2, pp. 1635–1644, 2019.

[9] Z. Xia, B. Bilgin, S. Nalakath, and A. Emadi, "A new torque sharing function method for switched reluctance machines with lower current tracking error," *IEEE Transactions on Industrial Electronics*, vol. 68, no. 11, pp. 10612–10622, 2021.

[10] R. Tarvirdilu-Asl, S. Nalakath, B. Bilgin, and A. Emadi, "A finite control set model predictive torque control for switched reluctance motor drives with adaptive turn-off angle," in *IECON 2019 - 45th Annual Conference of the IEEE Industrial Electronics Society*, vol. 1, pp. 840–845, 2019.

[11] F. Peng, J. Ye, and A. Emadi, "An asymmetric three-level neutral point diode clamped converter for switched reluctance motor drives," *IEEE Transactions on Power Electronics*, vol. 32, no. 11, pp. 8618–8631, 2017.

[12] J. Ye and A. Emadi, "Power electronic converters for 12/8 switched reluctance motor drives: A comparative analysis," in *2014 IEEE Transportation Electrification Conference and Expo (ITEC)*, pp. 1–6, 2014.

[13] K. Ramu, *Switched reluctance motor drives: modeling, simulation, analysis, design, and applications*. CRC Press, 2001.

[14] C. S. Edrington, B. Fahimi, and M. Krishnamurthy, "An autocalibrating inductance model for switched reluctance motor drives," *IEEE Transactions on Industrial Electronics*, vol. 54, no. 4, pp. 2165–2173, 2007.

[15] D. S. Mihic, M. V. Terzic, and S. N. Vukosavic, "A new nonlinear analytical model of the srm with included multiphase coupling," *IEEE Transactions on Energy Conversion*, vol. 32, no. 4, pp. 1322–1334, 2017.

[16] S. Song, M. Zhang, and L. Ge, "A new decoupled analytical modeling method for switched reluctance machine," *IEEE Transactions on Magnetics*, vol. 51, no. 3, pp. 1–4, 2015.

[17] A. Omekanda, C. Broche, and M. Renglet, "Calculation of the electromagnetic parameters of a switched reluctance motor using an improved fem-biem-application to different models for the torque calculation," *IEEE Transactions on Industry Applications*, vol. 33, no. 4, pp. 914–918, 1997.

[18] M. Stiebler and K. Liu, "An analytical model of switched reluctance machines," *IEEE Transactions on Energy Conversion*, vol. 14, no. 4, pp. 1100–1107, 1999.

[19] S. Hossain and I. Husain, "A geometry based simplified analytical model of switched reluctance machines for real-time controller implementation," in *2002*

IEEE 33rd Annual IEEE Power Electronics Specialists Conference. Proceedings (Cat. No.02CH37289), vol. 2, pp. 839–844 vol.2, 2002.

[20] B. Fahimi, G. Suresh, J. Mahdavi, and M. Ehsami, "A new approach to model switched reluctance motor drive application to dynamic performance prediction, control and design," in *PESC 98 Record. 29th Annual IEEE Power Electronics Specialists Conference (Cat. No.98CH36196)*, vol. 2, pp. 2097–2102 vol.2, 1998.

[21] A. Khalil and I. Husain, "Four quadrant sensorless operation of a switched reluctance machine using fourier model," in *2006 37th IEEE Power Electronics Specialists Conference*, pp. 1–8, 2006.

[22] X. Zhang, F. Wang, and X. Wu, "Low-speed direct-driven sensorless control including zero-speed for switched reluctance motor based on dynamic inductance model," in *2014 17th International Conference on Electrical Machines and Systems (ICEMS)*, pp. 763–767, 2014.

[23] S. Milano and A. Microsystems, "Hall-effect sensor ics."

[24] H. Inc., "Hall effect sensing and application."

[25] J. Szymczak, S. O'Meara, J. S. Gealon, and C. Nelson De La Rama, "Precision resolver to digital converter measures angular position and velocity," 2014.

[26] R. Ramamoorthy, "Reduce system costs with resolver-to-digital conversion implementation on c2000 microcontrollers," 2014.

[27] W. Thomson, "On the electro-dynamic qualities of metals:—effects of magnetization on the electric conductivity of nickel and of iron," *Proceedings of the Royal Society of London*, vol. 8, p. 546–550, 1857.

[28] C. Datlinger and M. Hirz, "Benchmark of rotor position sensor technologies for application in automotive electric drive trains," *Electronics*, vol. 9, no. 7, p. 1063, 2020.

[29] R. Guyol, "Amr angle sensors," 2014.

[30] L. Jogschies, D. Klaas, R. Kruppe, J. Rittinger, P. Taptimthong, A. Wienecke, L. Rissing, and M. Wurz, "Recent developments of magnetoresistive sensors for industrial applications," *Sensors*, vol. 15, no. 11, p. 28665–28689, 2015.

[31] M. N. Baibich, J. M. Broto, A. Fert, F. N. Van Dau, F. Petroff, P. Etienne, G. Creuzet, A. Friederich, and J. Chazelas, "Giant magnetoresistance of (001)fe/(001)cr magnetic superlattices," *Physical Review Letters*, vol. 61, no. 21, p. 2472–2475, 1988.

[32] J. S. Moodera, L. R. Kinder, T. M. Wong, and R. Meservey, "Large magnetoresistance at room temperature in ferromagnetic thin film tunnel junctions," *Phys. Rev. Lett.*, 1995.

[33] C. Choi, K. Lee, and W. Lee, "Observer-based phase-shift fault detection using adaptive threshold for rotor position sensor of permanent-magnet synchronous machine drives in electromechanical brake," *IEEE Transactions on Industrial Electronics*, vol. 62, no. 3, pp. 1964–1974, 2015.

[34] S. K. Kommuri, S. B. Lee, and K. C. Veluvolu, "Robust sensors-fault-tolerance with sliding mode estimation and control for pmsm drives," *IEEE/ASME Transactions on Mechatronics*, vol. 23, no. 1, pp. 17–28, 2018.

[35] H. Li, L. Qu, W. Qiao, and C. Wei, "Current and rotor position sensor fault detection and isolation for permanent magnet synchronous generators in wind applications," in *2017 IEEE Applied Power Electronics Conference and Exposition (APEC)*, pp. 2810–2815, 2017.

[36] M. Dybkowski and K. Klimkowski, "Speed sensor fault detection algorithm for vector control methods based on the parity relations," in *2017 19th European Conference on Power Electronics and Applications (EPE'17 ECCE Europe)*, pp. P.1–P.5, 2017.

[37] Y. Mollet and J. Gyselinck, "Rotor-current and position estimator for doubly-fed induction generators - application to sensor-fault detection," in *2016 IEEE International Energy Conference (ENERGYCON)*, pp. 1–6, 2016.

[38] S. Diao, Z. Makni, J.-F. Bisson, D. Diallo, and C. Marchand, "Sensor fault diagnosis for improving the availability of electrical drives," in *IECON 2013 - 39th Annual Conference of the IEEE Industrial Electronics Society*, pp. 3108–3113, 2013.

[39] Y. Ma, L. Lin, and Y. Wang, "Fault diagnosis of the speed sensor of electro-mechanical transmission of the high speed rotorcraft," in *2018 10th International Conference on Modelling, Identification and Control (ICMIC)*, pp. 1–5, 2018.

[40] G. H. B. Foo, X. Zhang, and D. M. Vilathgamuwa, "A sensor fault detection and isolation method in interior permanent-magnet synchronous motor drives based on an extended kalman filter," *IEEE Transactions on Industrial Electronics*, vol. 60, no. 8, pp. 3485–3495, 2013.

[41] Y. Liang and H. Chen, "Circuit-based flux linkage measurement method with the automated resistance correction for srm sensorless position control," *IET Electric Power Applications*, vol. 12, no. 9, pp. 1396–1406, 2018.

[42] K. R. Geldhof, A. P. M. Van den Bossche, and J. A. Melkebeek, "Rotor-position estimation of switched reluctance motors based on damped voltage resonance," *IEEE Transactions on Industrial Electronics*, vol. 57, no. 9, pp. 2954–2960, 2010.

[43] J. Cai, Z. Liu, Y. Zeng, H. Jia, and Z. Deng, "A hybrid-harmonic-filter-based position estimation method for an srm with embedded inductive sensing coils," *IEEE Transactions on Power Electronics*, vol. 33, no. 12, pp. 10602–10610, 2018.

[44] B. Fahimi, G. Suresh, and M. Ehsani, "Review of sensorless control methods in switched reluctance motor drives," in *Conference Record of the 2000 IEEE Industry Applications Conference. Thirty-Fifth IAS Annual Meeting and World Conference on Industrial Applications of Electrical Energy (Cat. No.00CH37129)*, vol. 3, pp. 1850–1857 vol.3, 2000.

[45] X. Wang, *A position sensorless control of switched reluctance motors*. PhD thesis, 2016.

[46] D. Xiao, S. R. Filho, G. Fang, J. Ye, and A. Emadi, "Position-sensorless control of switched reluctance motor drives – a review," *IEEE Transactions on Transportation Electrification*, pp. 1–1, 2021.

[47] M. Ehsani, I. Husain, and A. B. Kulkarni, "Elimination of discrete position sensor and current sensor in switched reluctance motor drives," *IEEE Transactions on Industry Applications*, vol. 28, no. 1, pp. 128–135, 1992.

[48] M. Ehsani, I. Husain, S. Mahajan, and K. R. Ramani, "New modulation encoding techniques for indirect rotor position sensing in switched reluctance motors," *IEEE Transactions on Industry Applications*, vol. 30, no. 1, pp. 85–91, 1994.

[49] G. Pasquesoone, R. Mikail, and I. Husain, "Position estimation at starting and lower speed in three-phase switched reluctance machines using pulse injection and two thresholds," *IEEE Transactions on Industry Applications*, vol. 47, no. 4, pp. 1724–1731, 2011.

[50] M. Krishnamurthy, C. S. Edrington, and B. Fahimi, "Prediction of rotor position at standstill and rotating shaft conditions in switched reluctance machines," *IEEE Transactions on Power Electronics*, vol. 21, no. 1, pp. 225–233, 2006.

[51] H. Gao, F. R. Salmasi, and M. Ehsani, "Sensorless control of srm at standstill," in *APEC 2001. Sixteenth Annual IEEE Applied Power Electronics Conference and Exposition (Cat. No.01CH37181)*, vol. 2, pp. 850–856 vol.2, 2001.

[52] Y. Chang, K. W. E. Cheng, and S. L. Ho, "Type-v exponential regression for online sensorless position estimation of switched reluctance motor," *IEEE/ASME Transactions on Mechatronics*, vol. 20, no. 3, pp. 1351–1359, 2015.

[53] E. Ofori, T. Husain, Y. Sozer, and I. Husain, "A pulse-injection-based sensorless position estimation method for a switched reluctance machine over a wide speed range," *IEEE Transactions on Industry Applications*, vol. 51, no. 5, pp. 3867–3876, 2015.

[54] J. Cai and Z. Deng, "Initial rotor position estimation and sensorless control of srm based on coordinate transformation," *IEEE Transactions on Instrumentation and Measurement*, vol. 64, no. 4, pp. 1004–1018, 2015.

[55] L. Shen, J. Wu, and S. Yang, "Initial position estimation in srm using bootstrap circuit without predefined inductance parameters," *IEEE Transactions on Power Electronics*, vol. 26, no. 9, pp. 2449–2456, 2011.

[56] T. Bamba, A. Komatsuzaki, and I. Miki, "Estimation of rotor position for switched reluctance motor at standstill," in *2007 Power Conversion Conference - Nagoya*, pp. 259–263, 2007.

[57] J. Cai and Z. Deng, "Sensorless control of switched reluctance motor based on phase inductance vectors," *IEEE Transactions on Power Electronics*, vol. 27, no. 7, p. 3410–3423, 2012.

[58] J. Bu and L. Xu, "Eliminating starting hesitation for reliable sensorless control of switched reluctance motors," *IEEE Transactions on Industry Applications*, vol. 37, no. 1, pp. 59–66, 2001.

[59] I. Ralev, S. Max, and R. W. De Doncker, "Accurate rotor position detection for low-speed operation of switched reluctance drives," in *2018 IEEE 18th International Power Electronics and Motion Control Conference (PEMC)*, pp. 483–490, 2018.

[60] J. Cai and Z. Deng, "Unbalanced phase inductance adaptable rotor position sensorless scheme for switched reluctance motor," *IEEE Transactions on Power Electronics*, vol. 33, no. 5, pp. 4285–4292, 2018.

[61] J. Cai and Z. Liu, "An unsaturated inductance reconstruction based universal sensorless starting control scheme for srm drives," *IEEE Transactions on Industrial Electronics*, vol. 67, no. 11, pp. 9083–9092, 2020.

[62] J. Cai, Y. Yan, W. Zhang, and X. Zhao, "A reliable sensorless starting scheme for srm with lowered pulse injection current influences," *IEEE Transactions on Instrumentation and Measurement*, vol. 70, pp. 1–9, 2021.

[63] D. Zhou and H. Chen, "Four-quadrant position sensorless operation of switched reluctance machine for electric vehicles over a wide speed range," *IEEE Transactions on Transportation Electrification*, pp. 1–1, 2021.

[64] H. Guo, M. Takahashi, T. Watanabe, and O. Ichinokura, "A new sensorless drive method of switched reluctance motors based on motor's magnetic characteristics," *IEEE Transactions on Magnetics*, vol. 37, no. 4, pp. 2831–2833, 2001.

[65] J. Shao, Z. Deng, and Y. Gu, "Fault-tolerant control of position signals for switched reluctance motor drives," *IEEE Transactions on Industry Applications*, vol. 53, no. 3, pp. 2959–2966, 2017.

[66] P. Ren, A. Xu, S. Wang, and W. Zhang, "Sensorless control of switched reluctance motor based on the logical relationship of three-phase inductance," in *2018 37th Chinese Control Conference (CCC)*, pp. 5035–5040, 2018.

[67] G. Gallegos-Lopez, P. Kjaer, and T. Miller, "A new sensorless method for switched reluctance motor drives," *IEEE Transactions on Industry Applications*, vol. 34, no. 4, pp. 832–840, 1998.

[68] J. Cai and Z. Deng, "A joint feature position detection-based sensorless position estimation scheme for switched reluctance motors," *IEEE Transactions on Industrial Electronics*, vol. 64, no. 6, pp. 4352–4360, 2017.

[69] N. Fuengwarodsakul, S. Bauer, J. Krane, C. Dick, and R. De Doncker, "Sensorless direct instantaneous torque control for switched reluctance machines," in *2005 European Conference on Power Electronics and Applications*, pp. 10 pp.–P.7, 2005.

[70] K. Ha, R.-Y. Kim, and R. Ramu, "Position estimation in switched reluctance motor drives using the first switching harmonics through fourier series," *IEEE Transactions on Industrial Electronics*, vol. 58, no. 12, pp. 5352–5360, 2011.

[71] D. Panda and V. Ramanarayanan, "Mutual coupling and its effect on steady-state performance and position estimation of even and odd number phase switched reluctance motor drive," *IEEE Transactions on Magnetics*, vol. 43, no. 8, pp. 3445–3456, 2007.

[72] Y. A. Khan and V. Verma, "Investigation of pn and f-mras based speed estimators for vector controlled switched reluctance motor drive," in *2018 IEEE International Conference on Power Electronics, Drives and Energy Systems (PEDES)*, pp. 1–6, 2018.

[73] L. Yu-zhou and Z. Ke-gang, "Sensorless speed control of the switched reluctance motor using extended kalman filter," in *The 2nd International Conference on Information Science and Engineering*, pp. 2375–2378, 2010.

[74] D. Pinto, J. Pelletier, W. Peng, and J. Gyselinck, "Combined signal-injection and flux-linkage approach for sensorless control of switched reluctance machines," in *2016 IEEE Vehicle Power and Propulsion Conference (VPPC)*, pp. 1–6, 2016.

[75] Y. Saadi, R. Sehab, A. Chaibet, M. Boukhnifer, and D. Diallo, "Sensorless control of switched reluctance motor with unknown load torque for ev application using extended kalman filter and second order sliding mode observer," in *2018 IEEE International Conference on Industrial Technology (ICIT)*, pp. 522–528, 2018.

[76] E. Mese and D. Torrey, "An approach for sensorless position estimation for switched reluctance motors using artifical neural networks," *IEEE Transactions on Power Electronics*, vol. 17, no. 1, pp. 66–75, 2002.

[77] S. Paramasivam, S. Vijayan, M. Vasudevan, R. Arumugam, and R. Krishnan, "Real-time verification of ai based rotor position estimation techniques for a 6/4 pole switched reluctance motor drive," *IEEE Transactions on Magnetics*, vol. 43, no. 7, pp. 3209–3222, 2007.

[78] A. Bellini, F. Filippetti, G. Franceschini, C. Tassoni, and P. Vas, "Position sensorless control of a srm drive using ann-techniques," in *Conference Record of 1998 IEEE Industry Applications Conference. Thirty-Third IAS Annual Meeting (Cat. No.98CH36242)*, vol. 1, pp. 709–714 vol.1, 1998.

[79] T. Shi, C. Xia, M. Wang, and Q. Zhang, "Single neural pid control for sensorless switched reluctance motor based on rbf neural network," in *2006 6th World Congress on Intelligent Control and Automation*, vol. 2, pp. 8069–8073, 2006.

[80] D. Xiao, J. Ye, G. Fang, Z. Xia, X. Wang, and A. Emadi, "Improved feature-position-based sensorless control scheme for srm drives based on nonlinear state observer at medium and high speeds," *IEEE Transactions on Power Electronics*, vol. 36, no. 5, pp. 5711–5723, 2021.

[81] Y. Sun, M. Preindl, S. Sirouspour, and A. Emadi, "Unified wide-speed sensorless scheme using nonlinear optimization for ipmsm drives," *IEEE Transactions on Power Electronics*, vol. 32, no. 8, pp. 6308–6322, 2017.

[82] S. Nalakath, Y. Sun, M. Preindl, and A. Emadi, "Optimization-based position sensorless finite control set model predictive control for ipmsms," *IEEE Transactions on Power Electronics*, vol. 33, no. 10, pp. 8672–8682, 2018.

[83] D. F. Valencia, L. Sun, M. Preindl, and A. Emadi, "Convex optimization-based sensorless control for ipmsm drives with reduced complexity," in *IECON 2018 - 44th Annual Conference of the IEEE Industrial Electronics Society*, pp. 439–444, 2018.

[84] L. Sun, S. Nalakath, A. D. Callegaro, and A. Emadi, "Investigation of a practical convex-optimization-based sensorless scheme for ipmsm drives," *IEEE Transactions on Power Electronics*, vol. 34, no. 12, pp. 12437–12452, 2019.

[85] D. Xiao, S. R. Filho, G. Fang, J. Ye, and A. Emadi, "Position-sensorless control of switched reluctance motor drives – a review," *IEEE Transactions on Transportation Electrification*, pp. 1–1, 2021.

[86] D. Xiao, J. Ye, G. Fang, Z. Xia, X. Wang, and A. Emadi, "Improved feature-position-based sensorless control scheme for srm drives based on nonlinear state

observer at medium and high speeds," *IEEE Transactions on Power Electronics*, vol. 36, no. 5, pp. 5711–5723, 2021.